DEVELOPMENT OF A DYNAMIC COUPLED HYDRO-GEOMECHANICAL CODE AND ITS APPLICATION TO INDUCED SEISMICITY

A Dissertation
presented in partial fulfillment of requirements
for the degree of Doctor of Philosophy
in the Department of Civil Engineering
The University of Mississippi

by

MD. MAMUN MIAH

August 2016

Copyright Md. Mamun Miah 2016
ALL RIGHTS RESERVED

ABSTRACT

This research describes the importance of a hydro-geomechanical coupling in the geologic sub-surface environment from fluid injection at geothermal plants, large-scale geological CO_2 sequestration for climate mitigation, enhanced oil recovery, and hydraulic fracturing during wells construction in the oil and gas industries. A sequential computational code is developed to capture the multiphysics interaction behavior by linking a flow simulation code TOUGH2 and a geomechanics modeling code PyLith. Numerical formulation of each code is discussed to demonstrate their modeling capabilities. The computational framework involves sequential coupling, and solution of two sub-problems- fluid flow through fractured and porous media and reservoir geomechanics. For each time step of flow calculation, pressure field is passed to the geomechanics code to compute effective stress field and fault slips. A simplified permeability model is implemented in the code that accounts for the permeability of porous and saturated rocks subject to confining stresses. The accuracy of the TOUGH-PyLith coupled simulator is tested by simulating Terzaghi's 1D consolidation problem. The modeling capability of coupled poroelasticity is validated by benchmarking it against Mandel's problem. The code is used to simulate both quasi-static and dynamic earthquake nucleation and slip distribution on a fault from the combined effect of far field tectonic loading and fluid injection by using an appropriate fault constitutive friction model. Results from the quasi-static induced earthquake simulations show a delayed response in earthquake nucleation. This is attributed to the increased total stress in the domain and not accounting for pressure on the fault. However, this issue is resolved in the final chapter in simulating a single event earthquake dynamic rupture. Simulation

results show that fluid pressure has a positive effect on slip nucleation and subsequent crack propagation. This is confirmed by running a sensitivity analysis that shows an increase in injection well distance results in delayed slip nucleation and rupture propagation on the fault.

DEDICATION

This dissertation is dedicated to my family back in Bangladesh, especially my mother Parvin Begum without whose inspiration and support I would not have got primary education let alone advanced study.

ACKNOWLEDGMENTS

It is not possible to acknowledge everybody who has contributed to my doctoral research. Nevertheless, I have tried my best to mention them here. I am grateful and thankful to the following persons. My academic advisor Dr. Christopher Mullen supported my research interests in Oxford and Berkeley. With his guidance, I was introduced to the finite element analysis of structure, which has been instrumental in understanding the numerical computation. William Foxall from Lawrence Berkeley National Laboratory (LBNL) has funded my doctoral research.

Lawrence Hutchings brought me to the LBNL as a summer intern in 2013 after a recommendation by Curtis Oldenburg (thanks a bunch to him). This paved the way for me to further explore my interest which eventually led to the formulation of my doctoral research topic. In addition, Larry and Bill have helped me understand the complexity of physics of earthquakes. Laura Blanco Martin contributed to the development of the computational code. She has been working with me very closely since I started my research at Berkeley. Dr. Chung Song was in my prospectus committee and helped me formulate the research scope. The Civil Engineering Department Chair, Dr. Yacoub Najjar, has continuously supported my work and serves on my committee. Dr. Al-Ostaz is on my committee and taught me a very important course, Continuum Mechanics, which has been very useful in my research. I have learned a lot from a non-departmental course named Groundwater Flow taught by Dr. Robert Holt. As a member of my committee, he has been supporting me continuously in understanding the complexity of subsurface fluid flow problem.

Very often, I have sought out Jonny Rutqvist at the LBNL to get insight into the coupling

of two different computational codes since he has a great deal of expertise in that area. Antonio Pio Rinaldi, at the ETH Zurich, got me started with the computational work of my research and has been helping me remotely from Switzerland. Khalid Ashraf, a post-doc in the Physics Department at UC Berkeley, has helped me understand mathematical formulation of a physical problem in dealing with my research. My landlords Donald and Elizabeth Erickson have supported me and shown curiosity about my work. Discussion with them has enabled me to better explain technical problems to non-experts in the field.

Finally, I am really thankful to all the teachers, relatives, co-workers, and friends who have contributed to my current knowledge and supported me during these last several years of advanced study.

TABLE OF CONTENTS

LIST OF TABLES

LIST OF FIGURES

CHAPTER I

INTRODUCTION

1.1 Description

This research describes development of a coupled hydro-geomechanical code and its application to the context of induced seismicity evaluation due to fluid injections at the geothermal development. The application of this code could be further extended to the evaluation ground subsidence problem from pumping, well stimulation problems in enhanced oil and gas recovery, fate of subsurface liquid nuclear waste disposal, induced seismicity risk from geological carbon dioxide sequestration.

Various human activities such as mining, fluid extraction in the energy industry, fluid injection at the geothermal plants, geological carbon sequestration, and reservoir impoundment result in small scale earthquake. Among them, fluid injection in the geothermal plants has raised a serious concern in various parts of the world where people use this technology. Specially, the occurrence of induced earthquake at the hot dry rock EGS in Basel, Switzerland led to its initial suspension and subsequent cancellation of the entire project [Bachmann, 2011]. It is worth mentioning here that the Swiss authority had not performed a thorough seismic risk assessment before starting geothermal stimulation. Earthquake events at the Soultz project in France raised a significant concern among the residents living nearby [Baria et al., 2005]. Very recently, the State of Oklahoma experienced a total of twenty felt earthquakes in a single day [NEWS, 2014]. Scientists believe that hydraulic fracturing is the main cause for these unexpected trembling

events.

Figure 1.1 delineates the induced seismicity phenomenon by using the concept of effective stress and pore-water pressure. Normal stress tends to lock the two slipping plane together whereas the pore water pressure works in outward direction thereby reducing the effective stress. This, in turn, reduces the shear strength of the rock making it more susceptible to slippage.

Figure 1.2 [Majer et al., 2007], which shows an example of induced seismicity being caused by water injection, is a cross section of the earth showing the location of earthquakes [green dots], as well as the locations of injection wells [thick blue lines] and production wells [thin lines, these wells extract fluid]. Note the large number of events associated with the injection wells.

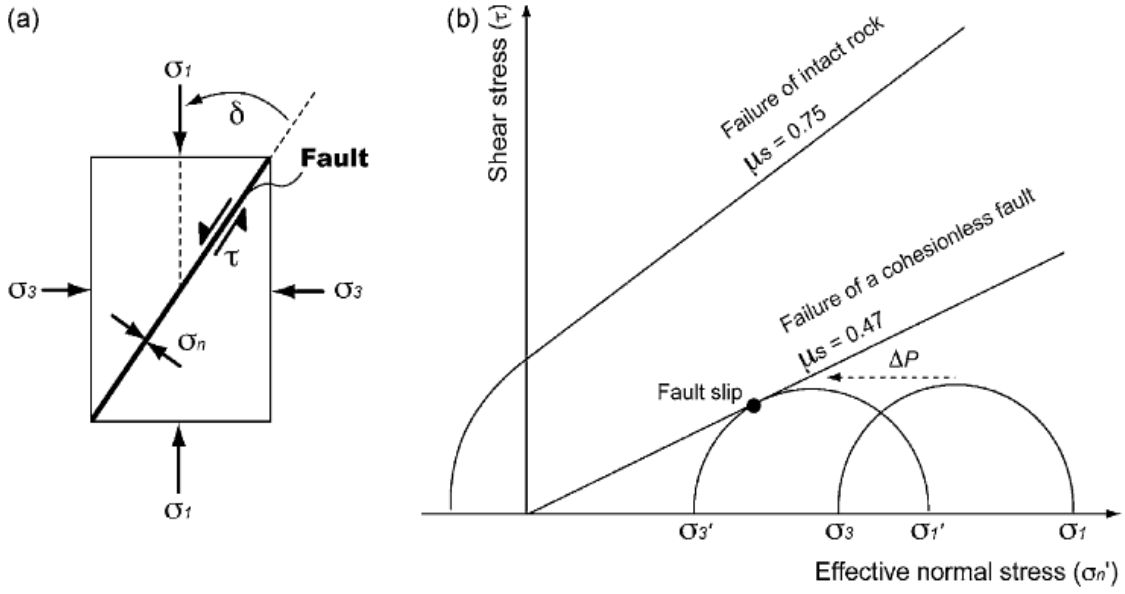

Figure 1.1 A fault plane along the diagonal describing the normal stress, pore water pressure, and fault plane shear strength [Cappa and Rutqvist, 2010]

Other factors thought to be responsible may be thermal changes and/or chemical changes caused by fluid movement and injection. This type of induced seismicity has been noted not only in

geothermal reservoirs but in reservoir impoundment [water behind dams], waste injections, oil and gas operations, and underground injection of fluids for waste disposal. Almost all of the significant events [recorded activity and in some cases felt activity] are associated with shear failure.

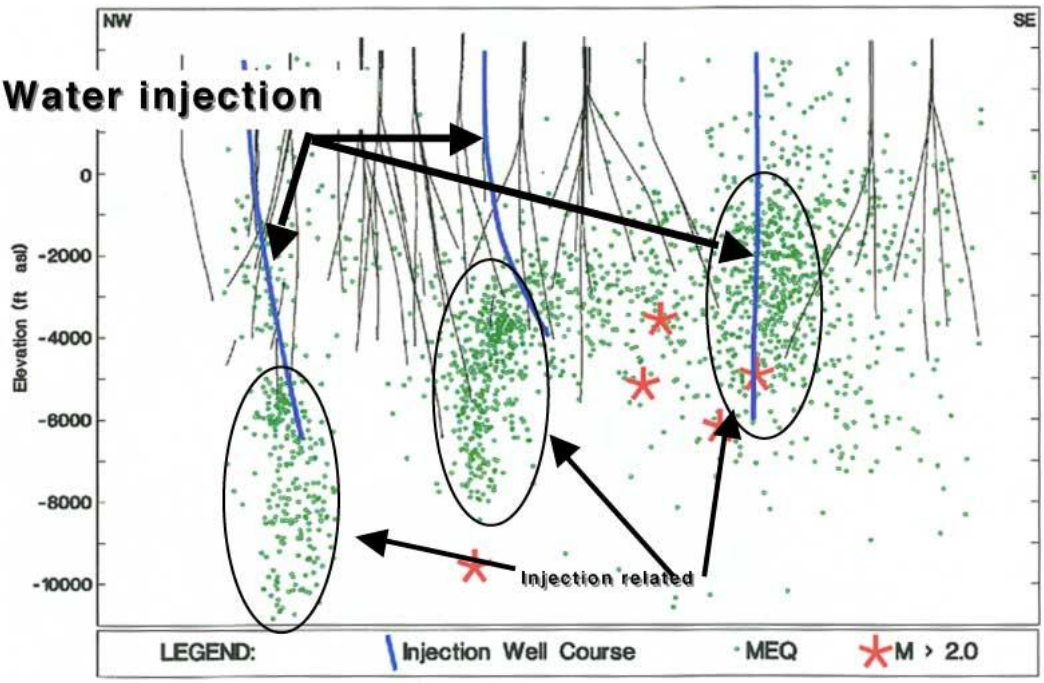

Figure 1.2 Example of injection related seismicity; note the close correlation between water injection wells and the location of the seismicity

1.2 Motivation

The complex interaction of coupled flow and geomechanics has received significant attention in engineering and the geosciences. Among other applications, knowledge of hydro-geomechanical coupling behavior is critical in improving understanding of enhanced geothermal systems, enhanced oil recovery, assessing the environmental impact of groundwater use-, as well as induced seismicity, and monitoring and evaluating subsurface liquid waste disposal, geological carbon sequestration, and reservoir stimulation processes [e.g., Kohl et al, 1995;

Morris, 2009; Rutqvist and Tsang, 2012; Zoback and Gorelick, 2012]. For example, in scientific and engineering studies of CO_2 injection for geological sequestration, understanding the interaction behavior of supercritical CO_2 with a reservoir and caprock requires coupled modeling. Similarly, modeling coupled fluid flow and geomechanical deformation in fractured and porous media enables us to calculate the subsurface pressure and stress changes that can lead to coseismic slip on faults and fractures, which enhances permeability in geothermal systems. In faulted and fractured reservoirs, stress- and shear slip-dependent permeability changes are of special interest both at a local and field scales [Gutierrez et al., 2001]. Fluid-induced stress and strain changes in the reservoir and overburden also impact wellbore stability, and therefore are of importance to the oil and gas industry [Zuluaga et al., 2007; Zoback, 2007].

The knowledge of hydro-geomechanical coupled problems and poroelasticity is essential in understanding multifarious subsurface problems across various disciplines. Some field cases that involves this coupled interaction processes are briefly described herein.

1.2.1 Geothermal systems

Geothermal energy is a thermal energy stored in the earth's subsurface due to its formation and radioactive decay of minerals. Historically, people have been extracting and using this energy across the world [e.g., Lund and Freeston; Zhang et al., 2000b; Teklemariam et al., 2000; Schellschmidt et al., 2000] especially in the areas having more geothermal and tectonic activities. Figure 1.3 shows a typical geothermal system and its various components. Fluid (usually cold water) is injected through injection wells (6) at a high injection pressure. Bedrock (10) is being fractured due to high injection pressure through which injected water propagates near the production wells. The heated water is produced back to the surface through production

wells (5) where it is used to rotate turbines to generate electricity.

In order to develop a geothermal area on a commercial scale, very often a site is stimulated by injecting water into the hot subsurface and creating cracks. This results in permeability increase [Pruess, 2006; McClure, 2009; Béatrice et al., 2010] and increased amount of water which can then be circulated through the hot and porous rock before producing it back to the surface as steam. This is known as an Enhanced Geothermal System (EGS). In such a system, when water is injected into the upper layers of the Earth's crust, it can create micro seismic activities. Scientists have been routinely using sensitive surface and downhill geophones to record small seismic events and monitor fluid movement during injection operations [Batra et al., 1984; Baria et al., 2004; Majer et al., 2005; Rivas et al., 2005; Asanuma et al., 2005]. However, under some conditions, injection operations have produced sufficiently large seismic events [Majer et al., 2007; Li et al., 2007; Shapiro and Dinske, 2009; Giardini, 2009; Nicol et al., 2011] to cause ground motion that is felt at the Earth's surface, and questions remain as to whether induced seismicity can be large enough to cause damage to the buildings and injuries or deaths to the people.

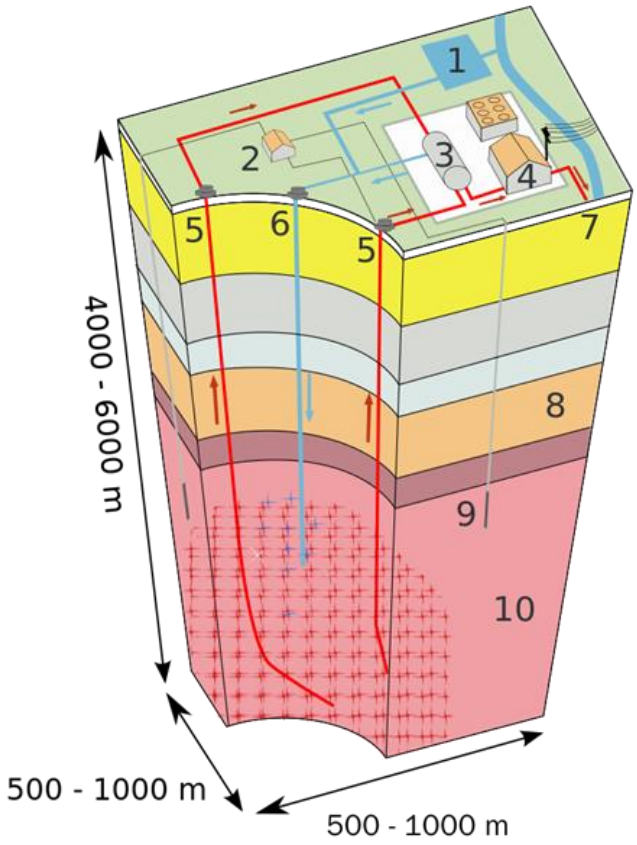

Figure 1.3 Schematics of a geothermal systems: ©M. Haering Geothermal Explorers Ltd, 2007

1.2.2 Geological CO_2 sequestration

In geological carbon sequestration sites, CO_2 is stored in the deep subsurface under high pressure and temperature. Although CO_2 is a gas in normal state, it acts like a supercritical fluid under that subsurface condition. This supercritical nature of CO_2 makes it favorable to be stored in the porous rock strata. Since supercritical CO_2 is less dense than the water, it is more likely to leak off through the cap rock especially if it is fractured and highly permeable. Large scale storage of CO_2 in deep faulted reservoirs causes pore-pressure perturbations resulting in stress drops eventually leading to small scale seismic activity [Hawkes et al., 2004; Cappa and Rutqvist, 2011; Zoback and Gorelick, 2012; Mazzoldi et al., 2012]. Leaking off of the pressurized CO_2 in the nearby fault systems have been associated with two earthquakes- Matsushiro earthquake swarm in Central Japan [Cappa et al., 2009], and the 1997 Umbria-Marche seismic sequence in northern Italy [Miller et al., 2004].

1.2.3 Oil and gas stimulation from reservoirs

Hydraulic fracturing is a conventional way of reservoir stimulation and oil and gas shale production. In low permeability matrix environment hydraulic fracturing is particularly used to increase the permeability to tap into the trapped oil inside rock pores and fissures [Economides and Martin, 2007]. The hydraulic fracturing procedure is conceptualized as a network of new fractures as well as expansion of the preexisting fractures which tend slip and open during the stimulation [e.g. Pine and Batchelor, 1984; Bowker, 2007; Fisher et al., 2004; Cipolla, 2008]. More recently, horizontal drilling in unconventional well stimulation has resulted in improved oil and shale gas production. Creating fractures by injecting water at a high pressure thereby increasing the permeability between wellbore and oil storage is a coupled hydro-geomechanical

process [Baisch et al., 2010; Ghassemi and Zhou, 2010; Tarasovs and Ghassemi, 2012]. Recently, McClure [McClure, 2014] has used a boundary element method to study coupled fluid flow, stresses induced by fracture opening and sliding, transmissivity coupling to deformation, friction evolution, and deformation in a discrete fracture network modeling. He has further applied his computational code to demonstrate how hydraulic fracturing contributes to inducing small scale seismicity.

1.2.4 Subsurface liquid waste disposal

Wastewater and nuclear waste disposal and storage in the earth's subsurface are coupled thermal- hydrological- mechanical-chemical processes [e.g. Xu et al., 2004; Kim et al., 2004; Rutqvist et al., 2005]. Wastewater injection at a depth of 3.7 km in the Rocky Mountain Arsenal Well in Denver, Colorado was associated with induced seismicity [McGarr et al., 2002]. There was no or little record of seismic activities before the injection period. One of the most prominent examples of wastewater injection related seismicity was seen in KTB (German Deep Drilling Program) [Zoback and Harjes, 1997].

1.2.5 Reservoir impoundment

Reservoir impoundment has been found in association with induced seismicity over seventy locations worldwide [Talwani, 1997]. Reservoir impoundment gradually increases the pore pressure in the submerged dam and acts the same way as in fluid injection.

1.2.6 Subsidence from groundwater pumping

Withdrawal of groundwater is linked with surface deformation on the ground. Studies

[Geertsma, 1973; Bear and Corapcioglu, 1981; Mossop and Segall , 1997; Gambolati et al., 2000; Galloway and Burbey, 2011] have been performed to understand the phenomenon of groundwater pumping and ground subsidence but still insufficient due to lack of limited knowledge.

Since coupled mechanisms play a significant role in understanding complex interactions across multidisciplinary areas, developing an accurate modeling scheme is of great interest. Therefore, coupled fluid and heat flow and deformation modeling has been studied quite extensively [Settari and Mourits, 1994; Mainguy and Longuemare, 2002; Thomas et al., 2003; Minkoff et al., 2003; Tran et al., 2004; Jha and Juanes, 2007; Kim, 2009; Rutqvist et al. 2013; Rinaldi et al., 2014]. In the research work described here, we develop a computational methodology to model coupled thermal-hydraulic-mechanical mechanisms specifically to simulate permeability and porosity changes, earthquake nucleation, and slip distribution due to poroelastic changes along the fault. The code is also capable of simulating dynamic rupture of a fault, and subsequent ground motions during earthquakes induced by subsurface fluid injection. However, this is beyond the scope of this dissertation. Also, in our current coupled framework, we only consider a single phase flow and do not include fully thermo-poroelastic effects that may arise from changes in temperature or saturation. These aspects will be addressed in the near future.

CO_2 storage and geothermal development operations aim to avoid any conditions that could cause felt ground-motion events, or destructive ground motions. Therefore, National Risk Assessment Partnership (NRAP) is interested in developing a methodology to assess risks from induced seismicity [Wainwright et al., 2012; Foxall et al., 2013]. This is the motivation to pursue my doctoral research in order to understand the induced seismicity mechanism from the

fundamental point of view and link it to the risk assessment of nearby building structures of a given site. The correlation between the fluid injection or production and generation of microseismicity has been studied by many [e.g., Zoback and Harjes, 1997; Parotidis et al., 2003; Shapiro et al., 2005b; Fischer et al., 2008; Cuenot et al., 2008; Shapiro and Dinske, 2009; Baisch et al., 2010]. Maillot et al. [1999] investigated the induced seismicity from fluid injection by combining a fluid pressure diffusion model with a rock deformation seismicity model. But they ignored the effect of rock seismic deformations on the changes in permeability and porosity which is the central part of my research. Every time there is a seismic slip, the stress field in the surrounding faults zone changes resulting in changes in porosity and permeability. The new porosity and permeability accounts for the subsequent slip potential of the seismic cycle.

1.3 Objectives

The objectives of this work are to:

- develop a coupled hydro-geomechanical code by coupling a flow code TOUGH2 [Pruess et al., 1999] and a dynamic geomechanics code PyLith [Aagaard et.al., 2014]
- validate the simulator against classical analytical solutions of coupled poroelasticity problems
- apply the coupled simulator to model quasi-static earthquakes from fluid injection
- simulate dynamic rupture of a single earthquake event triggered by fluid injection

1.4 Outline

Chapter one describes the research and its scope, research motivation, research objectives, and the dissertation outline. It briefly explains various aspects of hydro-geomechanical coupling

and its implication in wide variety of applications.

Chapter two describes literature review related to coupled poroelasticity and geomechanics problems. It starts out with the description of Terzaghi's [Wang, 2000] experiment for 1D consolidation problems in order to clarify the concept of total stress, pore water pressure, and effective stress. Next, Biot's theory [Biot, 1941] for coupled poroelasticity problem is revisited to explain the fluid-soil coupling interaction by means of two constitutive equations and three distinct poroelastic coefficients. Governing equations for coupled fluid flow and geomechanics are derived from a fluid mass balance equation and a mechanics momentum balance equation. Later it discusses the poroelastic effects in the fractured rock, fluid-induced seismicity and permeability changes, and permeability evolution during seismic slips along faulted zones. Some literature is explored related to multiphase flow and saturation in an underground reservoir condition. Various available fault constitutive models are explored in order to represent the fault friction during a complete earthquake cycle.

Chapter three describes the development procedure of the computational code. First, numerical formulations for the flow code TOUGH2 and geomechanics code PyLith are introduced. Discretization procedure of each of the codes is then discussed. Next, the solution strategy for each of the codes is explained in order to demonstrate their underlying numerical solution procedure. This is important since the two codes (TOUGH2 and PyLith) are linked and solved sequentially using their individual efficient solvers. We also discuss the time stepping procedure implemented in TOUGH2 and PyLith; since they have different numerical procedures, and different time and length scales for solving physical problems. Also discussed are the various coupled algorithms for solving a multiphysics problem and their comparative advantages and disadvantages. At the end of the chapter, the detailed step-by-step computational procedure

of the coupled simulator is illustrated by means of flow charts.

In chapter four, the validity of the coupled code is demonstrated through a couple of representative simulations that test the validity and accuracy of a coupled poroelasticity problem. Terzaghi's 1-D consolidation problem is used to test the accuracy of the one-way coupling from fluid to solid. For validation with a two-way coupled poroelasticity problem, the code is benchmarked against Mandel's analytical solution. The stress or pressure evolution obtained TOUGH-PyLith is compared with analytical and numerical approaches. Specifically, TOUGH-FLAC3D [Rutqvist et al., 2002] is used to show the agreement between the results obtained.

Chapter five describes hydro-geomechanical simulation of earthquakes induced by fluid injections in geothermal reservoirs. It starts with the description of an earthquake rupture, parameters to consider for a fault rupture simulation, and the dynamics of earthquake rupture propagation. The chapter puts detailed explanation and implementation of the aforementioned rate- and state-dependent friction model in the computational code since this friction model describes an earthquake cycle more completely. A 3D geological model with a 2D fault subject to fluid injection and production is run using the developed code. Results are shown in terms of seismic slips, fault tractions along with the stress distributions. Limitation of the simulation results and modeling approach is discussed at the end. Future work to improve the existing model is also discussed briefly.

Summary, future work, and conclusions are discussed in the final chapter.

CHAPTER II

LITERATURE REVIEW

2.1 Introduction

This chapter describes some literature relevant to coupled fluid flow and reservoir geomechanics, and how it is linked with fluid-induced seismicity. It starts out with the background study of geomechanics and poroelasticity explained through Terzaghi's experiment for 1D soil consolidation. It also resorts to Biot's theory of coupled fluid-soil interaction to identify some of the relevant poroelastic coefficients to help explain a coupled poroelastic problem. Governing equations for this coupled phenomenon are derived by combining a fluid mass balance equation and a mechanics momentum balance equation. Later in the chapter is shown how this coupled formulation can capture the capability of modeling induced seismicity by using appropriate fault constitutive models.

2.2 Geomechanics and Poroelasticity

Soil and rock have pore spaces and fractures which are filled with water. The deformation of these porous and fractured soil/rock depends on the stiffness of the media and fluid pressure inside those pore space. On the other hand, fluid pressure response is dependent on the hydraulic properties changes of the fluid such as porosity, permeability, tortuosity etc. The theory of consolidation or poroelasticity deals with the soil/rock deformation and the pore fluid pressure response interaction with that media. The theory was first developed by Terzaghi for a

one-dimensional case and later extended by Biot for three dimensional case.

Karl Terzaghi (1883-1963) elucidated the idea of theory of consolidation for a foundation material through a simplified experiment (Figure 2.1).

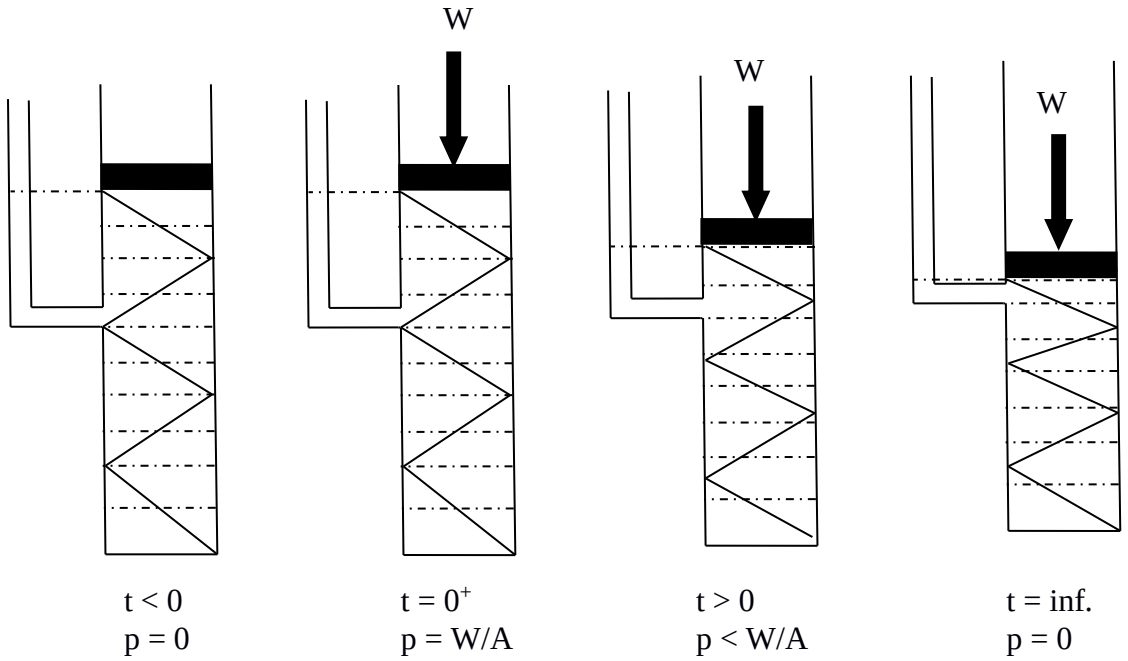

Figure 2.1 1D soil consolidation coupled with pore water pressure dissipation in Terzaghi's experiment

A fully saturated soil sample is laterally constrained and uniaxially loaded with a compressive load of W. Cross sectional area of the cylinder is A. At time $t = 0$, there is no application of load and there is no pore pressure ($p = 0$). At time $t = 0^+$, with the application of a uniaxially compressive load W, the pore pressure p rises to its undrained pressure response [Skempton, 1954] value of W/A in order to support that load. As time passes, stress from the fluid is being transferred to the solid particles and water leaks out through the drainage ($t > 0$). At infinite time excess pore water pressure will be zero and the total axial compressive stress will be completely transferred to the solid particles. Terzaghi derived a simplified pressure diffusion equation for this consolidation phenomenon:

$$\frac{\partial p}{\partial t} = c_v \frac{\partial^2 p}{\partial z^2} \qquad for\ t > 0 \tag{2.1}$$

where c is hydraulic diffusivity which is also known as consolidation coefficient, t is time, and z is distance along the soil column. Equation (2.1) is independent of stress leading to uncoupled interaction between soil consolidation and fluid diffusion [Wang, 2000]. The pressure evolution of Terzaghi's experiment is analogous to the heat conduction problem [Carslaw and Jaeger, 1959]. With Terzaghi's diffusion equation the concept of total stress, effective stress, and pore water pressure is very well-understood but without coupled interaction among them.

The effective stress is responsible for the solid deformation of a porous medium. It is defined as follows:

$$\sigma_{ij} = \sigma_{ij}^{'} + \alpha p \delta_{ij} \tag{2.2}$$

where σ_{ij} are the components of total stress, $\sigma_{ij}^{'}$ are the components of effective stress, α is Biot's coefficient, δ_{ij} are the Kronecker delta symbols, and p is pore water pressure. α is defined as follows:

$$\alpha = 1 - \frac{C_s}{C_m} \tag{2.3}$$

where C_s is compression modulus of the soil skeleton, and C_m is compression modulus of the porous medium.

2.3 Biot's Theory of Poroelasticity

Biot [Biot, 1941] extended Terzaghi's 1-D consolidation to 3D consolidation by introducing a quantity ζ called variation in water content which is defined as the increment of water volume per unit volume of soil. He showed that Terzaghi's 1-D consolidation problem is a special case of his theory. Increment of fluid mass content, ζ is defined as -

$$\zeta = \frac{\partial m_f}{\rho f_0} \tag{2.4}$$

where $\partial m_f = m_f - m_{f0}$; m_{f0} and ρ_{f0} are the fluid mass content and density at the reference state. The advantage of using ζ as a primary variable is that like strain, it is dimensionless and the constitutive equations do not have to include a density factor.

For an isotropic fluid-filled porous medium with an isotropic applied stress field σ, Biot's theory of poroelasticity can be expressed in two linear constitutive equations [Wang, 2000]:

$$\epsilon = a_{11}\sigma + a_{12}p \tag{2.5}$$

$$\zeta = a_{21}\sigma + a_{22}p \tag{2.6}$$

The volumetric strain $\epsilon = \frac{\partial V}{V}$ is positive in expansion and negative in compression. Increment in fluid content ζ is positive for fluid added to the control volume and negative for fluid flowing out of the control volume. Here, generic coefficients a_{ij} are used to emphasize simple and linear combination of constitutive relations. Eq. (2.5) represents the change in volume fraction as a function of applied stress and pore pressure. Eq. (2.6) states that changes in applied stress and pore pressure require the system to add or remove fluid from the storage. The poroelastic coefficients a_{ij} are defined as ratios of field variables by attributing various constraints on an elementary control volume.

$$a_{11} = \frac{\partial \epsilon}{\delta \sigma}|_{p=0} = \frac{1}{K} \tag{2.7}$$

$$a_{12} = \frac{\partial \epsilon}{\delta p}|_{\sigma=0} = \frac{1}{H} \tag{2.8}$$

$$a_{21} = \frac{\partial \zeta}{\delta \sigma}|_{p=0} = \frac{1}{H_1} \tag{2.9}$$

$$a_{11} = \frac{\partial \zeta}{\delta p}|_{\sigma=0} = \frac{1}{R} \tag{2.10}$$

The coefficient $\frac{1}{K}$ is obtained by measuring the change in volumetric strain due to changes in applied stress while keeping the pore pressure constant. This is why it is referred to as the compressibility of the material measured under drained conditions where K is the drained bulk modulus. The term $\frac{1}{H}$ indicates how much the bulk volume changes due to changes in pore pressure while keeping the applied stress constant. With analogy from the heat conduction problem, it is called as the poroelastic expansion coefficient. The coefficient $\frac{1}{H_1}$ is same as the $\frac{1}{H}$ for symmetric linear transformation matrix. The term $\frac{1}{R}$ is the ratio in the change in volume of water added to storage per unit volume divided by the change in pore water pressure and also referred as S_σ.

The three poroelastic coefficients viz. drained compressibility $\frac{1}{K}$, poroelastic expansion coefficient $\frac{1}{R}$, and unconstrained specific storage coefficient $\frac{1}{H}$ completely characterizes the poroelastic response of a porous medium under an isotropic applied stress. Together, they form a 2 x 2 symmetric matrix of three independent variables:

$$\begin{pmatrix} \frac{1}{K} & \frac{1}{H} \\ \frac{1}{H} & \frac{1}{R} \end{pmatrix}$$

where the drained compressibility and unconstrained storage coefficient are the diagonal terms and poroelastic expansion coefficient is the off-diagonal term of the symmetric matrix. This symmetry indicates that the value of $\frac{1}{H}$ for the coupling between strain and fluid pressure at constant stress is equal to the value for the coupling between increment of fluid content and stress at constant pressure.

By using the various values of poroelastic constants from Eqs. (2.7), (2.8), (2.9), and (2.10) into the constitutive equations (2.5) and (2.6) we get:

$$\epsilon = \frac{\partial V}{V} = \frac{1}{K}\sigma + \frac{1}{H}p \tag{2.11}$$

$$\zeta = \frac{1}{H}\sigma + \frac{1}{R}p \tag{2.12}$$

Two additional coefficients, Skempton's coefficient B and constrained specific storage coefficient are also defined here for the purpose of poroelasticity explanation.

Skempton's coefficient B is defined as the ratio of the induced pore pressure in an undrained case to the change in applied stress for undrained conditions:

$$B = -\frac{\partial P}{\partial \sigma}|_{\zeta=0} \tag{2.13}$$

The negative sign indicates that the decrease in pore pressure is associated with the increase in stress being transferred to the soil skeleton. The significance of Skempton's coefficient is that if a compressive stress is applied suddenly to a saturated porous medium, the induced pore pressure will be an undrained response and is given by the applied stress multiplied by B.

The constrained specific storage coefficient is defined as:

$$S_\epsilon = \frac{\delta \zeta}{\delta p}|_{\epsilon=0} = \frac{1}{M} \tag{2.14}$$

With the definition of various poroelastic constants, the stress and strain tensor become [Biot, 1941]:

$$\varepsilon_x = \frac{\sigma_{xx}}{E} - \frac{\nu}{E}(\sigma_{yy} + \sigma_{zz}) + \frac{\sigma}{3H}, \qquad \gamma_x = \frac{\sigma_{xy}}{G} \tag{2.15}$$

$$\varepsilon_y = \frac{\sigma_{yy}}{E} - \frac{\nu}{E}(\sigma_{zz} + \sigma_{xx}) + \frac{\sigma}{3H}, \qquad \gamma_y = \frac{\sigma_{yz}}{G} \tag{2.16}$$

$$\varepsilon_z = \frac{\sigma_{zz}}{E} - \frac{\nu}{E}(\sigma_{xx} + \sigma_{yy}) + \frac{\sigma}{3H}, \qquad \gamma_z = \frac{\sigma_{zx}}{G} \tag{2.17}$$

$$\zeta = \frac{1}{3H}(\sigma_{xx} + \sigma_{yy} + \sigma_{zz}) + \frac{\sigma}{R} \tag{2.18}$$

2.4 Governing Equations of Coupled Poroelasticity

In this section the governing equations for fluid flow and mechanical problems are introduced first. The governing equation for fluid flow is a mass balance equation whereas the governing equation for the mechanical problem is a stress equilibrium equation. Unlike quasistatic problem, where the wave propagation term is ignored, the mechanical problem in this research work is elastodynamic which means that a dynamic equilibrium is obtained for each time step of fluid flow problem since they are solved sequentially (details in Chapter 3). The equilibrium of a coupled poroelastic problem requires that if a stress or pressure field is applied to a porous and saturated medium, displacements and pore pressure within each representative element volume (REV) adjust instantaneously to maintain a state of internal force equilibrium. The deformation is computed from the material constitutive models that involve effective stress field. On the other hand, total stress is required to maintain the global equilibrium of the fluid-saturated porous medium. The linear poroelastic problem has to satisfy the mechanical equilibrium equations and the fluid continuity equation simultaneously and specify initial and boundary conditions.

Assume Ω be our interested domain and $\partial\Omega$ be its closed boundary. Then the governing equation for linear momentum balance of this soil-fluid system is-

$$\nabla \cdot \boldsymbol{\sigma} + \rho_b \boldsymbol{g} = 0 \tag{2.19}$$

Where $\boldsymbol{\sigma}$ is the Cauchy total stress tensor, $\boldsymbol{g}$ is the gravity vector, and ρ_b is the bulk density which can be expressed as-

$$\rho_b = \phi \sum_{\boldsymbol{\beta}}^{\boldsymbol{n_{phase}}} \rho_\beta S_\beta + [1-\phi]\rho_s \tag{2.20}$$

Where ρ_b is the density of fluid phase β

S_β is the saturation of fluid phase β

$\rho_s\ is$ the density of the solid phase

ϕ is the true porosity defined as the ratio of pore volume (V_p) to the bulk volume (V_b) in the current configuration n_{phase} is the number of fluid phases.

Assuming fluids are immiscible in a multiphase system the mass conservation equation is-

$$\frac{dm_\alpha}{dt} + \nabla \cdot \boldsymbol{w}_\alpha = \rho_\alpha f_\alpha \tag{2.21}$$

Where $\frac{dm_\alpha}{dt}$ is the accumulation term describing fluid mass variation with time f_α is volumetric source term for phase α

$\boldsymbol{w}_\alpha$ is the mass flux of fluid phase α relative to the solid skeleton and is given by-

$\boldsymbol{w}_\alpha = \rho_f \boldsymbol{v}, \boldsymbol{v}$ is the seepage velocity relative to the deforming skeleton and is given by-

$$\boldsymbol{v} = -\frac{\boldsymbol{k}}{\boldsymbol{\mu}}(\nabla \mathrm{p} - \rho_f)\boldsymbol{g} \tag{2.22}$$

where k is the intrinsic permeability tensor, μ is the fluid dynamic viscosity and p is the pore fluid pressure.

Governing Eqs. (2.19) and (2.21) define a solid-fluid coupled system where they are viewed as overlapping continua. In this coupled system, if there are changes in pore fluid pressure then there will be changes in effective stress causing deformation in the porous media. Conversely, the deformation in the porous media induces changes in fluid mass content and

pressure.

Biot [1941] linked changes in strain and fluid content with changes in total stress and fluid pressure. Coussy [1995] expressed Biot's coupling formulation in the following forms -

$$\partial \boldsymbol{\sigma} = \boldsymbol{C}_{dr} : \varepsilon - b\delta p \mathbf{1} \tag{2.23}$$

$$\zeta = b\varepsilon_v + \frac{1}{M}\delta p \tag{2.24}$$

where $\boldsymbol{C}_{dr}$ is the rank-4 drained elasticity tensor, $\mathbf{1}$ is the rank-2 identity tensor, ε is the linearized strain tensor and is defined as-

$$\varepsilon = \frac{1}{2}(\nabla \boldsymbol{u} + \nabla^T \boldsymbol{u}) \tag{2.25}$$

$$\varepsilon_v = tr(\varepsilon), \qquad volumetric\ strain \tag{2.26}$$

From the Eqs. (2.23) and (2.24) above, it is clear that Biot's theory of poroelasticity has two coupling coefficients, Biot Modulus M, and Biot coefficient b. Coussy [1995] showed that these coupling coefficients are related to rock and fluid properties as follows-

$$\frac{1}{M} = \phi_0 c_f + \frac{b - \phi_0}{K_s} \tag{2.27}$$

$$b = 1 - \frac{K_{dr}}{K_s} \tag{2.28}$$

where,

$c_f = \frac{1}{K_f}$ is the fluid compressibility

K_f is bulk modulus of the fluid

K_s is the bulk modulus for solid skeleton

K_{dr} is the drained bulk modulus of the porous medium

Assuming small elastic deformations, Eqs. (2.23) and (2.24) can be rewritten based on reference state as-

$$\sigma - \sigma_0 = \boldsymbol{C}_{dr} : \varepsilon - b(p - p_0)\mathbf{1} \tag{2.29}$$

$$\frac{1}{\rho_{f,0}}(m - m_0) = b\varepsilon_v + \frac{1}{M}(p - p_0) \tag{2.30}$$

Substituting Eq. (2.27) into Eq. (2.21) for a single phase flow, the fluid mass balance equation is obtained in terms of pressure and volumetric strain-

$$\frac{1}{M}\frac{\partial p}{\partial t} + b\frac{\partial \varepsilon_v}{\partial t} + \nabla \cdot \boldsymbol{v} = f \tag{2.31}$$

The linearized relation between volumetric total stress and volumetric strain with respect to the reference state can be expressed as follows-

$$\delta\sigma_v = \sigma_v - \sigma_{v,0} = K_{dr}\varepsilon_v - b(p - p_0) \tag{2.32}$$

Using the above relation and $m = \rho_f \phi$, the change in porosity can be expressed as-

$$\frac{\rho_f}{\rho_{f,0}}(\phi - \phi_0) = \frac{b}{K_{dr}}\left(\sigma_v - \sigma_{v,0}\right) + \left(\frac{b^2}{K_{dr}} + \frac{1}{M}\right)(p - p_0) \tag{2.33}$$

Eq. (7) can be rewritten as-

$$\left(\frac{b^2}{K_{dr}} + \frac{1}{M}\right)\frac{\partial p}{\partial t} + \frac{b}{K_{dr}}\frac{\partial \sigma_v}{\partial t} + \nabla \cdot \boldsymbol{v} = f \tag{2.34}$$

Both Eqs. (2.31) and (2.34) are equivalent for fluid flow and geomechanical coupling but they lead to different operator splits: fixed-strain split and fixed-stress split [Kim et al., 2011b]. It is noted from these two equations that there are no explicit quantities like fluid and rock compressibility to account for geomechanical coupling, rather these quantities are determined from the poroelastic coefficients K_{dr}, b, and M.

2.4.1 Initial and boundary conditions

In order to fully describe the coupled fluid flow and geomechanical mathematical problem it is necessary to specify the initial and boundary conditions. For the flow problem a

prescribed pressure boundary condition $p = \bar{p}$ is specified on Γ_p, and a prescribed volumetric flux $\boldsymbol{v}.\boldsymbol{n} = \bar{v}$ is specified on Γ_v, where n is an outward unit normal vector to the boundary ∂V. In order to satisfy the well-posedness of the mathematical boundary value problem, we let

$$\Gamma_p \cap \Gamma_v = \emptyset$$

$$\Gamma_p \cup \Gamma_v = \partial V$$

For the mechanical problem we specify a prescribed displacement of $\boldsymbol{u} = \bar{u}$ on Γ_u and a prescribed traction of $\boldsymbol{\sigma} \cdot \boldsymbol{n} = \bar{\boldsymbol{t}}$ on Γ_σ. We also let

$$\Gamma_u \cap \Gamma_\sigma = \emptyset$$

$$\Gamma_u \cup \Gamma_\sigma = \partial V$$

The initial conditions of a coupled geomechanical problem should represent an equilibrium condition for each of the sub-problems i.e. hydrostatic equilibrium of $p|_{t=0} = p_0$ for the fluid flow part and geostatic equilibrium of $\sigma|_{t=0} = \sigma_0$ for the mechanical part.

2.5 Time Scale Characteristics

Equilibrium conditions for fluid flow and mechanical deformations have different time scale characteristics especially for the stable time step integration in the individual codes. Fluid flow problems are transient whereas mechanical equilibrium is almost instantaneous in quasi-static problems. Fluid flow is a long term process where dissipation of pressure occurs through diffusion process that could take days, months, or years. For dynamic problems, mechanical deformation and stress change in a continuum involve propagation of wave in an REV which requires a finite amount of time. Stable time is calculated based on the time required for a wave to propagate in the shortest path of an REV.

For a coupled fluid flow and geomechanics interaction problem, there are two

characteristic time scales [Jha, 2005]:

$$t_c^{fluid} = \frac{\mu L_c^2}{k}\left(\frac{1}{M} + \frac{b^2}{K_0 + \frac{4}{3}G}\right) \tag{2.35}$$

where t_c^{fluid} is the characteristic time for fluid flow equilibrium, L_c is the characteristic length of the smallest element of fluid-solid system, and K_0 is the undrained bulk modulus of the porous media. The relationship between undrained and drained bulk modulus is:

$$K_0 = K + b^2 M \tag{2.36}$$

Mechanical characteristic time is given by -

$$t_c^{mech} = \left(\sqrt{\frac{\rho}{K_0 + \frac{4}{3}G}}\right) L_c \tag{2.37}$$

The diffusion process in the system takes place based on the ratio of those expressions above. Assuming b = 1, we get:

$$\frac{t_c^{fluid}}{t_c^{mech}} = \sqrt{\frac{K_0 + \frac{4}{3}G}{\rho}}\frac{L_c}{k/\mu}\left(\frac{1}{M} + \frac{b^2}{K_0 + \frac{4}{3}G}\right) \tag{2.38}$$

The advantage of having knowledge about the characteristic time scales for a coupled fluid flow and geomechanics problem includes:

- discretion of choosing a suitable transient scale
- selection of appropriate linear solver for each of the processes
- setting up numerical validation cases for experiments

2.6 Uncoupling of Stress from Pore Pressure

Analogous to uncoupled quasistatic theory in thermoelasticity [Boley and Weiner, 1960],

in poroelasticity, uncoupling of stress from pore water pressure means that the mechanical coupling term in the fluid pressure diffusion equations is omitted. This is what Terzaghi provided in terms of 1-D fluid diffusion equation. Although uncoupled, it still involves one-way coupling i.e. changes in fluid pressure do produce stress and strains, but changes in stress field do not affect the fluid pressure [Wang, 2000]. The simplification of this uncoupled problem signifies that the transient fluid flow equation in pressure can be solved independently of the time-dependent stress or strain field. By solving them independent of one another, the resulting pore pressure field output can then be used as input in the mechanical problem to account for the effective stresses in the material constitutive models.

There are four special circumstances [Wang, 2000] where the inhomogeneous pore water diffusion equation is uncoupled from the mechanical equilibrium equations: steady state problems, problems involving uniaxial strain and constant vertical stress, problems involving highly compressible fluid, and problems having irrotational displacement field in an unbounded domain.

2.7 Pore Compressibility in Geomechanical Coupling

When a stress field is applied to a fluid-saturated porous media, there is a deformation in the solid skeleton causing the pore spaces to be squeezed. The reduction in the volume of these pore spaces cause the fluid to leak out of the pore space. The drained pore compressibility is defined as the ratio of pore volume change to the change in confining pressure while still maintaining constant pore pressure. It is given by -

$$\frac{1}{K_p} = \frac{\alpha}{\phi K} \tag{2.39}$$

where ϕ is the porosity of the porous medium.

Typically, in conventional reservoir simulation of a coupled hydro-geomechanical problem a term called 'pore compressibility', $c_p = \frac{1}{K_p}$ is used in the pressure computation in order to account for poroelastic effect of solid-fluid coupling [e.g. Settari and Mourits, 1998; Kim et al., 2009].

c_p is expressed as-

$$(\phi_0 c_f + \phi_0 c_p)\frac{\partial p}{\partial t} + Div\, \boldsymbol{v} = f \tag{2.40}$$

Although pore compressibility is not an intrinsic property of the porous media due to its dependency on the stress and boundary conditions, its use in reservoir simulation simplifies the computation of stress and strain changes. A porosity correction term $\Delta\phi$ used by Mainguy and Longuemare [Mainguy and Longuemare, 2002] based on Eq. (2.8) is given below:

$$\Delta\phi = \left(\phi_0 c_p + \frac{\phi_0}{K_s} - \frac{b}{K_{dr}}\right)\frac{\partial p}{\partial t} - \left(\frac{1}{K_{dr}} - \frac{1}{K_s}\right)\frac{\partial \sigma_v}{\partial t} \tag{2.31}$$

Under the fixed-stress split solution scheme using Eqs. (2.6), (2.11), and (2.12) it is shown by Kim et al. [2009]:

$$\phi_0 c_p|_{sn} = \frac{b - \phi_0}{K_s} + \frac{b^2}{K_{dr}} \tag{2.41}$$

where, $\frac{b}{K_{dr}}\frac{\partial \sigma_v}{\partial t}$ is a correction term from the mechanical solution.

2.8 Poroelastic Effects in Rock Mechanics

Porous media tend to dilate in volume when they are flooded with water. If the soil is constrained, it experiences a confining pressure i.e. compressive stresses. This is known as poroelastic effect of rock. It has been identified that an isotropic poroelastic material needs four

independent constitutive coefficients to characterize its mechanical behavior [Cheng et al. 1993]. These are soil shear modulus G, drained bulk modulus K, Biot effective stress coefficient α, and Biot modulus M. According to Fairhurst and Haimson, a poroelastic coefficient is given by -

$$\eta = \frac{\alpha(1-2v)}{2(1-v)} \tag{2.42}$$

The value of the poroelastic coefficient v varies between 0 and 0.5. Here α is another coefficient that is associated with the bulk moduli of the skeleton, K and the solid constituent, K_S.

$$\alpha = 1 - K/Ks \tag{2.43}$$

When a soil specimen is subject to an incremental compressive stress of ΔP in an undrained condition, the ratio of the pore pressure rise Δp to the applied compressive stress is termed as Skempton pore pressure coefficient, B.

$$B = \frac{\Delta p}{\Delta P} \tag{2.44}$$

This coefficient is a composite property of solid and fluid.

2.9 Hydro-mechanical Coupling

In dealing with earth sciences, coupled hydromechanical (HM) processes are found in various natural and human induced activities such as landslides, dam failure, reservoir impoundment, fluid injection, and so on. The term 'HM coupling' refer to the interaction between hydraulic and mechanical processes. The coupled process is highly nonlinear making the modeling task a challenging one. Coupling HM process involves coupling of stress and permeability or, in other words, rock deformation with fluid flow. Laboratory and field data show that permeability dependence on fracture rock is more sensitive at shallow depth with low in situ permeability [Rutqvist and Stephansson, 2003]. Conversely, in highly fractured and

permeable zone permeability is not so much sensitive to the stress changes. It is recommended to use in situ characterized HM properties due to their high variability in fractured rock and difficulties in using laboratory data. Figure 2.2 illustrates volumetric deformation of a porous and fractured rock subject to confining pressure and pore-water pressure. It also schematically shows shear and normal deformation of fractured and porous media.

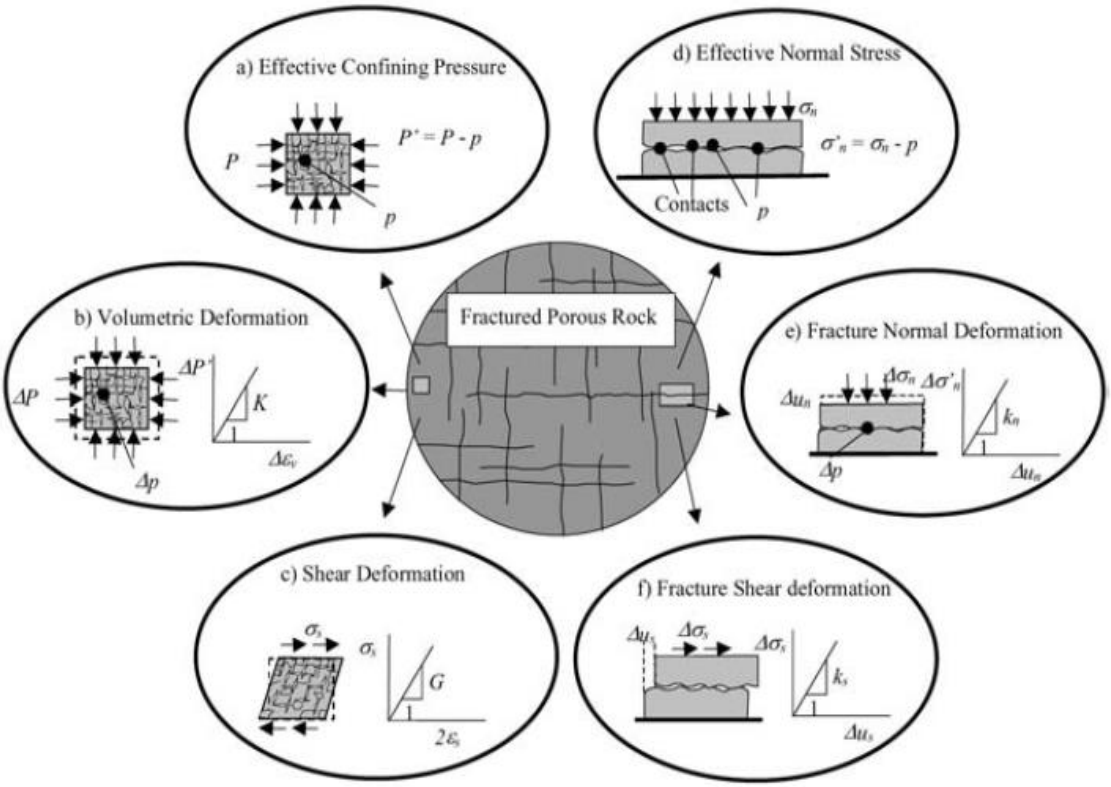

Figure 2.2 Illustration of porous and fractured rock associated with confining pressure and various types of deformation

When an external load is applied to fluid saturated porous or fractured rock, deformation takes place in the rock changing its pore volume. Deformation of the rock compresses the pore volume within itself and squeezes the water out. If the external load is applied rapidly in a manner such that the fluid has no time to escape then the pore water pressure develops in a situation referred to as undrained HM response. But if the external load is applied gradually so

that there is enough time for pore water to squeeze out without developing pressure inside the rock pore space then that situation is referred to as drained HM response. Similarly, reduction in pore pressure results in reduction in pore volume causing consolidation or settlement [Biot, 1941].

The HM couplings described above is termed as "direct" HM couplings [Wang, 2000]. These couplings include:

i. A solid-to-fluid coupling that accounts for the change in fluid mass or pressure due to change in applied stress
ii. A fluid-to-solid coupling that accounts for the change in porous medium volume due to change in fluid pressure or mass

Figure 2.3 shows the "direct" HM couplings with appropriate labels. Change in porous medium volume can change the hydraulic and material properties which are considered as "indirect" HM couplings [Rutqvist and Stephansson, 2003]. Rutqvist [1995a] combined Goodman's [1974] model to provide a complete relationship between fracture transmissivity and effective normal stress.

The "indirect" HM couplings include [Fig. 2.5]:

i. A solid-to-fluid coupling that results in a change hydraulic properties due to change in applied stress
ii. A fluid-to-solid coupling that results in a change in mechanical properties due to change in fluid pressure

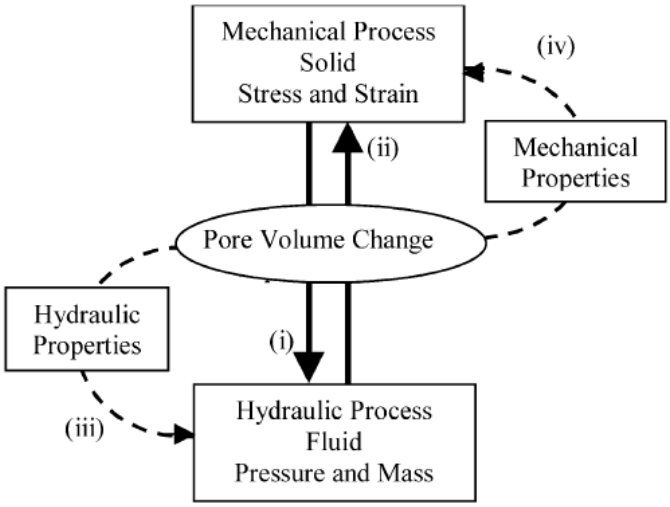

Figure 2.3 Illustration of direct and indirect coupling [Rutqvist and Stephansson, 2003]

$$T = C\left[b_{hi} + \frac{\sigma_{ni}^{'}}{k_{ni}}\left(1 - \frac{\sigma_{ni}^{'}}{\sigma_{ni}^{'}}\right)\right]^3 \tag{2.45}$$

where, $\sigma_{ni}^{'}$ is initial effective normal stress, b_{hi} is initial apparent hydraulic aperture, k_{ni} is initial hydraulic normal stiffness, and C is constant which depends on flow geometry and fluid properties. The most widely used fracture closure model under effective normal stress is given by Walsh [1981]:

$$T = T_0\left[1 - \left(\frac{\sqrt{2}h_e}{b_0}\ln\frac{\sigma_{ni}^{'}}{\sigma_{ni}^{'}}\right)\right]^3 \tau_w(\Delta\sigma_n^{'}) \tag{2.46}$$

where T_0 and b_0 are joint transmissivity and aperture at some reference effective stress, $\sigma_n^{'}$, τ_w is the tortuosity factor that depends on the normal stress, h_e is standard deviation of the asperity height distribution.

In the coupled code two failure mechanisms are considered to redistribute the permeability after a potential fracture or fault slip. First one is shear reactivation due to the reduction in effective stress as a result of increased pore fluid pressure.

2.10 Fluid Induced Permeability Changes

Fault reactivation in dealing with permeability evolution to the context of CO_2 sequestration have been modeled by both finite thickness solid element and zero thickness interface element [Cappa and Rutqvist, 2010]. The modeling results do not show any difference in the elasto-plastic behavior of the fault zone. They showed that the shear-enhanced permeability and fault reactivation are more likely to occur at the faulted reservoir locations where fluid is injected. Reservoir stress conditions coupled with fluid injection in the vicinity of fault zones may potentially nucleate, propagate, and arrest from low to moderate earthquakes [Hickman et al., 1995; Sibson and Rowland., 2003; Wibberly and Shimamoto, 2005].

A fault zone in the earth's upper crust usually consists of two distinct regions – a fault core having low permeability and a damage zone having relatively higher permeability [Vermilye and Scholz,1998; Gudmundsson, 1999, 2000; Wibberley and Shimamoto, 2003; Faulkner et al., 2003; Cappa et al., 2007; Guglielmi et al., 2008; Mitchell and Faulkner, 2009; Cappa, 2009]. It was shown that the permeability of the fault zone changes with earthquake slip and associated stress reduction [Uehara and Shimamoto, 2004]. Field data and models show that both the damage zones and fault cores increase in thickness with increased slip [Vermilye and Scholz, 1998]. Consequently, fault zones having higher amount of fractures also grow and allow more fluid to pass through porous and fractured media.

The range of damage zone width can extend from meters for a single core to kilometers for multiple cores [Caine et al., 1996; Gudmundsson, 2004; Mitchell and Faulkner, 2008, Wilson et al., 2003] indicating a vast area that may have more probability of fluid injection.
As shown in Figure 2.4, permeability in a fault core can range from 10^{-17} to 10^{-21} whereas in the damaged zones it can range from 10^{-14} to 10^{-16}. Young's modulus can range from 10 GPa in the

fault core to 50 GPa in the damaged zones [Gudmundsson, 2004; Faulkner et al., 2006]. When fluid is injected in a reservoir rock, pore pressure increases resulting in lowering of the stress according to the Terzaghi's stress law:

$$\sigma_n^{'} = \sigma_n - P \tag{2.47}$$

where $\sigma_n^{'}$ is the effective normal stress, σ_n is the total normal stress and P is pore water pressure. The Mohr-Coulomb failure criteria [Jaeger and Cook, 1979] is given by-

$$\tau = c + \mu_s \sigma_n^{'} \tag{2.48}$$

where τ is the critical shear stress, c is the cohesion, and μ_s is static coefficient of friction.

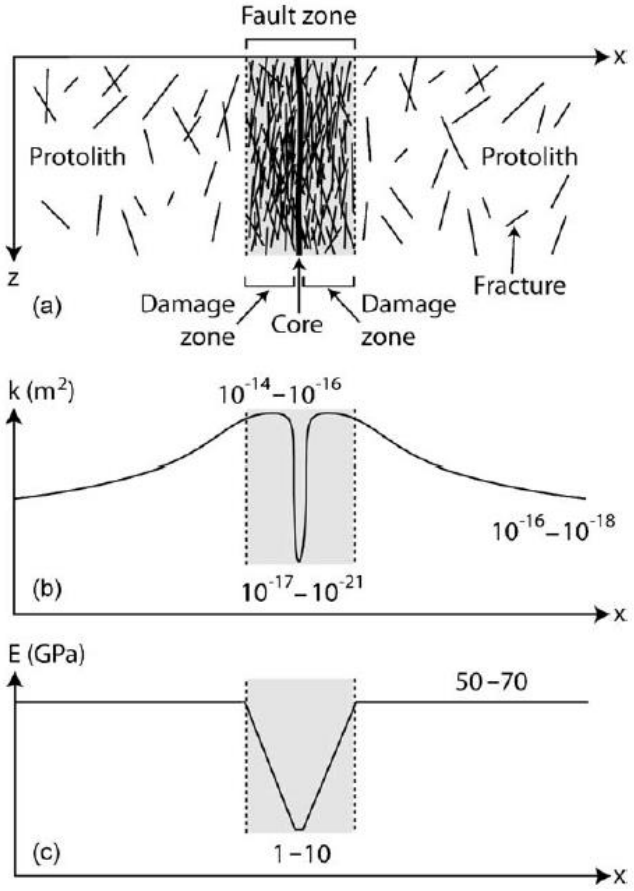

Figure 2.4 Schematic showing fault core and damage zone with their permeability and Young's modulii [Rutqvist and Stephansson, 2003]

The normal stress σ_n and shear stress τ is calculated using the following equations:

$$\sigma_n = \frac{\sigma_1 + \sigma_3}{2} - \frac{\sigma_1 - \sigma_3}{2}\cos[2\delta] \tag{2.49}$$

$$\tau = \frac{\sigma_1 - \sigma_3}{2}\sin[2\delta] \tag{2.50}$$

where σ_1 is maximum principal stress, σ_3 is minimum principal stress and δ is the angle between the fault plane and the σ_1 direction. Eqs. (2.1) and (2.2) indicate that increase in pore water pressure, P reduces the effective stress thereby reducing the shear strength of a given fault. The ratio of $\frac{\tau}{\sigma_n'}$ is termed as "ambient stress ratio" which is a measure of slip tendency. If the value of "ambient stress ratio" exceeds the coefficient friction, μ_s then the slip occurs. For most rocks, based on laboratory tests, μ_s varies from 0.6 to 0.85 [Byerlee, 1978].

2.11 Permeability Coupling Representation

The hydraulic and mechanical behavior of a single-fault plane can be modeled by using zero-thickness interface elements. These elements can represent flow transmissivity and fracture normal and shear stiffness. The cubic law for relation between flow along an open fracture and fracture aperture is given by-

$$T = \frac{b_h^3 \rho g}{12\mu} \tag{2.51}$$

where T is the fault transmissivity and $b_h$is fracture aperture, $\rho \; and \; \mu$ are fluid density and viscosity, respectively, and g acceleration of gravity. Fracture aperture is affected by the mechanical deformation thus changing the fault transmissivity [Witherspoon et al., 1980].

$$T = \frac{[b_h + \Delta b_h]^3 \rho g}{12\mu} \tag{2.52}$$

Where Δb_h is the change in hydraulic aperture due to mechanical deformation. This is

proportional to the changes in fracture normal displacement u_n.

$$\Delta b_h = f \cdot \Delta u_n \tag{2.53}$$

Where f denotes a friction factor accounting for roughness of the fracture surface and Δu_n denotes changes in fracture normal displacement. Δu_n results from the changes in fracture normal stress $\Delta\sigma_n$ or shear dilation u_s or combination of two [Cappa and Rutqvist, 2010].

Hydromechanical properties of rock can be idealized as isotropic if the fault core is homogeneous and unfractured or the damaged zone is highly fractured [Cappa and Rutqvist, 2010]. In such cases, permeability and porosity changes may be related to the mean stress or volumetric strain and assumed to possess equal hydraulic properties along and across the fault. In such cases, a simple permeability model [Zoback and Byerlee, 1975] may be used. Rutqvist et al. used an isotropic model developed and applied by Chin et al. [2000] for modeling of permeability changes in petroleum reservoirs:

$$\phi = 1 - [1 - \phi_i]e^{-\varepsilon_v} \tag{2.54}$$

$$k = k_i \left(\frac{\phi}{\phi_i}\right)^n \tag{2.55}$$

where ϕ is the porosity at a given stress, ϕ_i is the initial porosity, ε_v is volumetric strain, k is the permeability at a given stress, k_i is the initial permeability, and n is a power-law exponent. The above formula allows for consistent permeability correction for both elastic and plastic mechanical behavior.

In case of anisotropic elasto-plastic constitutive model, permeability change is approximated using a nonlinear normal stress versus permeability function with the option of plastic strain dilation [Hsiung et al., 2005]:

$$\frac{k}{k_i} = \left[\frac{a}{c[c\sigma_n^{'} + 1]}\frac{1}{b_{hi}} + \frac{e_{ftp} + e_{fsp}\tan\psi}{f_d b_{hi}}\right]^3 \tag{2.56}$$

where a and c are empirical constants for normal-closure hyperbola, e_{ftp} is the plastic strain caused by tensile failure, e_{fsp} is the plastic shear strain, b_{hi} is the initial fracture aperture, f_d is the fracture frequency [1/spacing], and ψ is dilation angle.

2.12 Multiphase Poroelasticity

Unlike single phase poroelasticity, it is not possible to linearize stress increment equation [Coussy, 1995] The following reasons are attributed to that -

1. Unlike water or liquid gases are highly compressible. In a multiphase system gaseous phases coexist with liquid phases for which the theory of single phase poromechanics does not hold.
2. Capillary pressures are nonlinear

For multiphase poroelasticity an effective stress formulation for constitutive modeling of porous media is proposed by Bishop et al. [Bishop, 1959; Bishop and Blight, 1963]. They propose that one part of total stress contributes to the deformation of the solid skeleton while the other part induces changes in fluid pressure.

$$\partial \boldsymbol{\sigma} = \boldsymbol{C}_{dr} : \delta\varepsilon - \sum_{\beta}^{n_{phase}} b_\beta \, \delta p \mathbf{1} \tag{2.57}$$

Where, b_β corresponds to the Biot coefficients for phases existing in the multiphase system. It is obvious that

$$\sum_{\boldsymbol{\beta}}^{\boldsymbol{n_{phase}}} b_\beta = b \tag{2.58}$$

Several authors [Lewis and Sukirman, 1993; Coussy et al., 1998 Lewis and Schrefler, 1998] assumed that Biot coefficients b_β are proportional to the individual saturations S_β. The advantage

of using effective stress in multiphase system is that we can treat that as a single-phase continuum [Khalili et al., 2004; Nuth and Laloui, 2008; Vlahinic et al., 2011; Nikooee et al., 2013; Kim et al., 2013]. For a multiphase linear poroelasticity, the stress-strain relationship becomes [Jha and Juanes, 2014]:

$$\partial \boldsymbol{\sigma} = \partial \boldsymbol{\sigma}' - b\delta p \mathbf{1} \tag{2.59}$$

$$\partial \boldsymbol{\sigma}' = \boldsymbol{C}_{dr} : \delta \varepsilon \tag{2.60}$$

For multiphase poromechanics Eq. (2.24) can be extended as:

$$\left(\frac{dm}{\rho}\right)_{\alpha} = b_{\alpha} d\varepsilon_v + \sum_{\boldsymbol{\beta}}^{\boldsymbol{n_{phase}}} N_{\alpha\beta} dp_{\beta} \tag{2.61}$$

Where $\boldsymbol{N} = \boldsymbol{M}^{-1}$ is the inverse of Biot modulus and positive definite tensor whereas Biot coefficient b is a vector. For a two-phase water-gas system, $N_{\alpha\beta}$ can be expressed as a function of fluid pressure, saturations, displacement, and rock and fluid properties [Jha and Juanes, 2014] as follows:

$$N_{gg} = -\phi \frac{\partial S_w}{\partial P_{wg}} + \phi S_g c_g + S_g^2 N \tag{2.62}$$

$$N_{gw} = N_{wg} = \phi \frac{\partial S_w}{\partial P_{wg}} + S_g S_w N \tag{2.63}$$

$$N_{ww} = -\phi \frac{\partial S_w}{\partial P_{wg}} + \phi S_w c_w + S_w^2 N \tag{2.64}$$

Where $N = (b - \phi)[1 - b]/K_{dr}$ and subscripts w and g refer to water and gas.

By substituting Eq. (2.63), (2.64), and (2.65) into Eq. (2.21), we obtain the multiphase flow equation:

$$\frac{\partial}{\partial t}\left(\rho_{\alpha} \sum_{\boldsymbol{\beta}}^{\boldsymbol{n_{phase}}} \left(N_{\alpha\beta} + \frac{b_{\alpha} b_{\beta}}{K_{dr}}\right) p_{\beta}\right) + \frac{1}{K_{dr}} \frac{\partial}{\partial t}(\rho_{\alpha} b_{\alpha} \sigma_v) + \nabla \cdot \boldsymbol{w}_{\alpha} = \rho_{\alpha} f_{\alpha} \tag{2.65}$$

2.13 Fluid-induced Seismicity Mechanism

Injection of fluid in the subsurface porous and fractured rocks increases the pore water pressure. Pressure is used to calculate effective normal stress according to Terzaghi's principle [see Terzaghi et al., 1996]:

$$\sigma_n^{'} = \sigma_n - P \tag{2.66}$$

Where $\sigma_n^{'}$ is effective normal stress, σ_n is total normal stress, P is pore water pressure, and compressive stress is considered positive.

Reduction in effective stresses reduces the shear strength according to the Mohr-Coulomb failure criterion [Hubbert et al., 1959]:

$$\tau = c + \mu\sigma_n^{'} \tag{2.67}$$

Where, τ is critical shear stress, c is cohesion, and μ is the coefficient of friction. The slip potential is calculated from the reduction of shear strength at the predefined faults or fractures. The occurrence of an earthquake on a fault or fracture alters the stress conditions throughout the entire domain. The new stress condition, in conjunction with the ongoing fluid injection, accounts for an updated potential of seismic slip generation and dynamic rupture wave propagation which goes on throughout the entire period of injection activities.

2.14 Permeability Evolution from Fault Slip

During an earthquake slip, permeability along the fractured and porous damage zone is redistributed due to changes in porosity and diminution of contacts between the fault asperities. In the mature faults, permeability would be very low across the fault core while it would be really high along the fault plane [e.g., Sibson, 1977; Chester et al., 1993] due to presence of fractures. Furthermore, permeability may be substantially different on the two sides of the fault

after a seismic slip [Sibson, 1990]. In order to accurately model multiple fluid-induced earthquake cycles it is important to account for these slip-dependent permeability changes.

Figure 2.5 shows a fault damage zone (thick solid black line) of width b and a finite thickness fault with aperture e_h. The fault is subject to an effective normal stress σ_n'. Frictional shear stress in the fractures is given by-

$$\tau_f = \frac{e_h^3 \rho g}{12\mu} \tag{2.68}$$

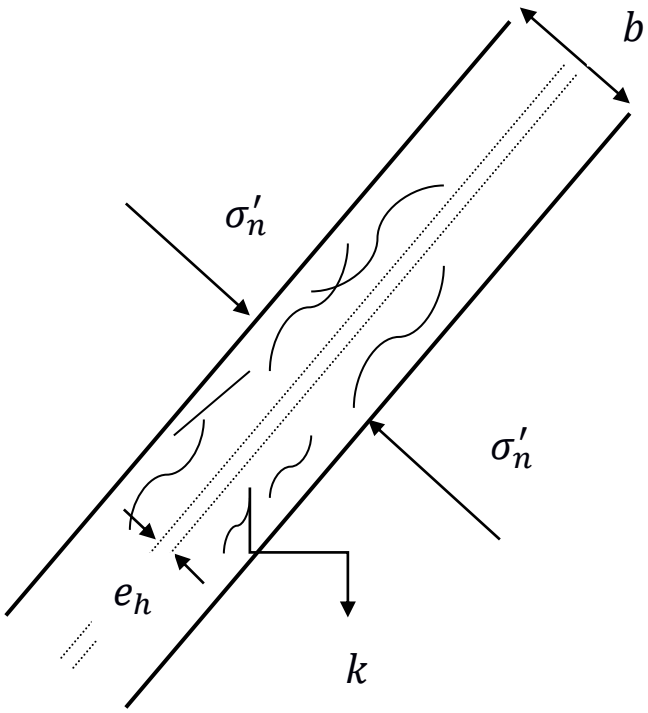

Figure 2.5 Permeability changes in a faulted zone subject to normal opening and shear slips

The transmissivity in the damage zone is given by [Cappa and Rutqvist; 2011]:

$$T = \frac{k\rho g}{\mu} \cdot b \tag{2.69}$$

At failure, $T = \tau_f$. From Eqs. (2.69) and (2.70) we get:

$$k = \frac{e_h^3}{12\mu b} \tag{2.70}$$

$$Now, \qquad e_h = e_{ih} + \Delta u_n$$

$$and \qquad \Delta u_n = \Delta u_s \cdot \tan d$$

Inserting this expression in Eq. (2.71) we get the permeability modification for shear reactivation:

$$k = \frac{(e_{ih} + \Delta u_s \cdot \tan d)^3}{12\mu b} \tag{2.71}$$

2.15 Fault Slip Modeling

Faults can be represented either as a two-dimensional surface [Juanes et al., 2002] or a three-dimensional zone [Rutqvist et al., 2008]. It is advantageous to represent faults as surfaces over 3D zones. First it is easier to describe the localized displacement at the interface where the domain is discontinuous. Second, one can use dynamic fault friction models in order to simulate dynamic rupture process of a fault. A fault surface is a zero thickness element that is very widely used in the finite element literature [Goodman et al., 1968; Beer, 1985; Carol et al., 1985; Gens et al., 1988; Lei et al., 1995]. A fault surface allows us to model discontinuous displacements across that fault in order to estimate slip.

A domain decomposition approach [Aagaard et al., 2013] is adopted in order to model fault slip by means of finite element formulation. This approach is applicable to both quasi-static and dynamic simulations of fault rupture propagation. An earthquake cycle consists of an interseismic period where the deformation rate is very slow and a coseismic period where the deformation rate is very high. Also the spatial and temporal scales of earthquake rupture propagation are very complex to model. The domain decomposition approach includes the features that can model this huge variety of complexity. It includes modeling fault rheologies

with elastic, viscoelastic, and viscoelastoplastic constitutive models. It also capitalizes the finite element data structure using parallel computation which makes the simulation much more efficient and faster.

In a domain decomposition approach [Aagaard et al., 2014], a fault is represented by a surface (Figure 2.6) which has two sides – a positive side and a negative side. A fault normal vector n is used to specify the direction of positive side from negative side. A slip is calculated as the relative displacement of the positive side of the fault to negative side.

Mathematically, $(\boldsymbol{u}_+ + -\boldsymbol{u}_-) - \boldsymbol{d} = 0 \; on \; S_f$

Where $\boldsymbol{u}_+ \; \boldsymbol{and} \; \boldsymbol{u}_-$ are the displacements on the positive and negative sides of the fault, $\boldsymbol{d}$ is the fault slip vector which is dictated by the effective traction on the fault. $\boldsymbol{u}$ represents displacement

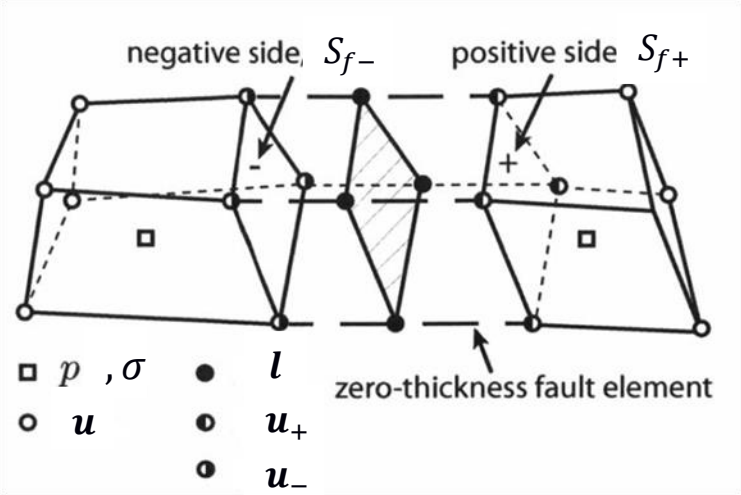

Figure 2.6 Locations of the pressure p, displacement, u and Lagrange multiplier, l in modeling and computing slips on fault [Jha, 2014]

at the regular nodes. To calculate the slip vector $\boldsymbol{d}$ or the relative motion of the positive fault surface S_{f+}, in relation to the negative fault surface S_{f-}, zero volume cohesive cells are inserted along the fault plane to allow for additional degrees of freedom (DOFs) (Figure 2.7). These additional DOFs are used to calculate dislocations or jumps in the displacement field across the

fault. The dislocations in the 3D model correspond to lateral and reverse shear slip, and to Mode I fault opening. PyLith can simulate either kinematic or dynamic rupture propagations on the fault. Fault tractions are indicative of elastic strains accumulated in the fault zone. In domain decomposition approach, the effective traction is modeled by introducing a Lagrange multiplier, l which is defined as the force per unit area required to hold an equilibrium condition for a given slip vector d across the fault.

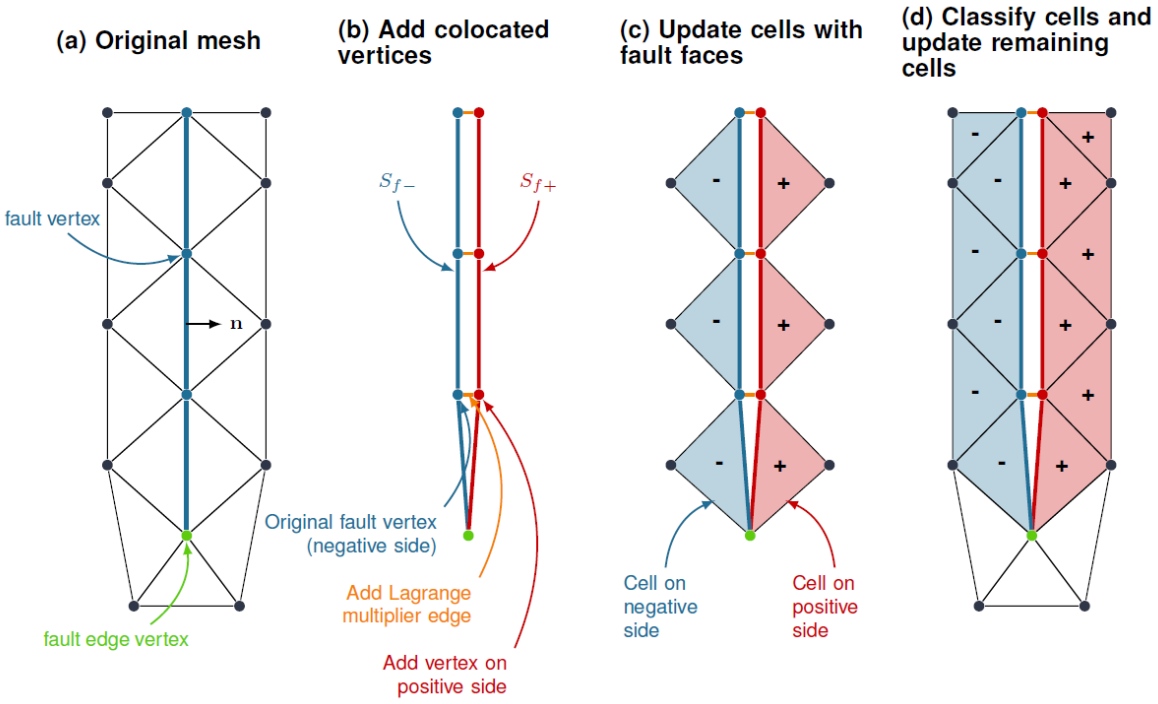

Figure 2.7 Illustration of fault slip calculation by means of zero thickness cohesive cells [Aagaard et al., 2014]

Mathematically,

$$\sigma_n^{'} = \boldsymbol{l}.\boldsymbol{n} \tag{2.72}$$

The fault tractions are equal and opposite on the two sides of the fault in order to satisfy the equilibrium condition. The corresponding shear traction acting tangentially on the fault surface is given by-

$$\tau = |\sigma_n^{'} - \boldsymbol{l}.\boldsymbol{n}| \tag{2.73}$$

Under this approach, a fault surface consists of nodes similar to 'split nodes' used in a number of finite element and finite difference codes.

The 'split nodes' technique form a diagonal Jacobian in order to solve the fault tractions of the uncoupled equations.

Another technique to compute fault slip is to use a double couple point sources where body forces are imposed in a manner consistent with an effective plastic strain resulting from the slip. But the body forces depend on the elastic modulii which change across the fault surface. But in domain decomposition approach, Lagrange multipliers are equal and opposite across the fault which is a key difference. PyLith introduces Lagrange multipliers in order to calculate traction on the fault surface. When there is no relative displacement of the two sides of the fault due to a large friction value, the fault is locked and the Lagrange multipliers correspond to the forces required to keep the slip zero. When there is a slip along the fault surface Lagrange multipliers correspond to the forces consistent with the friction from the fault constitutive model. To model a fault in TOUGH2, hydraulic elements are added along the interface during the mesh making process. This facilitates calculating fluid pressure within the fault.

In PyLith, fault interfaces are introduced to determine the dislocations or jumps in the displacement field. These dislocations result from both tensile and shear slips across a fault surface. In 3D, these dislocations correspond to lateral-slip, reverse-slip, and fault opening (See Figure 2.9). Figure 2.9 shows an arbitrary orientation of a typical fault surface in 3D. δ, λ, and ϕ represent the angle of fault dip, the rake angle, and fault strike respectively. The figure also shows a slip vector $\boldsymbol{r}$ with respect to the fault surface and coordinate axes [Aagaard et al., 2014].

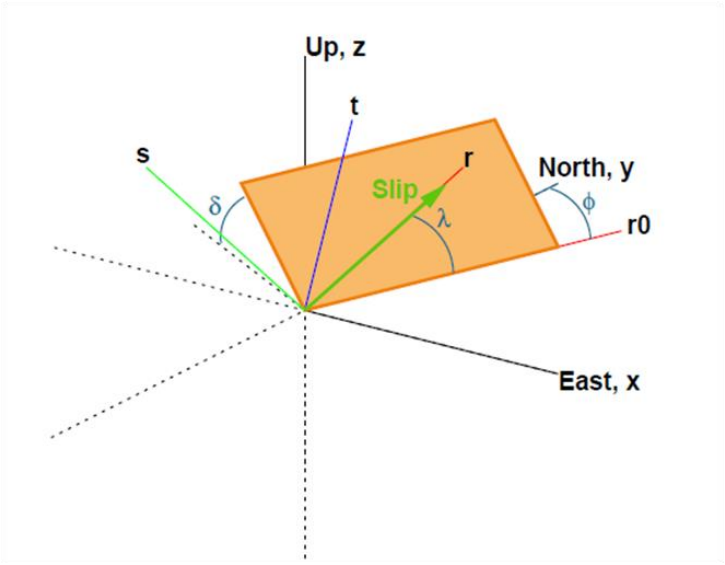

Figure 2.8 Orientation of a fault surface and its slip vector in 3D [Aagaard et al., 2014]

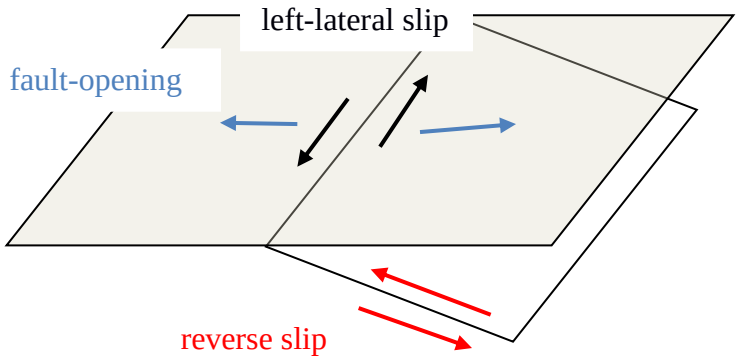

Figure 2.9 Sign conventions of different kinds of slips on a fault surface used in PyLith (shown in positive senses)

2.16 Fault Constitutive Models

A fault constitutive model is used to determine frictional stress of a fault which determines its strength to rupture. Mathematically, the frictional stress, τ_f can be expressed as:

$$\tau_f = \begin{cases} \tau_c - \mu_f \sigma_n^{'}, & \sigma_n^{'} < 0 \\ \tau_c, & \sigma_n^{'} \geq 0 \end{cases} \tag{2.74}$$

Where, τ_c is the cohesive strength of the fault, and $\mu_f$is the coefficient of friction. The friction coefficient is modeled differently in different fault constitutive models. It could be static model where $\mu_f$is assumed to be constant or not changing with fault slips.

2.16.1 Slip-weakening friction law

A slip-weakening model [Matsu'ura et al., 1992], unlike static friction law, considers μ_f as a function of slip magnitude $|\boldsymbol{d}|$. μ_f decreases from its static maximum value of μ_s to dynamic value μ_f over a critical slip distance d_c.

$$\mu_f = \begin{cases} \mu_s - (\mu_s - \mu_d)\dfrac{|\boldsymbol{d}|}{d_c}, & |\boldsymbol{d}| \leq 0 \\ \mu_d, & |\boldsymbol{d}| > 0 \end{cases} \tag{2.75}$$

This produces shear tractions on the fault surface equal to the cohesive stress plus a fault normal traction that varies with μ_f.

2.16.2 Rate- and state-dependent friction

In contrast to usual slip-dependent friction model, a rate- and state-dependent [RSF] friction model [Dieterich, 1979; Ruina, 1983; Tullis, 1988; Marone, 1998] provides a more complete representation of earthquake nucleation and rupture process due to the inclusion of an aging parameter, θ in it. Under an RSF constitutive relation, the coefficient of friction has the following form:

$$\mu = \mu_f + A\ \ln\left(\frac{V_2}{V_1}\right) + B\ \ln\left(\frac{\theta_1}{\theta_0}\right) \tag{2.76}$$

$$\frac{d\theta}{dt} = 1 - \frac{\theta V}{D_c} \tag{2.77}$$

Where a and b are dimensionless constants, V_0 is a reference slip speed, D_c is the characteristic slip distance over which θ evolves, and μ is friction coefficient at the reference slip speed and constant normal stress. The RSF model is based on laboratory experiments of frictional sliding on rock surfaces and fault gouges. The typical laboratory values of a and b are in the range 0.005 to 0.015. μ_f is the nominal coefficient of friction with typical values in the range 0.5-0.8. The state variable θ can be explained as the frictional contact time [Dieterich, 1979] or the average maturity of the contact asperities between the sliding surfaces [Rice, 1993]. At a constant normal stress and slip, θ takes a steady state value of $\theta^{SS} = \frac{D_c}{V}$. Equation (2.77) demonstrates that if the slip velocity V_1 increases, then there could be two possibilities. First, if $a - b < 0$ then the value of friction coefficient falls below its static value that is termed as slip-weakening, leading to dynamic slip on the fault. On the other hand, $if\ a - b > 0$ then fault strength increases and the elements under consideration can undergo only stable sliding. The two effects combined can capture a stick-slip behavior, which can describe the complete earthquake cycle more completely. tractions and resulting slip.

CHAPTER III

DEVELOPMENT OF A COUPLED HYDRO-GEOMECHANICAL CODE

3.1 Introduction

This chapter describes development of a coupled hydro-geomechanical code by combining the flow code TOUGH2 and geomechanics code PyLith. First, numerical formulation and solution procedure for each of the individual codes is discussed. Next, governing equations for coupled fluid flow and geomechanics are derived as a coupled simulator for sequential execution of the codes. In the subsequent section, solution strategy for stability and convergence is re-examined. Finally, development of the computational scheme for sequentially solving flow and geomechanics is explained.

3.2 Numerical Methods for Fluid Flow in TOUGH2

3.2.1 Governing equations

TOUGH2 solves a mass and an energy balance equations as follows:

$$\frac{d}{dt}\int_{V_n} M^{\kappa}\, dV_n = \int_{\Gamma_n} F^{\kappa}\cdot \mathbf{n} d\Gamma_n + \int_{V_n} q^{\kappa}\, dV_n \tag{3.1}$$

where we consider an arbitrary volume V_n for the integration domain of the flow system bounded by the closed surface Γ_n. The quantity M represents mass or energy per unit volume. Superscript κ refers to different components such as water, air, H_2, solutes etc. $\kappa = 1,2,\ldots,NK$ for mass

components and $\kappa = NK + 1$ for heat component. F represents mass or heat flux and q refers to the sink or source term. **n** is a unit normal vector on surface $d\Gamma_n$ which points inward into V_n.

Mass accumulation term is given by-

$$M^{\kappa} = \phi \sum_{\beta} S_{\beta}\, \rho_{\beta} X_{\beta}^{\kappa} \tag{3.2}$$

where, β represents fluid phases such as liquid, gas, non-aqueous phase liquid. For any component κ, the total mass is obtained by summing over β. ϕ is porosity, ρ_{β} is the density of phase β, and X_{β}^{κ} is the mass fraction of component κ present in phase β.

Heat accumulation term is given by-

$$M^{NK+1} = (1-\phi)\rho_R C_R T + \phi \sum_{\beta} S_{\beta}\, \rho_{\beta} u_{\beta} \tag{3.3}$$

where ρ_R and C_R are, respectively, grain density and specific heat of the rock, T is temperature, and u_{β} is specific internal energy in phase β.

Individual phase fluxes are given by a multiphase version of Darcy's law:

$$F_{\beta} = \rho_{\beta} u_{\beta} = -k \frac{k_{r\beta}\rho_{\beta}}{\mu_{\beta}\left(\nabla P_{\beta} - \rho_{\beta} g\right)} \tag{3.4}$$

Here μ_{β} is the Darcy velocity (volume flux) in phase β, k is absolute permeability, $k_{r\beta}$ is relative permeability to phase β, μ_{β} is viscosity, and

$$P_{\beta} = P + P_{c\beta} \tag{3.5}$$

is the fluid pressure in phase β, which is the sum of the pressure P of a reference phase (usually taken to be the gas phase), and the capillary pressure $P_{c\beta}$ (≤ 0). g is the vector of gravitational acceleration.

By applying Gauss's divergence theorem, equation (3.1) can be rewritten as:

$$\frac{\partial M^{\kappa}}{\partial t} = -div\mathbf{F}^{\kappa} + q^{\kappa} \tag{3.6}$$

which is a starting point numerical computation by using either finite element or finite difference method.

3.2.2 Discretization and finite difference formulation

TOUGH2 uses an integral finite difference method (IFD) [Edwards, 1972; Narasimhan and Witherspoon, 1976]. This means the discretization of the governing equation is done on the integrals without going through partial differential equations (PDEs) [Pruess, 2003]. In this approach [see Figure 3.1], a flow system can be viewed as a network of boxes that exchange mass and energy. It also allows for an application of boundary conditions on a very simple conceptual basis. Unlike conventional finite difference approaches, an IFD has many advantages: All geometric information like volume, area, and distances are defined locally. There is no need for local to global transformation of coordinates. This is especially more useful in case of spatially irregular features. This also allows for the advanced discretization approaches for fractured and highly heterogeneous media such double-porosity [Barenblatt et al., 1960], multiple interacting continua [Pruess and Narasimhan, 1985] and multi-region models [Gwo et al., 1996].

TOUGH2 uses an integral finite difference method in order to discretize the continuum mass and energy balance equations. Introducing appropriate averaging terms, we get:

$$\int_{V_n} M\, dV = V_n M_n \tag{3.7}$$

where M is a volume-normalized extensive quantity, and M_n is the average value of M over V_n. The space discretization is illustrated below:

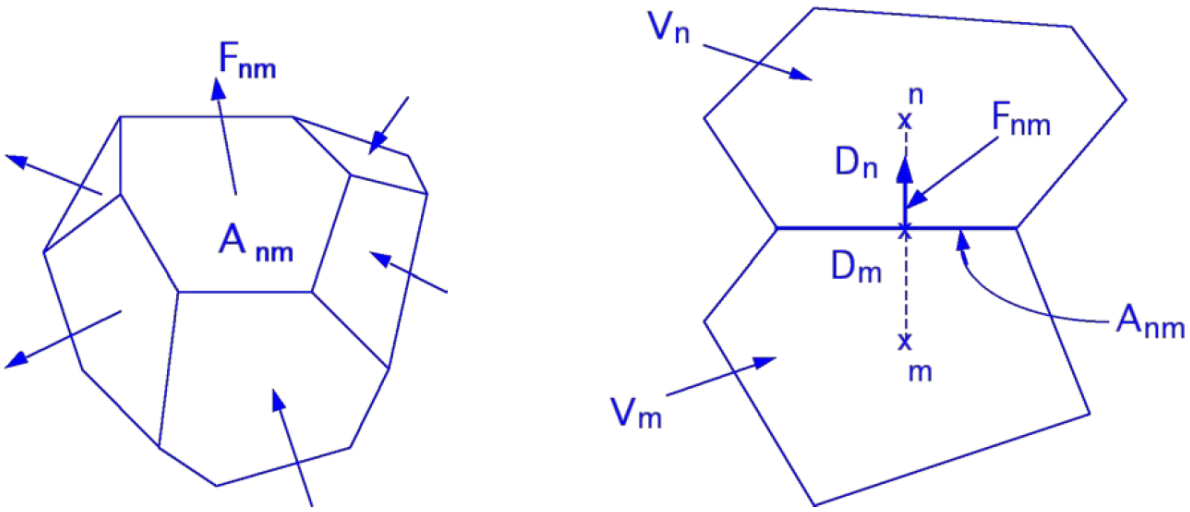

Figure 3.1 Illustration of flow calculation under an integral finite difference method

Surface integrals are approximated as a discrete sum of averages over surface segments Anm:

$$\int_{\Gamma_n} F^{\kappa} \cdot \mathbf{n} d\Gamma_n = \sum_m A_{nm} F_{nm} \tag{3.8}$$

Here F_{nm} is the average value of the (inward) normal component of F over the surface segment A_{nm} between volume elements V_n and V_m.

Substituting the discretized mass and heat flux terms into the governing equation (3.1) we get:

$$\frac{dM^{\kappa}}{dt} = \frac{1}{V_n} \sum_m A_{nm} F_{nm}^{\kappa} + q_n^{\kappa} \tag{3.9}$$

3.2.3 Solution procedure

TOUGH2 uses a fully implicit time discretization scheme in order to perform numerical computation of flux terms and its stability. After employing time level $t^{k+1} = t^k + \Delta t$ it results in

$$R_n^{\kappa,k+1} = M_n^{\kappa,k+1} - M_n^{\kappa,k} - \frac{\Delta t}{V_n}\left\{\sum_m A_{nm}\, F_{nm}^{\kappa,k+1} + V_n q_n^{\kappa,k+1}\right\} = 0 \tag{3.10}$$

where $R_n^{\kappa,k+1}$ is the residual term of flux difference between time step $t^{k+1}$and t^k. For each grid block V_n, there are a total of $\kappa = 1,2 \ldots, NEQ$ equations for respective components where $NEQ = NK + 1$. Therefore, for a problem domain having NEL grid blocks or elements there will be a total of $NEL * NEQ$ coupled nonlinear equations. These equations are solved by Newton-Raphson method.

3.3 Numerical Methods for Geomechanics in PyLith

3.3.1 Governing equations

In order to develop a numerical model for fault slip, the conventional finite element method for elasticity is augmented for domain decomposition approach [Aagaard et al., 2013]. The strong form of the elasticity equation is:

$$\rho \frac{\delta^2 \boldsymbol{u}}{\delta t^2} - \boldsymbol{f} - \boldsymbol{\nabla} \cdot \boldsymbol{\sigma} = \mathbf{0}\ in\ V \tag{3.11}$$

$$\boldsymbol{\sigma} \cdot \boldsymbol{n} = \boldsymbol{T}\ on\ S_T \tag{3.12}$$

$$\boldsymbol{u} = \boldsymbol{u}_0\ on\ S_u \tag{3.13}$$

$$(\boldsymbol{u}_+ - \boldsymbol{u}\_) - \boldsymbol{d} = 0\ on\ S_f \tag{3.14}$$

where u is the displacement vector on surface S_u, f is the body force vector, T is the traction on surface S_T, d is the slip vector on surface S_f, ρ is the density, and t is the time.

It is possible to have an overlapping domain for both displacement and traction vectors where both Dirichlet and Neumann boundary conditions cannot be applied simultaneously.
A weak form of the governing equation is formed by taking the dot product of the above equation with a weighting function and setting the integral equal to zero.

$$\int_V \boldsymbol{\phi} \cdot \left(\boldsymbol{\nabla} \cdot \boldsymbol{\sigma} + \boldsymbol{f} - \rho \frac{\delta^2 \boldsymbol{u}}{\delta t^2} \right) dV = 0 \tag{3.15}$$

Applying divergence theorem, inserting essential and natural boundary conditions, and exploiting the symmetry of the stress tensors, the weak form of the equation becomes:

$$-\int_V \nabla \boldsymbol{\phi} : \boldsymbol{\sigma} \, dV + \int_{S_T} \boldsymbol{\phi} \cdot \boldsymbol{T} \, dS + \int_V \boldsymbol{\phi} \cdot \boldsymbol{f} \, dV - \int_V \boldsymbol{\phi} \cdot \rho \frac{\delta^2 \boldsymbol{u}}{\delta t^2} \, dV = 0 \tag{3.16}$$

where $\boldsymbol{\nabla \phi} : \boldsymbol{\sigma}$ is the double inner product of the gradient of the weighting function and the stress tensor.

After adding the contributions of the Lagrange multipliers over the fault surface, the equation becomes:

$$\begin{aligned} -\int_V \nabla \boldsymbol{\phi} : \boldsymbol{\sigma} \, dV + \int_{S_T} \boldsymbol{\phi} \cdot \boldsymbol{T} \, dS - \int_{S_{f+}} \boldsymbol{\phi} \cdot \boldsymbol{l} \, dS + \int_{S_{f-}} \boldsymbol{\phi} \cdot \boldsymbol{l} \, dS + \int_V \boldsymbol{\phi} \cdot \boldsymbol{f} \, dV \\ - \int_V \boldsymbol{\phi} \cdot \rho \frac{\delta^2 \boldsymbol{u}}{\delta t^2} \, dV = 0 \end{aligned} \tag{3.17}$$

Similarly, we can write the weak form for the fault slip vector:

$$\int_{S_f} \boldsymbol{\phi} \cdot (\boldsymbol{d} - \boldsymbol{u}_+ + \boldsymbol{u}_-) \, dS = 0 \tag{3.18}$$

3.3.2 Discretization and finite element formulation

The mechanics code PyLith is discretized using nodal based finite element method [Hughes, 1987; Zienkiewicz and Taylor, 2005]. In the flow problem under IFD, pressure degrees of freedom are located at the center of a grid block whereas in the mechanics problem displacement degrees of freedom are located at the nodal points. In order to maintain conformity

and avoid interpolation, stress outputs are requested at the center of each cell by using 'Cell Filtered Average' scheme. This scheme computes the weighted average of the values within a cell [Aagaard et al., 2014]. The weights are determined from the quadrature associated with the cells.

Fault discretization in the mechanics problem needs special consideration. A number of nodes are defined as a 'nodeset' in order to represent a fault surface. For each node on the fault surface, a total of three nodes are created of which two side nodes correspond to positive side, and negative side of the fault. The third node is a Lagrange node and located in the middle. The side nodes store positive and negative displacements whereas the Lagrange node stores Lagrange multiplier and the fault slip vector. A fault coordinate system is defined to describe the commonly used fault motion parameters [normal or reverse, left or right lateral slip].

Expressing the weighting function $\boldsymbol{\phi}$, trial solution $\boldsymbol{u}$, Lagrange multipliers $\boldsymbol{l}$, and fault slip $\boldsymbol{d}$ as linear combinations of basis functions:

$$\boldsymbol{\phi} = \sum_{\boldsymbol{m}} \boldsymbol{a_m} N_m \tag{3.19}$$

$$\boldsymbol{u} = \sum_{\boldsymbol{n}} \boldsymbol{u}_n N_n \tag{3.20}$$

$$\boldsymbol{l} = \sum_{\boldsymbol{m}} \boldsymbol{l_p} N_p \tag{3.21}$$

$$\boldsymbol{d} = \sum_{\boldsymbol{m}} \boldsymbol{d_p} N_p \tag{3.22}$$

where Lagrange multipliers $\boldsymbol{l}$ and slip vectors $\boldsymbol{d}$ are associated with the fault surface meaning one less dimension than the displacement $\boldsymbol{u}$ and weighting function $\boldsymbol{\phi}$ which involve volume. Hence, $p < n$. Also, $n > m$.

Expressing the above expressions in matrix form:

$$\boldsymbol{\phi} = \boldsymbol{N_m} \cdot \boldsymbol{a_m} \tag{3.23}$$

$$\boldsymbol{u} = \boldsymbol{N_n} \cdot \boldsymbol{u}_n \tag{3.24}$$

$$\boldsymbol{l} = \boldsymbol{N_p} \cdot \boldsymbol{l_p} \tag{3.25}$$

$$\boldsymbol{d} = \boldsymbol{N_p} \cdot \boldsymbol{d_p} \tag{3.26}$$

Using the above matrix expressions in equations (3.17) and (3.18), we get:

$$\begin{aligned} -\int_V \nabla \boldsymbol{N_m^T} : \boldsymbol{\sigma}\, dV + \int_{S_T} \boldsymbol{N_m^T} \cdot \boldsymbol{T}\, dS - \int_{S_{f+}} \boldsymbol{N_m^T} \cdot \boldsymbol{N}_p \cdot \boldsymbol{l}\, dS + \int_{S_{f-}} \boldsymbol{N_m^T} \cdot \boldsymbol{N}_p \cdot \boldsymbol{l}\, dS \\ + \int_V \boldsymbol{N_m^T} \cdot \boldsymbol{f}\, dV - \int_V \rho \boldsymbol{N_m^T} \cdot \boldsymbol{N}_p \cdot \frac{\delta^2 \boldsymbol{u_n}}{\delta t^2}\, dV = 0 \end{aligned} \tag{3.27}$$

Similarly, we can write the weak form for the fault slip vector:

$$\int_{S_f} \boldsymbol{N_p^T} \cdot \left(\boldsymbol{N_p} \cdot \boldsymbol{d_p} - \boldsymbol{N_{n+}} \cdot \boldsymbol{u}_{n+} + \boldsymbol{N_{n-}} \cdot \boldsymbol{u}_{n-} \right) dS = 0 \tag{3.28}$$

3.3.3 Solution strategies for fault slip

Introducing time discretization Eqs. (3.27) and (3.28) can be written in the residual forms:

$$\begin{aligned} \boldsymbol{R_{u,a}^{n+1}} = -\int_V \nabla \boldsymbol{N_m^T} : \boldsymbol{\sigma}\, dV + \int_{S_T} \boldsymbol{N_m^T} \cdot \boldsymbol{T}\, dS \\ - \int_{S_{f+}} \boldsymbol{N_m^T} \cdot \boldsymbol{N}_p \cdot \boldsymbol{l}\, dS + \int_{S_{f-}} \boldsymbol{N_m^T} \cdot \boldsymbol{N}_p \cdot \boldsymbol{l}\, dS + \int_V \boldsymbol{N_m^T} \cdot \boldsymbol{f}\, dV \\ - \int_V \rho \boldsymbol{N_m^T} \cdot \boldsymbol{N}_p \cdot \frac{\delta^2 \boldsymbol{u_n}}{\delta t^2}\, dV \end{aligned} \tag{3.29}$$

$$\boldsymbol{R}_{l,a'}^{n+1} = \int_{S_f} \boldsymbol{N}_{\boldsymbol{p}}^{\boldsymbol{T}} \cdot \left(\boldsymbol{N}_{\boldsymbol{p}} \cdot \boldsymbol{d}_{\boldsymbol{p}} - \boldsymbol{N}_{\boldsymbol{n+}} \cdot \boldsymbol{u}_{n+} + \boldsymbol{N}_{\boldsymbol{n-}} \cdot \boldsymbol{u}_{n-}\right) dS \tag{3.30}$$

where $\boldsymbol{a}$ and $\boldsymbol{a}'$ correspond to the nodes for calculation of displacement $(\boldsymbol{u})$and Lagrange multipliers $(\boldsymbol{l})$, $\boldsymbol{R}_{u,a}^{n+1}$ *and* $\boldsymbol{R}_{l,a'}^{n+1}$ are the residuals calculated at time step $(n+1)$.

These equations are solved using the Portable, Extensible Toolkit for Scientific Computation (PETSc) [Balay et al., 1997] which can solve a system of linear equations with parallel processing. To evaluate the solution for the next time step, time is incremented and the equations are solved for that increment and finally the increment is added to the solution of the previous time step. The residual is in the form:

$$\boldsymbol{r} = \boldsymbol{b} - \boldsymbol{A} \cdot \boldsymbol{u} \tag{3.31}$$

where r is the residual and $\boldsymbol{A}$ is the Jacobian of the system and given by-

$$\boldsymbol{A} = \begin{pmatrix} \boldsymbol{K} & \boldsymbol{L}^T \\ \boldsymbol{L} & \boldsymbol{0} \end{pmatrix} \tag{3.32}$$

where *K* is associated with Eq. (3.29) and L is associated with the constraint Eq. (3.30).

The Jacobian of the system, *A*, is the opertion that is applied to the increment of the solution, $\boldsymbol{du}$, where

$$\boldsymbol{du}(t) = \boldsymbol{u}(t + \Delta t) - \boldsymbol{u}(t) \tag{3.33}$$

Since the action in the solution increment $(\boldsymbol{du})$ results from the stress increment, $\boldsymbol{d\sigma}$, we use:

$$\boldsymbol{\sigma}(t + \Delta t) = \boldsymbol{\sigma}(t) + \boldsymbol{d\sigma}(\boldsymbol{t})$$

to determine $\boldsymbol{K}$. Using linear elasticity and assuming infinitesimal strains we can write:

$$\boldsymbol{d\sigma}(\boldsymbol{t}) = \frac{1}{2} C[t] \cdot (\nabla + \nabla^T)\boldsymbol{u}[t] \tag{3.34}$$

where C is the fourth order tensor or elastic constants. It is constant for linear bulk constitutive models. For linear elasticity in 3D:

$$C = \frac{E}{(1+\upsilon)[1-2\upsilon]}\begin{bmatrix} 1-\upsilon & \upsilon & \upsilon & 0 & 0 & 0 \\ \upsilon & 1-\upsilon & \upsilon & 0 & 0 & 0 \\ \upsilon & \upsilon & 1-\upsilon & 0 & 0 & 0 \\ 0 & 0 & 0 & \frac{1}{2}[1-2\upsilon] & 0 & 0 \\ 0 & 0 & 0 & \frac{1}{2}[1-2\upsilon] & 0 & 0 \\ 0 & 0 & 0 & 0 & 0 & \frac{1}{2}[1-2\upsilon] \end{bmatrix} \tag{3.35}$$

where E is the Young's modulus and υ is the Poisson ratio.

Using the stress increment into the first term of Eq. (3.29) we get $\boldsymbol{K}$:

$$K = \int_V (\nabla + \nabla^T)\boldsymbol{N_m^T} \cdot \boldsymbol{C} \cdot (\nabla + \nabla^T)\boldsymbol{N_n}\ dV \tag{3.36}$$

The above portion of the Jacobian is analogous to the tangent stiffness matrix in conventional solid mechanics finite element formulations. Similarly, the portion of the Jacobian associated with the constraints Eq. (3.30) is:

$$L = \int_{S_f} \boldsymbol{N_p^T} \cdot (\boldsymbol{N_{n+}} + \boldsymbol{N_{n-}})\ dS \tag{3.37}$$

The terms $\boldsymbol{N_{n+}}$ and $\boldsymbol{N_{n-}}$ are identical and refer to degrees of freedom on positive and negative sides of the fault respectively. It is given by-

$$L_P = \int_{S_f} \boldsymbol{N_p^T} \cdot \boldsymbol{N_{n+}}\ dS \tag{3.38}$$

Eqs. (3.29) and (3.30) are solved using Newton's method with sufficient iteration (k) for convergence. With an approximation of the solution at time , an improved solution is obtained. Let the solution to the mechanics problem at time t_{n+1} be $[U^{n+1}, L^{n+1}]^{(k)}$for a Newton iteration number of k. Then an improved solution with one more iteration, $(k+1)$ is obtained as:

$$[U^{n+1}, L^{n+1}]^{(k+1)} = [U^{n+1}, L^{n+1}]^{(k)} + [\delta U^{n+1}, \delta L^{n+1}]^{(k)} \tag{3.39}$$

where the correction vector is the solution of the system of linear algebraic equations.

$$\begin{bmatrix} \boldsymbol{K} & \boldsymbol{C^T} \\ \boldsymbol{C} & \boldsymbol{0} \end{bmatrix}^{[k]} \begin{bmatrix} \boldsymbol{\delta U} \\ \boldsymbol{\delta L} \end{bmatrix}^{k} = -\begin{bmatrix} \boldsymbol{R_u} \\ \boldsymbol{R_l} \end{bmatrix}^{k} \tag{3.40}$$

The Jacobian [Aagaard et al., 2013] for the entire system is given by-

$$A = \begin{pmatrix} \boldsymbol{K_{nn}} & \boldsymbol{K_{nn+}} & \boldsymbol{K_{nn-}} & \boldsymbol{0} \\ \boldsymbol{K_{n+n}} & \boldsymbol{K_{n+n+}} & \boldsymbol{0} & \boldsymbol{L_p^T} \\ \boldsymbol{K_{n-n}} & \boldsymbol{0} & \boldsymbol{K_{n-n-}} & \boldsymbol{-L_p^T} \\ \boldsymbol{0} & \boldsymbol{L_P} & \boldsymbol{-L_P} & \boldsymbol{0} \end{pmatrix} \tag{3.41}$$

where n refers to the DOF not associated with the fault, n_+ refers to DOF associated with the positive side of the fault, n_- refers to the DOF associated with the negative side.

3.4 Numerical Formulation of Coupled Fluid Flow and Geomechanics

Analytical solution for coupled flow and geomechanics is cumbersome. Therefore, numerical formulations are adopted in order to make the solution computationally efficient and feasible. Two separate numerical formulations are adopted for two different sub-problems – flow problem and mechanics problem. Each sub problem is based on space and time discretization, formation of a system of algebraic equations, and solution of the coupled equations using an efficient scheme.

Usually for a coupled hydro-geomechanical problem a cell-centered finite volume approach [Aziz and Settari, 1979] is adopted for the fluid flow simulation whereas a finite volume approach is used for the mechanics problem [e.g. Zienkiewicz et al., 1988; Armero and Simo, 1992]. In a finite volume approach flow parameter such as pressure is output at the center of each cell of the flow grid. On the other hand, a nodal-based finite element method outputs the stress and strain fields at the corner nodes of each cell of the geomechanics grid. The space

discretization requires local mass conservation at the element level, continuous displacement field, and convergent approximations with the lowest order discretization [Jha and Juanes, 2007].

Let the continuum domain V be partitioned into non-overlapping elements or grid blocks such that $V = \sum_{j=1}^{n_{elem}} V_j, \ \ where \ n_{elem}$ is the number of elements. We define the functional spaces for the solution of pressure $\boldsymbol{p}$ as $\mathcal{Q} \subset L^2(V)$ and for displacement $\boldsymbol{u}$ as $\mathcal{U} \subset \left(H^1(V)\right)^d$ where $d = 2,3$ is the number of space dimensions. Let also φ and $\boldsymbol{\eta}$ are the test functions for flow and mechanics problems respectively. $\mathcal{Q}_h, \mathcal{Q}_{h,0}, \mathcal{U}_h, and \ \mathcal{U}_{h,0}$ are the corresponding finite-dimensional subspaces. Then the functional space for solutions of both flow and mechanics problem will be such that $(u_h, p_h) \in \mathcal{U}_h \, x \, \mathcal{Q}_h$. The discrete approximations of the governing equations (2.19) and (2.21) become:

$$\int_V \nabla \eta_h : \sigma_h \, dV = \int_V \eta_h \cdot \rho_b g \, dV + \int_V \eta_h \cdot \bar{t} \, dV \, dS, \qquad \eta_h \in \eta_h \tag{3.42}$$

$$\frac{1}{\rho_{f,0}} \int_V \varphi_h \frac{\partial m_h}{\partial t} dV + \int_V \varphi_h \nabla \cdot v_h dV = \int_V \varphi_h \, f dV, \qquad \forall \varphi_h \in \mathcal{Q}_{h,0} \tag{3.43}$$

Let pressure field p_h and the displacement field u_h can be approximated as:

$$p_h = \sum_{j=1}^{n_{elem}} \varphi_j \, \boldsymbol{P}_j \tag{3.44}$$

$$\boldsymbol{u}_h = \sum_{b=1}^{n_{node}} \eta_b \, U_b \tag{3.45}$$

where n_{elem} is number of elements, P_j are the element pressures, n_{node} is the number of nodes, and U_b are the displacement vectors at the element nodes. Pressure shape functions are assumed to be piecewise constant functions so that φ_j takes a constant value of *1* over element *j* and *0* at

all other elements. Applying divergence theorem, we can write:

$$\int_V \varphi_i \, Div\, \boldsymbol{v} \; dV = -\int_{dV} \boldsymbol{v}.\boldsymbol{n_i}\, dS = -\sum_{j=1}^{n_{face}} \boldsymbol{v}.\boldsymbol{n_i}\, dS = -\sum_{j=1}^{n_{face}} V_{\boldsymbol{ij}} \tag{3.46}$$

We arrive at the semi-discrete finite difference equations:

$$\int_{V_i} \left(\frac{1}{M}\right)\frac{\partial P_i}{\partial t}\, dV + \int_{V_i} b\,\frac{\partial \varepsilon_v}{\partial t}\, dV - \sum_{j=1}^{n_{face}} V_{\boldsymbol{ij}} = \int_V f\, dV \tag{3.47}$$

The displacement interpolation function η_b is approximated such that it takes a value of *1* at the node b and *0* everywhere else. Inserting this interpolation function in the stress equilibrium Eq. (2.19) we get:

$$\int_V \boldsymbol{B}_a^T \sigma_h \, dV = \int_V \eta_a \cdot \rho_b g \, dV + \int_S \eta_a \cdot \bar{t}\, dV \, dS \tag{3.48}$$

where $\boldsymbol{B}_a^T$ is linearized strain matrix operator which in 2D is given by-

$$\boldsymbol{B}_a = \begin{bmatrix} \partial_x \eta_a & 0 \\ 0 & \partial_y \eta_a \\ \partial_y \eta_a & \partial_x \eta_a \end{bmatrix} \tag{3.49}$$

The stress and strain tensors are given by-

$$\sigma_h = \begin{bmatrix} \sigma_{h,xx} \\ \sigma_{h,yy} \\ \sigma_{h,xy} \end{bmatrix} \tag{3.50}$$

$$\varepsilon_h = \begin{bmatrix} \varepsilon_{h,xx} \\ \varepsilon_{h,yy} \\ \varepsilon_{h,xy} \end{bmatrix} \tag{3.51}$$

where the poroelastic stress and strains are defined as follows:

$$\partial \boldsymbol{\sigma} = \partial \boldsymbol{\sigma}' - b\delta p_h \mathbf{1} \tag{3.52}$$

$$\partial \boldsymbol{\sigma}' = \boldsymbol{C} : \delta \varepsilon_h \tag{3.53}$$

where $\boldsymbol{\sigma}'$ is the effective stress tensor, and $\boldsymbol{C}$ is the elasticity matrix given in 2D:

$$C = \frac{E(1-\upsilon)}{(1+\upsilon)(1-2\upsilon)} \begin{bmatrix} 1 & \frac{\upsilon}{(1-\upsilon)} & \frac{\upsilon}{(1-\upsilon)} \\ \frac{\upsilon}{(1-\upsilon)} & 1 & \frac{\upsilon}{(1-\upsilon)} \\ \frac{\upsilon}{(1-\upsilon)} & \frac{\upsilon}{(1-\upsilon)} & 1 \end{bmatrix} \tag{3.54}$$

where, E is Young's modulus, and υ is Poisson's ratio.

3.5 Coupled Solution Strategy

Five different solution strategies have been investigated for stability, accuracy, and efficiency in a typical coupled fluid flow and reservoir geomechanics problem [Kim et al., 2009]: fully coupled, drained, undrained, fixed-strain, and fixed-stress (Figure 3.2). The solution of a fully coupled approach requires solving both the flow and mechanics codes simultaneously.

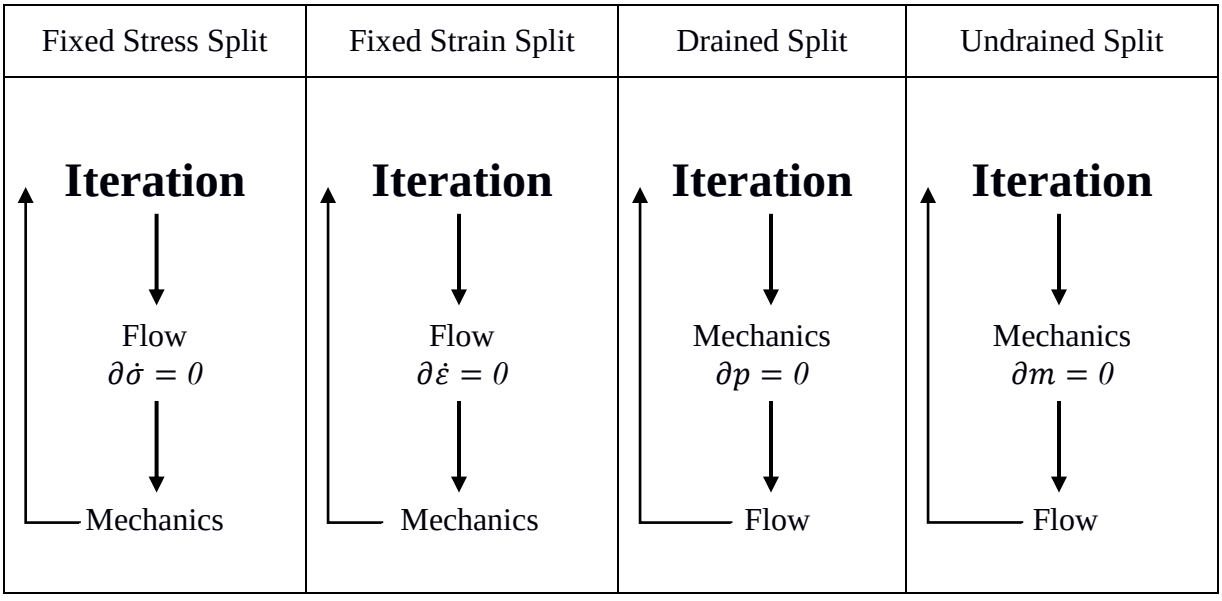

Figure 3.2 Solution strategies for sequentially coupled flow and geomechanics problem

It is evident from the Figure 3.2 that in both drained and undrained split methods mechanics

problem is solved first and then the fluid flow problem after. Whereas in fixed-strain and fixed-stress split methods, flow problem is solved first and mechanics problems is solved in the second stage. All these solution strategies are applicable to both linear and nonlinear problems including elastic and elastoplastic nonlinearity.

A coupled hydro-geomechanical problem involves a stress equilibrium Eq. (2.19) and fluid mass balance Eq. (2.21). Denoting by the □ operator of the coupled original problem the discrete approximation of the fully coupled method can be expressed as:

$$\begin{bmatrix} \boldsymbol{u}^n \\ \boldsymbol{p}^n \end{bmatrix} \overset{\mathcal{A}_{fc}}{\Longrightarrow} \begin{bmatrix} \boldsymbol{u}^{n+1} \\ \boldsymbol{p}^{n+1} \end{bmatrix} \tag{3.55}$$

$$\text{where} \quad \mathcal{A}_{fc}: \begin{cases} Div\, \boldsymbol{\sigma} = 0 \\ \dot{\boldsymbol{m}} + Div\, \boldsymbol{v} = 0 \end{cases}$$

where $(\dot{})$ denotes time derivative. Using a backward Euler time discretization the residual forms of the fully discrete coupled equations are:

$$\boldsymbol{R}_i^p = \int_{V_i} \frac{1}{M}\left(P_i^{n+1} - P_i^n\right) dV + \int_{V_i} b(\varepsilon_v^{n+1} - \varepsilon_v^n) dV - \Delta t \sum_{j=1}^{n_{face}} V_{h,ij}{}^{\boldsymbol{n+1}} - \Delta t \int_V f^{n+1}\, dV \qquad \forall i = 1,2,3, \ldots\ldots, n_{elem} \tag{3.56}$$

$$\boldsymbol{R}_a^u = \int_V \boldsymbol{B}_a^T \sigma_h{}^{n+1}\, dV - \int_V \eta_a \cdot \rho_b{}^{n+1} \boldsymbol{g}\, dV - \int_S \eta_a \cdot \bar{t}^{n+1}\, dV\, dS \qquad \forall a = 1,2, \ldots\ldots, n_{node} \tag{3.57}$$

Equations (3.56) and (3.57) represent both spatial and time discretized forms of the governing equations of coupled fluid flow and mechanics, where, $\boldsymbol{R}_i^p$ and $\boldsymbol{R}_a^u$ are the residuals for flow (element *i*) and mechanics (node *a*), respectively. Given an approximation of the solution $\left[u^{(n+1),k}, p^{(n+1),k}\right]$ at time level $(n+1)$ and an iteration level k, an improved solution for an

iteration level of $(k+1)$, is given by the Newton's method:

$$\begin{bmatrix} \boldsymbol{K} & -\boldsymbol{L}^T \\ \boldsymbol{L} & \boldsymbol{F} \end{bmatrix} \begin{bmatrix} \partial \boldsymbol{u} \\ \partial \boldsymbol{p} \end{bmatrix}^{n+1,(k+1)} = - \begin{bmatrix} \boldsymbol{R}^u \\ \boldsymbol{R}^p \end{bmatrix}^{n+1,(k+1)} \tag{3.58}$$

where Jacobian matrix, J is given by-

$$\boldsymbol{J} = \begin{bmatrix} \boldsymbol{K} & -\boldsymbol{L}^T \\ \boldsymbol{L} & \boldsymbol{F} \end{bmatrix} \tag{3.59}$$

$\boldsymbol{K}$ is the stiffness matrix, $\boldsymbol{L}$ is the coupling poromechanics matrix, and $\boldsymbol{F}$ is the flow matrix given by-

$$\boldsymbol{F} = \boldsymbol{Q} + \Delta t \boldsymbol{T} \tag{3.60}$$

where $\boldsymbol{Q}$ is the compressibility matrix, and $\boldsymbol{T}$ is the transmissibility matrix. The matrices are defined as follows:

$$\boldsymbol{K_{ab}} = \int_V \boldsymbol{B}_a^T \boldsymbol{C}\, \boldsymbol{B_b}\, dV \tag{3.61}$$

$$\boldsymbol{L_b} = \int_V \varphi_i b (\boldsymbol{Grad}\, \eta_b)^T \; dV \tag{3.62}$$

$$\boldsymbol{Q_{i,j}} = \int_V \varphi_i M^{-1} \varphi_j \, dV \tag{3.63}$$

where T_{ij} is the transmissibility between grid blocks i and j. Under a fully coupled approach, the Jacobian J is computed at every time step to determine $\delta \boldsymbol{u}$ and $\delta \boldsymbol{p}$ until the residuals are reasonably zero and fall below the desired tolerance i.e. convergence.

3.5.1 Fixed-stress split method

In the developed coupled simulator fixed-stress split method is used for the operator splitting and numerical computation. Under this methodology, flow problem is solved first and

then the mechanics problem is solved. The total volumetric mean stress is kept fixed i.e. $\partial\dot{\sigma}_v = 0.\ \ or,\ \dot{\sigma}_v{}^{n+1/2} = \dot{\sigma}_v{}^{n}$. The volumetric stress term $\left(\frac{b}{K_{dr}}\right)\dot{\sigma}_v$ in the accumulation term of equation (2.34) is computed explicitly. The operator □ is decomposed based on the solution of flow and mechanics problems as follows:

$$\begin{bmatrix}\boldsymbol{u}^n\\ \boldsymbol{p}^n\end{bmatrix} \overset{\mathcal{A}_{ss}^{p}}{\Longrightarrow} \begin{bmatrix}\boldsymbol{u}^{n+1/2}\\ \boldsymbol{p}^{n+1}\end{bmatrix} \overset{\mathcal{A}_{ss}^{u}}{\Longrightarrow} \begin{bmatrix}\boldsymbol{u}^{n+1}\\ \boldsymbol{p}^{n+1}\end{bmatrix} \tag{3.64}$$

where, $\mathcal{A}_{ss}^{p} : \begin{cases}\dot{\boldsymbol{m}} + Div\,\boldsymbol{v} = 0\\ \partial\dot{\sigma}_v = 0\end{cases}$

$$\mathcal{A}_{ss}^{u} : \begin{cases} Div\,\boldsymbol{\sigma} = 0\\ \partial p = 0\ or, \quad Div\boldsymbol{\sigma}' = 0\end{cases}$$

Since we keep the rate of the entire stress tensor field constant during the solution of the flow problem, the following condition should be satisfied:

$$\begin{bmatrix}\boldsymbol{K} & -\boldsymbol{L}^T\\ \boldsymbol{L} & \boldsymbol{F}\end{bmatrix}\begin{bmatrix}\partial\boldsymbol{u}\\ \partial\boldsymbol{p}\end{bmatrix} = \begin{bmatrix}\boldsymbol{K} & -\boldsymbol{L}^T\\ \boldsymbol{0} & \boldsymbol{F}+\boldsymbol{L}\boldsymbol{K}^{-1}\boldsymbol{L}^T\end{bmatrix}\begin{bmatrix}\partial\boldsymbol{u}\\ \partial\boldsymbol{p}\end{bmatrix} - \begin{bmatrix}\boldsymbol{0} & \boldsymbol{0}\\ -\boldsymbol{L} & \boldsymbol{L}\boldsymbol{K}^{-1}\boldsymbol{L}^T\end{bmatrix}\begin{bmatrix}\partial\boldsymbol{u}\\ \partial\boldsymbol{p}\end{bmatrix} \tag{3.65}$$

Therefore, the flow problem is solved with $(\boldsymbol{F}+\boldsymbol{L}\boldsymbol{K}^{-1}\boldsymbol{L}^T)\partial\boldsymbol{p} = -\boldsymbol{R}^p$. Since the rate of volumetric mean stress is kept constant by introducing the term $\frac{b^2}{K_{dr}}$ locally in each element, there is no need of the full matrix inversion and multiplication $\boldsymbol{L}\boldsymbol{K}^{-1}\boldsymbol{L}^T$**.** In the second step, the mechanics problem is solved following $\boldsymbol{K}\partial\boldsymbol{u} = -\boldsymbol{R}^u\boldsymbol{L}^T\partial\boldsymbol{p}$**.**

3.6 Coupling Strategies

Coupled processes involve formulation of a multiphysics problem of different problem domains having varying time and length scales in order to solve them simultaneously. A fully coupled approach usually assumes (Jha, 2005):

- domains of individual processes be solved together
- partial differential equations that describe each of the individual processes have their dependent variables implicitly formulated

Other coupling strategies are briefly discussed below:

3.6.1 Fully coupled vs. sequentially coupled

for a typical multiphysics problem there are usually three approaches: fully coupled, loosely coupled, and one-way coupled [Minkoff et al., 2003]. In a fully coupled simulator, a single set of nonlinear coupled partial differential equations is derived and solved by incorporating all the relevant physics of flow and mechanics. In a loosely coupled approach, the governing equations for flow and mechanics are solved separately but sequentially. In that sense, a fully coupled approach might be more rigorous in simulating the complex multiphysics involved, but it is difficult and expensive. Unlike a fully coupled approach, where the full set of regular flow/mechanics time steps are used, in loose coupling, large jumps in time occur in the flow simulation due to the infrequent time steps dictated by the mechanics simulator. Also, in a fully coupled approach, a single computational grid is used for both of the codes whereas in a loosely coupled approach, the spatial grids can be different.

The advantage of using a loosely coupled algorithm is that it can capture much of the complexity of the underlying physics of a coupled problem at considerably less time and cost [Minkoff et al., 2003]. In a loosely coupled sequential algorithm, a high-level interface couples the two codes by calling each code sequentially and repeatedly. A time step, δt_1 [$\delta t_1 = t_1 - t_0$], for example, is specified to run the flow code first. The flow code usually breaks up that time step into number of smaller intervals in order to converge to its solution by the end of the given time

step. The pressure output from the flow code is then passed to the mechanics code, which runs a simulation for the same time interval, δt_1. To converge to its solution, the mechanics code may take one time step or a number of sub-steps that are generally different from those used in the flow calculation. The pore pressures are used as loads in the geomechanical governing equations in order to calculate effective stresses which are, in turn, used to calculate new porosity and permeability of the reservoir. The updated values of these flow parameters are then used in the flow code for the next time step. Thus a loosely coupled algorithm is staggered in time and involves a two-way sequential passage of information.

3.6.2 One-way coupled

Under a one-way coupling scheme, the flow problem and the mechanics problem are solved separately and independent of each other, but for the same time period. In this approach, output from one code is passed to the other code only in one direction. It could be, for example, passing pore water pressure from flow code to mechanics code but no passage of information from mechanics code to the flow code. An example of successful demonstration of one-way coupling is well failure prediction in Belridge Field, California [Fredrich et al., 1996]. Minkoff et al. [2003] argues that a one-way coupled approach is preferable to gain valuable insight of a physical problem and to the cases where mechanics is important than the fluid alone.

3.7 Development of the Computational Scheme

The development of the sequential coupled hydro-geomechanical computational framework is based on a sequential coupling algorithm [Settari and Mourits, 1994; Minkoff et al., 2003, Kim, 2009] and divided into two parts. The first part is focused on the modeling of

fluid and heat transport through porous and fractured strata under high injection pressure and calculation of changes in the fluid pressure field due to the injection. The second part deals with earthquake nucleation, i.e. triggering of shear slip on pre-existing highly stressed faults, due to the changes in the reservoir stress conditions resulting from fluid injection. In order to accomplish the first part, the LBNL-developed code TOUGH2 [Pruess et al., 1999] is used. TOUGH2 is a finite difference-based suite of codes that contain multi-dimensional numerical models for simulating the coupled transport of water, vapor, non-condensible gas, and heat in porous and fractured media.

For the second part, the geomechanics code PyLith is used. PyLith is an open-source finite-element code for dynamic and quasi-static simulation of earthquakes developed by the Computational Infrastructure for Geodynamics [CIG, 2014]. TOUGH2 and PyLith use different meshes, each created using different mesh generator. The reason behind this is that the two codes use different mesh formats in their respective calculations. TOUGH2 uses its own mesh-generation module called MESHMaker. PyLith can use geometry data either in the form of a manually produced ASCII format or the binary formats produced by CUBIT [CUBIT 14.1, 2014] and LaGriT [LaGriT, 2014]. In our present development, CUBIT is used in PyLith to create a 3D model of faults and fractures at the site of interest; i.e. site characterization, model conceptualization, and grid generation.

3.7.1 TOUGH2 execution

TOUGH2 has a modular architecture (See Figure A1, Appendix) where the flow and transport module can interface with different fluid property modules. The modular approach enables the code to handle multicomponent, multiphase fluid flow systems. The governing

equations solve the thermophysical properties such as density, viscosity, enthalpy, etc., by using an appropriate equation of state (EOS) module. One large array holds the primary variables such temperature, pressure, saturation, etc., for all the grid blocks and another large array contains all other thermophysical parameters in order to assemble the governing flow and transport equations. Fortran77 COMMON block arrays are used to hold the spatially distributed thermodynamic variables. The list of TOUGH2 subroutines [Pruess et al., 1999] and their functions are listed in the Table 3.1 below (See Table A1, Appendix):

Table 3.1 Various subroutines used in TOUGH2 for flow computation

Subroutines	**Functions**
TOUGH2 (main	Executive routine, define arrays depending on the size of a
INPUT, RFILE	Initialize a problem
CYCIT	Time stepping routine
EOS	Equations of state that define thermophysical properties and phase
MULTI	Mass and energy balance equations are assembled here block
QU	Defines sink and source terms
LINEQ	Executive routine for linear equation solver
CONVER	Shows converged time steps, updates thermodynamic variables and iteration counters
WRIFI, OUT, BALLA	Outputs results

TOUGH2 is initialized with all the thermophysical properties with time step counter KCYC, iteration counter ITER, and convergence flag KON. With increasing ITER values, the accumulation and flow terms are assembled in subroutine MULTI, which calls subroutine QU if there is sink or source terms. Subroutine MULTI computes residuals by Newton-Raphson

method and checks convergence. After convergence is achieved, primary variables are updated by the subroutine CONVER. In case of convergence failure, subroutine LINEQ is called for invocation of linear equation solvers. The value of KON decides whether the program will go to the next iteration or the next time step. If there is a failure in the computation of thermophysical parameters, or solving linear equations, or convergence, time step is being reduced by some predefined factor.

3.7.2 Time stepping in TOUGH2

Execution of TOUGH2 will terminate if the user-specified total number of time steps or a specified simulation time is reached. If the time step is too small or conditions are too close to steady state, flow convergence can be achieved without requiring the updates of thermodynamic variables. TOUGH2 decides on the steady state based on the convergence on the first iteration for 10 consecutive time steps. Under an automatic time step control, TOUGH2 stops executing if there is a convergence failure for two consecutive time steps. This is because under approaching steady state conditions, the rates of change in thermodynamic variables become small for which time step will become very large. This, in turn, increases the off-diagonal terms of the Jacobian matrix so large that convergence of the linear equation solver may not be achieved due to numerical roundoff [Pruess et al., 1999]. A situation may arise where a somewhat smaller time step converges the program without solving the linear equation whereas somewhat larger time step required for the linear equation solver does not guarantee the convergence. This is designed in order to prevent the program to go on that 'no progress' calculations and on for large number of user-specified time steps.

3.7.3 Execution of PyLith

A workflow of PyLith execution is shown in the Appendix (Figure A2) section. There three main inputs to run a problem with PyLith: mesh information, description of the relevant parameters, and databases defining the material properties and boundary conditions. PyLith is run from the command line in Windows, Mac, and Linux platform. We use Linux based Ubuntu platform both for PyLith and TOUGH2. PyLith writes solution in Visualization Toolkit (.vtk) text data format or Hierarchical Data Format (HDF5). We use VisIt [Childs et al., 2012] for visualization of the outputs throughout this document. VisIt is a open-source, interactive, scalable, distributed, parallel visualization and graphical analysis tool developed at the Lawrence Livermore National Laboratory. It was originally developed by the U.S. Department of Energy Advanced Simulation and Computing Initiative (ASCI) to visualize and analyze the results of terascale simulations. VisIt can read both .vtk and .h5 file formats and play multiple consecutive files like an animation movie. This enables us to see the evolution of stress field or slip along the fault with time in PyLith.

Figure 3.3 shows a flow chart for selection of time step based on the numerical procedure and convergence of the individual codes, TOUGH and PyLith. Time step selection for the geomechanics code governs the time step for the entire coupled simulator (TOUGH-PyLith). This is because geomechanics solver has more rigorous requirement of convergence for nonlinear friction solver of the fault surface [Aagaard et al., 2013]. Under this approach, a time step is selected based on a pre-run experience of the geomechanics simulator which has converged successfully. Next, that time step is used to run the flow problem in TOUGH2. If the flow code does not converge we select another suitable time step for the geomechanics and use it in the flow code until it converges. Usually, the flow code TOUGH2 converges for almost any

time step that is selected for the convergence of geomechanics code. This is because PyLith simulates earthquakes which involves hundreds or thousands of years.

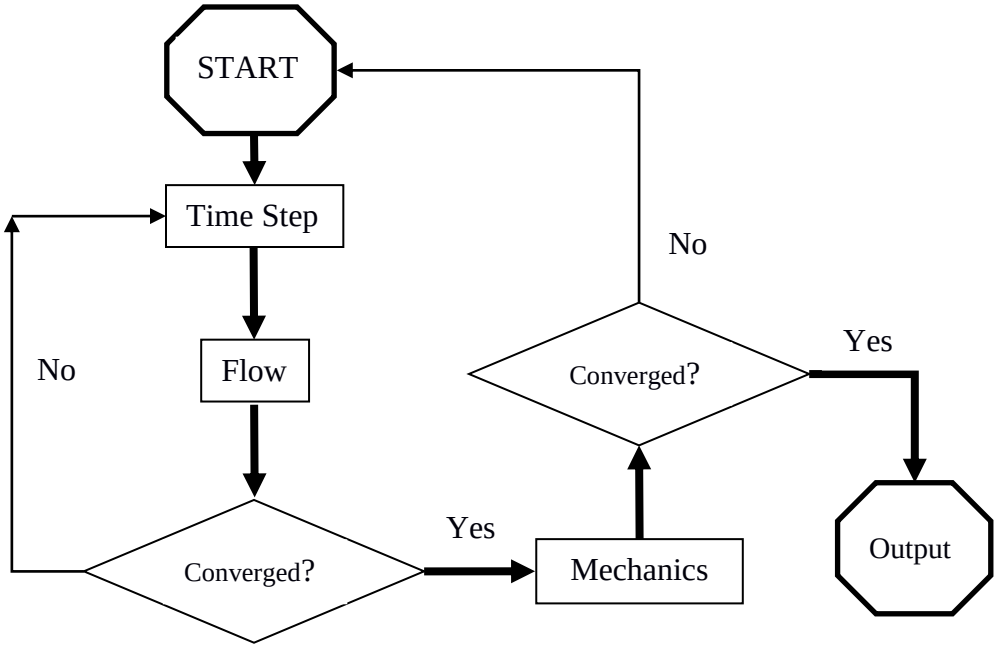

Figure 3.3 Flow chart showing selection of time step criteria for convergence of flow (TOUGH2) and geomechanics code (PyLith)

Therefore, the time steps are on the order of years which are good for converging the flow problem as well. For any given time step, if not converged, TOUGH2 multiplies that time step with pre-allocated factors in order to reduce that time step to a suitable value for convergence.

3.7.4 Time stepping in PyLith

PyLith has three types of time stepping formulation for time-dependent problem simulations. They are as follows:

User-Specified Uniform Time Step

Under a user-specified uniform time stepping scheme, the user specifies a certain amount of time to be used as a constant time step throughout the simulation. The user-specified time step has to be smaller than the stable time step computed by smallest finite element cells of the grid. Otherwise, PyLith gives an error.

User-Specified Nonuniform Time Step

A nonuniform user-specified time step scheme entails specification of time step changes via a text file. Stable time step is being checked like in the user-specified time stepping.

Automatic Nonuniform Time Step

Automatic nonuniform time steps automatically calculates a time step based on the material constitutive model and rate of deformation. The automatic stable time step calculation is based on the calculation of wave propagation throughout the each finite element cell by the constitutive models. The user has some sorts of control over this time step selection in terms of frequency with which a new time step is calculated, using time step relative to the one defined by the constitutive models, and a maximum value for a time step.

For the TOUGH-PyLith time stepping procedure, TOUGH is run for a user-specified time step which is usually governed by the geomechanics code since our end results are the outputs of stress field and slip. If TOUGH converges within that time step, that time step is transferred to PyLith to use as its total runtime (not time step). Since TOUGH converges for that time step and gives pressure field output corresponding to that time step, we want to make sure that PyLith runs for the same amount of time to get the stress field output and so that we are able to compute the effective stress field for that period of runtime. If TOUGH does not converge within that time step, it is being reduced within the time stepping formulation inside the integral

finite difference method until it converges. The reduced time step is then transferred to PyLith for its total runtime. Therefore, time stepping procedure used in the current TOUGH-PyLith coupling procedure is uniform user-specified. Although the user is not explicitly giving the time step to PyLith, time is not being automatically calculated under PyLith formulation either. It is using the time step that is transferred from the converged TOUGH time step.

3.7.5 Coupled computational procedure

Figure 3.4 shows a simplified representation of the four-step scheme used in our coupling.

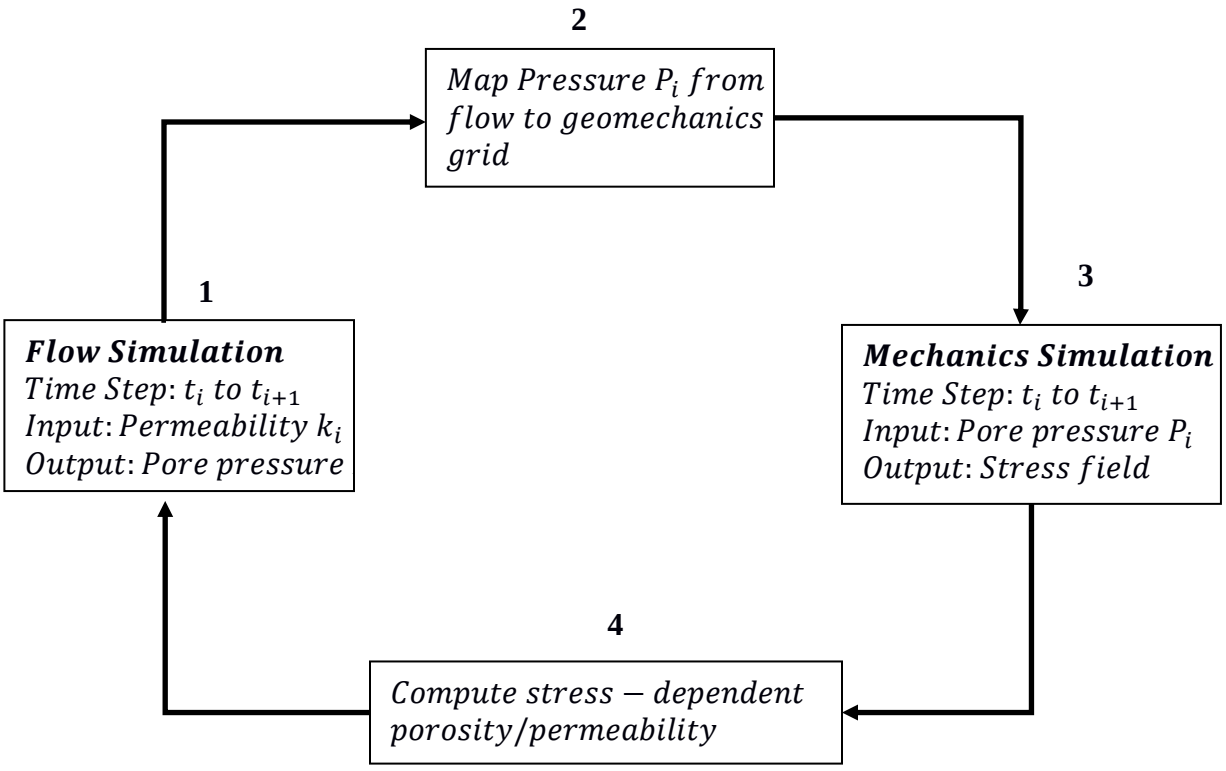

Figure 3.4 Coupling scheme between TOUGH2 and PyLith

In the first step of the cycle, we model the fluid transport through a porous rock volume by means of the flow simulator TOUGH2. In addition to pressure, TOUGH2 also provides outputs

of reservoir temperature, multiphase saturations, capillary pressure and other hydrogeological parameters. At the end of the flow simulation step, TOUGH2 provides us with the pore fluid pressure state in the reservoir system. The pore pressure is output at the centers of all of grid blocks in the computational domain. In second step, we map the pore pressure of each grid block from the flow grid to the geomechanics grid. In the third step, we run PyLith for the same time interval as for the TOUGH2 run. The newly calculated pore pressures are used in the calculation of effective stresses by modifying the governing equations implemented in PyLith. In the fourth step of the cycle, we use a FORTRAN interface to estimate the permeability of the fractured and faulted zones by using an effective stress-dependent permeability model. We obtain the permeability output at the center of the geomechanics grid and map it from the geomechanics grid to the TOUGH2 grid. The updated permeability is then used as input in the next cycle of TOUGH2 run.

CHAPTER IV

VERIFICATION AND VALIDATION OF THE COUPLED SIMULATOR

4.1 Introduction

This chapter describes verification and validation of the developed TOUGH-PyLith coupled simulator. To distinguish the two terms, verification demands if we are building the code right whereas validation requires if we are building the right code. Typically, code verification is performed before the code validation. To verify our code, we compare the results from our numerical simulator (TOUGH-PyLith) with the analytical solution of Terzaghi's classical uncoupled 1-d consolidation problem, which is a fluid diffusion problem. To validate the code, Mandel's problem of coupled poroelasticity is revisited to show the agreement between the analytical solution and the results obtained from the coupled simulator. Additionally, the code is benchmarked against available TOUGH-FLAC thermal-hydrological-chemical coupled simulator to show how they calibrate against each other.

4.2 Terzaghi's One Dimensional Consolidation

Soil consolidation is a coupled poroelasticity problem [Terzaghi, 1996; Biot, 1941; Cheng et al., 1993; Voyiadjis and Song, 2006; Verruijt, 2013] for which Terzaghi provided a simplified solution by means of a 1-D fluid diffusion equation and treating as an uncoupled problem. Although Terzaghi's simplified solution could not demonstrate the coupled poroelasticity, we use it to check the validity of fluid to solid coupling capability of TOUGH-

PyLith coupled simulator. In other words, if the results from TOUGH-PyLith agrees with the solution given by Terzaghi's equation we could confidently say that our code is built accurately.

In a classical Terzaghi's 1-D consolidation problem, a saturated soil sample is confined on all sides except the top surface. The sample is kept saturated throughout the entire experiment by submerging it into a water-filled container.

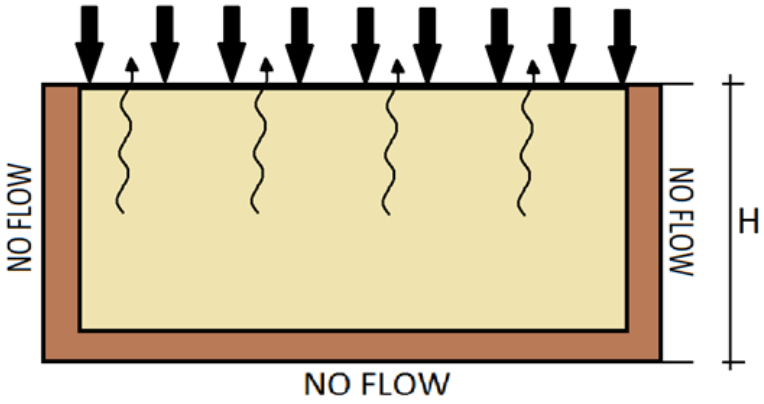

Figure 4.1 Demonstration of Terzaghi's 1-D consolidation

The upper surface is fully drained and the lower and the lateral surfaces are kept as no-flow boundary condition. A constant vertical stress is then applied on the top surface of the soil sample. In the beginning, the experiment acts like a confined undrained condition since the stress is applied instantaneously and that increase in stress is carried entirely by the pore fluid. As time passes, the pore water starts leaking out through the top surface and the following things are observed -

- a decrease in pore water pressure
- an increase in soil effective stress
- a decrease in soil volume due to vertical settlement of the sample

Rate of consolidation depends on the following factors -

- soil compressibility and hydraulic conductivity or permeability
- distribution of initial excess pore water pressure

- drainage boundary condition

Consolidation test is usually carried out on clay like soil where the permeability is very low. This makes a clay soil sample to take a long time to undergo considerable amount of consolidation. The general differential equation for one-dimensional consolidation [Verruijt, 2013] is given by-

$$\frac{\partial p}{\partial t} = \frac{\alpha m_v}{S + \alpha^2 m_v} \frac{\partial \sigma_{zz}}{\partial t} + \frac{k}{\gamma_f (S + \alpha^2 m_v)} \tag{4.1}$$

where, p is pore water pressure, α is Biot's coefficient, S is the storativity of the pore space, k is the permeability coefficient or hydraulic conductivity of the porous soil sample, γ_f is the unit weight of the pore fluid, σ_{zz} is the applied vertical stress, and m_v is the confined compressibility of the porous soil. The storativity S is given by-

$$S = nC_f + (\alpha - n)C_s \tag{4.2}$$

where, C_f is the fluid compressibility and C_s is the compressibility of the soil skeleton. Biot's coefficient involves C_s and can be expressed as:

$$\alpha = 1 - \frac{C_s}{C_m} \tag{4.3}$$

where, C_m is the compressibility of the porous medium, which is the inverse of the soil compression modulus, K. The confined compressibility m_v of the porous medium is given by-

$$m_v = \frac{1}{K + \frac{4}{3}G} \tag{4.4}$$

where, G is the shear modulus of the porous medium.

In a 1-D case under constant vertical loading, Terzaghi provided the following equation [see also in Chapter two] for consolidation:

$$\frac{\partial p}{\partial t} = c_v \frac{\partial^2 p}{\partial z^2} \qquad for\ t > 0 \tag{4.5}$$

At time $t = 0$, a vertical load is applied instantaneously for which it becomes an undrained condition. But for $t > 0$, the soil undergoes consolidation with drained condition at the top boundary. Here, c_v is the coefficient of consolidation and given by-

$$c_v = \frac{k}{\gamma_f (S + \alpha^2 m_v)} \tag{4.6}$$

The initial condition at time $t = 0$, is established from equation (4.1) by noting that there is no fluid loss at that instant. Therefore, ignoring the second term of that equation we get:

$$at\ time\ t = 0,\ \ p = p_0 = \frac{\alpha m_v}{S + \alpha^2 m_v} q \tag{4.7}$$

Assuming fluid and solid particles as incompressible, Biot's coefficient $\alpha = 1$, and $S = 0$, we get

$$p_0 = q,\ \ the\ applied\ vertical\ stress$$

The boundary conditions are given by -

Top surface: $t > 0,\ z = 0,\ \frac{\partial p}{\partial z} = 0$

Bottom surface: $t > 0,\ z = h,\ \ p = 0$

The complete analytical solution [Verruijt, 2013] of the Terzaghi's one-dimensional consolidation problem is given by-

$$\frac{p}{p_0} = \frac{4}{\pi} \sum_{k=1}^{\infty} \frac{(-1)^{k-1}}{2k-1} \cos[(2k-1)\frac{\pi}{2}\frac{z}{h}] \exp[-(2k-1)^2 \frac{\pi^2}{4} \frac{c_v t}{h^2}] \tag{4.8}$$

This is a dimensionless solution where the dimensionless parameters are given by -

time parameter, $t_v = \frac{c_v t}{h^2}$

dimensionless depth $= \frac{z}{h}$

dimensionless pressure $= \frac{p}{p_0}$

The advantage of this dimensionless solution is that we will have to solve this equation only once; we can then use this to solve any case by converting the dimensioned variables into the above three dimensionless variables.

4.2.1 Numerical solution

Equation (4.5) is solved numerically by using finite difference method as follows:

$$\frac{p(z,t+\Delta t)-p(z,t)}{\Delta t} = c_v \frac{p(z+\Delta z,t)-2p(z,t)+p(z-\Delta z,t)}{\Delta z^2} \tag{4.9}$$

Writing $p(z,t)$ as $p_i(t)$, $p(z+\Delta z,t)$ as $p_{i+1}(t)$ and $p(z-\Delta z,t)$ as $p_{i-1}(t)$, the above equation can be expressed as:

$$p_i(t+\Delta t) = p_i(t) + \delta\{p_{i+1}(t) - 2p_i(t) + p_{i-1}(t)\} \tag{4.10}$$

where $\delta = \frac{c_v \Delta t}{\Delta z^2}$, Δz being the vertical displacement due to applied constant overburden load for a corresponding time Δt.

In TOUGH-PyLith coupled simulator, Δz is calculated in the geomechanics code, PyLith.

From the initial condition the pore pressure values at time t=0 are known. The pressure values at time $t = \Delta t$ are then calculated for $i = 1,2,3, \ldots \ldots n-1$. The value corresponding to $i = n$ is calculated from the boundary condition at the top and the value corresponding to $i = 0$ is calculated from the boundary condition at the bottom.

4.2.2 Simulation using TOUGH-PyLith

We use a 1-D vertical soil column of 31 elements, each element being 1x1x1 m in dimension. Figure 4.2 shows the meshed geometry from Cubit pre-processor. We use a free flow boundary condition in TOUGH2 by adding an additional element on the top and giving it a high

volume and setting it to atmospheric pressure of 0.1 MPa. The high volume acts as a sink and since it is set to a constant atmospheric pressure, it will not change the value of this high-volume element .

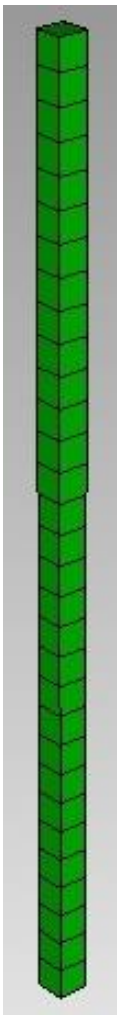

Figure 4.2 Soil column specimen for simulation of Terzaghi's 1D consolidation problem

with time. All other sides are by default no-flow boundaries since they do not have any connections to other elements. This is what required to simulate Terzaghi's problem since fluid is only allowed to flow through the top surface. Table 4.1 lists the geometry dimension, material properties, and boundary conditions.

Table 4.1 Dimensions and properties of the specimen for simulation of Terzaghi's problem

Formation	
Rock density	2200 kg/m^3
Porosity	42.5%
Permeability	$6.51x10^{-15}$ m^2
Pore compressibility	$2.5x10^{-10}$ Pa^{-1}
Saturation	1.0
Column Height	31 m
V_S	500 ms^{-1}
V_P	1500 ms^{-1}
Initial and Boundary Conditions	
Overburden on top surface	10.1 MPa
Temperature	25 ºC
Liquid saturation	1.0
Boundary conditions	Free flow on top; no flow along all other faces

The simulation is run as a no-gravity computation. TOUGH is initialized with an initial overburden pressure of 10.1 MPa on the top surface. As soon as a uniform compressive load of 10.1 MPa is applied through the top surface on the specimen, the fluid-saturated soil skeleton compacts and an undrained pore water pressure response is observed at time $t = 0^+$. The undrained pressure response due to sudden application of a compressive load is known as

Skempton effect [Skempton, 1954]. The undrained pressure response is equal to the overburden pressure applied i.e. 10.1 MPa which is used to initialize the drained portion of the simulation for times larger than t = 0 s. Since there is a steep pressure gradient between the top surface and the rest of the saturated soil specimen, the simulation continues to run until the pressure gradient diminishes. This simulation is done in steps where the flow simulator, TOUGH, provides pressure output for each time step and the geomechanics simulator, PyLith, runs for the corresponding time step to account for stress and deformation. There is no feedback of stress dependent porosity or permeability changes to the flow simulator TOUGH. Hence, this simulation represents a one-way coupling phenomenon and a successful demonstration of TOUGH-PyLith coupled code execution. The total time for the simulation is 8 years and it ensures a steady state solution.

Results from the simulation are visualized in VisIt software. Figure 4.3 shows the displacement in the soil column at the end of simulation. As expected, maximum displacement is computed at the top which is about 1.86 cm and minimum displacement is zero which is located at the bottom. Also, shown are the vectors for displacement that are acting downward. Since the displacements normal to each of the surfaces are restrained (except the top surface), the only settlement occurs along the vertical column.

The pore pressure results from Terzaghi's problem simulation are plotted against the analytical solution with respect to dimensionless time $t_v = \frac{c_v t}{h^2}$ and dimensionless depth $\frac{z}{h}$. This is shown in Figure 4.4. We plot results for three characteristic dimensionless times t_v= 0.01, 0.02, and 0.1 respectively. They all show good agreements with the analytical solutions. Note at the ground surface (i.e. z = 0), pressure is zero at all times which means water near the ground surface leaks out immediately the load is applied on the specimen. As depth from the ground

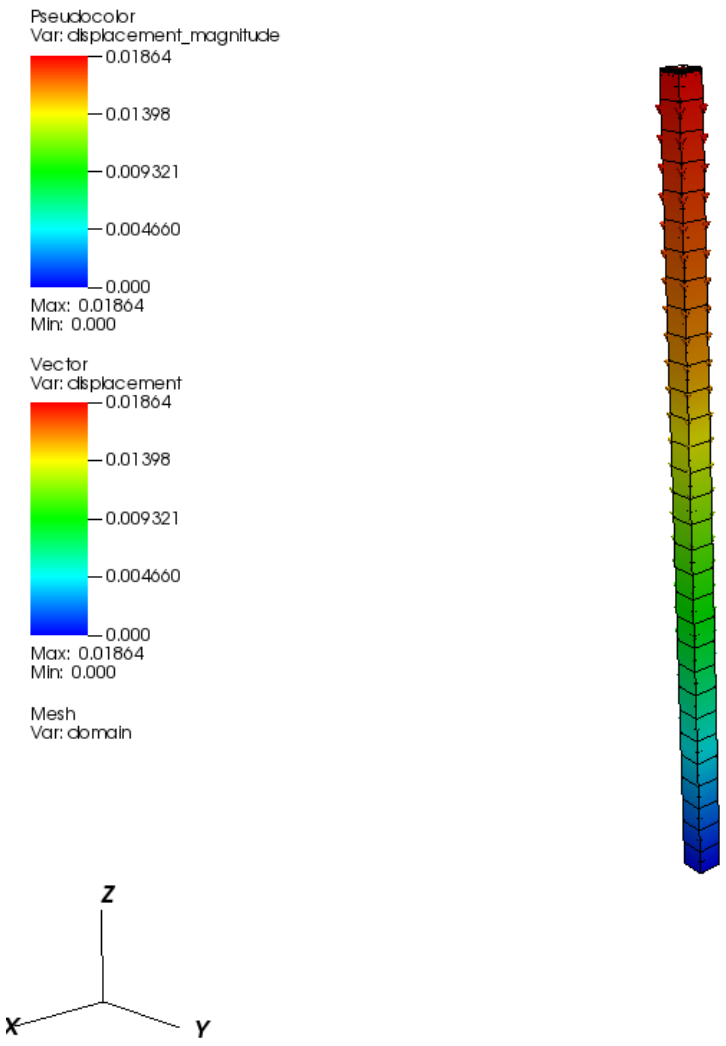

Figure 4.3 Displacement in the soil column from Terzaghi's problem simulation

surface increases, so does the pressure at any time instant. The advantage of using dimensionless parameters are that we can use any other specimen with any other parameters in order to show the agreement with the analytical solutions.

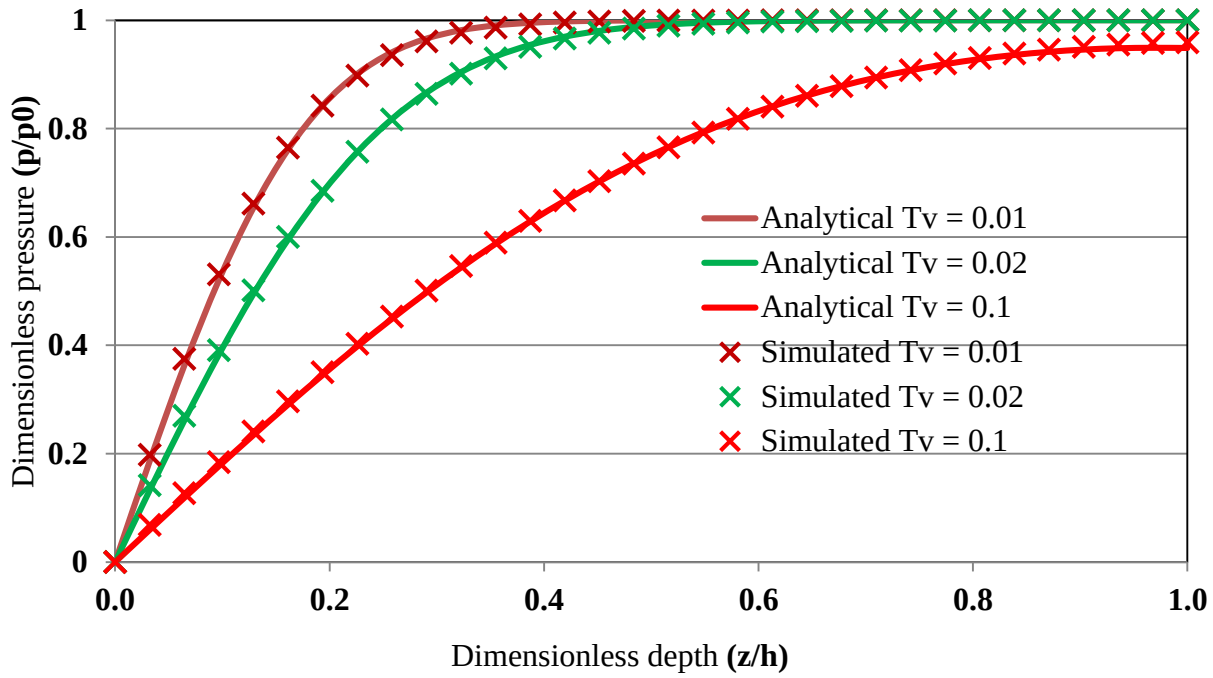

Fig 4.4 Comparison of pressure evolution results in Terzaghi's 1-D consolidation

4.3 Mandel's Problem

Mandel's problem [Mandel, 1953; Abousleiman et al., 1996] is an example of coupled poroelasticity with two-way coupling i.e. both fluid-to-solid and solid-to-fluid. Mandel [Mandel, 1953] showed that for three dimensional consolidation [Biot, 1941] pore water pressure response is non-monotonic. Later, Cryer [Cryer, 1963] presented similar results for fluid-saturated sphere undergoing all-around compressive stress. The non-monotonic pressure effect is known as Mandel-Cryer effect [Schiffman et al., 1969; Gibson et al., 1990]. Unlike classical uncoupled Terzaghi's consolidation theory, Mandel's problem clearly demonstrates the coupled phenomenon of soil consolidation and provides an analytical solution for non-monotonic pressure response. Later Abousleiman et al. [1996] extended this solution to include material transverse isotropy, pore fluid compressibility, and the compressibility of soil-rock skeleton.

Mandel's problem (Figure 4.5) consists of an infinitely long rectangular specimen. The top and bottom surface are no-flow boundary conditions with free-flow boundary conditions on the lateral sides. Like the classical Terzaghi's problem, a sudden uniform compressive stress is applied to the rigid and frictionless plates on top and bottom. Due to undrained response of the pore water pressure at time $t = 0^+$, Skempton effect is observed. With time pore water starts to leak out through the lateral sides. The sudden raise of pore water pressure inhibits the compression of the specimen adding to the apparent compressive stiffness. The sides of the specimen being more amenable to drainage, an equivalent compressive load is transferred to the stiffer central region. Consequently, pore water pressure response at the center of the specimen becomes greater than the applied compressive pressure on the specimen. In other words, generated pore water pressure at the center of the specimen is non-monotonic. Several numerical codes [Christian and Boehmer, 1970; Cheng and Detournay, 1988; Cui et al., 1995] have used the Mandel's analytical solution for testing their validity of simulating coupled poroelasticity problem.

4.3.1 Problem definition

Mandel's problem can be idealized as a 2D plane strain problem since it is a long specimen with rectangular cross section where deformation along the y direction or perpendicular to the xz plane is essentially negligible. The displacement and flux vanish along the z direction. The boundary conditions are:

$$\sigma_{xx} = \sigma_{xz} = p = 0, \qquad at\ x = \pm a \tag{4.11}$$

$$\sigma_{zx} = q_z = 0, \qquad at\ x = \pm b \tag{4.12}$$

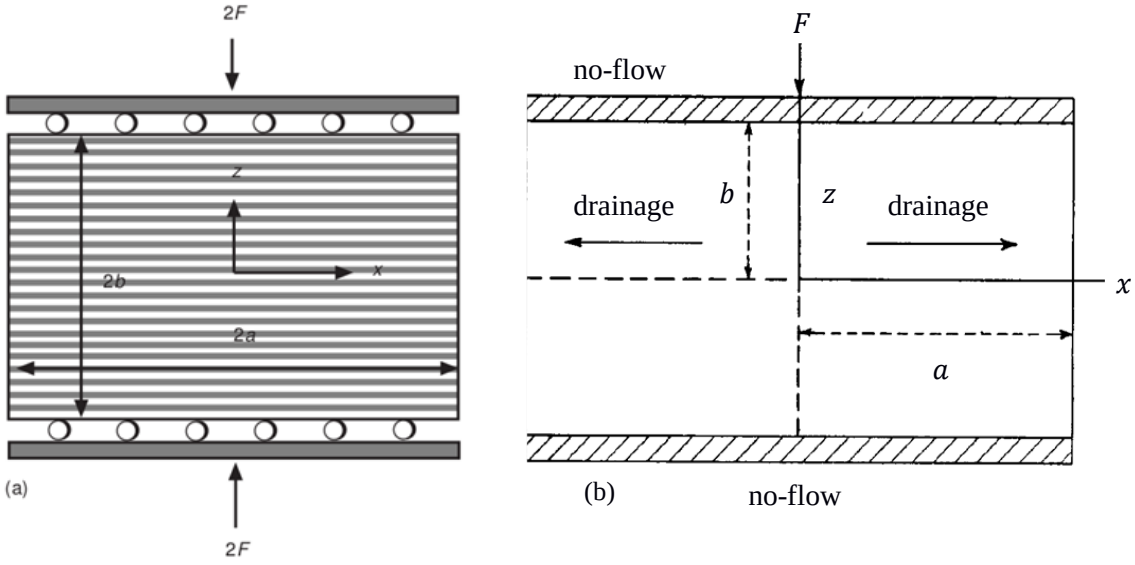

(a) Abousleiman et al., 1996

(b) Mandel, 1953

Figure 4.5 Mandel's problem description with associated boundary conditions

$$q_z = constant, \qquad at\ \ z = \pm b \tag{4.13}$$

$$\int_{-a}^{a} \sigma_{zz} = -F, \ \ at\ \ z = \pm b \tag{4.14}$$

Under these conditions, Mandel provided the following equation for the evolution of pore pressure:

$$q = \sum_i A_i (\cos \frac{\alpha_i x}{i} - \cos \alpha_i)\, e^{\frac{-\alpha_i^2 ct}{a^2}} \tag{4.15}$$

where,

$$A_i = \frac{p_0(\lambda + 2\mu)\cos \alpha_i}{\mu - (\lambda + 2\mu)\cos^2 \alpha_i} \tag{4.16}$$

Here, λ and μ are Lame constants. p_0 is the initial or undrained pore water pressure response and α_i are the directional Biot's coefficient under drained condition. α_i satisfy the following equation:

$$\tan \alpha = \frac{\lambda + 2\mu}{\mu} \alpha \tag{4.17}$$

4.3.2 Simulation with TOUGH-PyLith

For simplicity and convenience of simulation we idealize [see Jha, 2014] Mandel's problem as shown in Figure 4.6. We increase the aspect ratio of the domain and apply a compressive load on the shorter side so that any imprecision in applying the load does not contaminate the pressure and displacement at the observation point far from the load boundary.

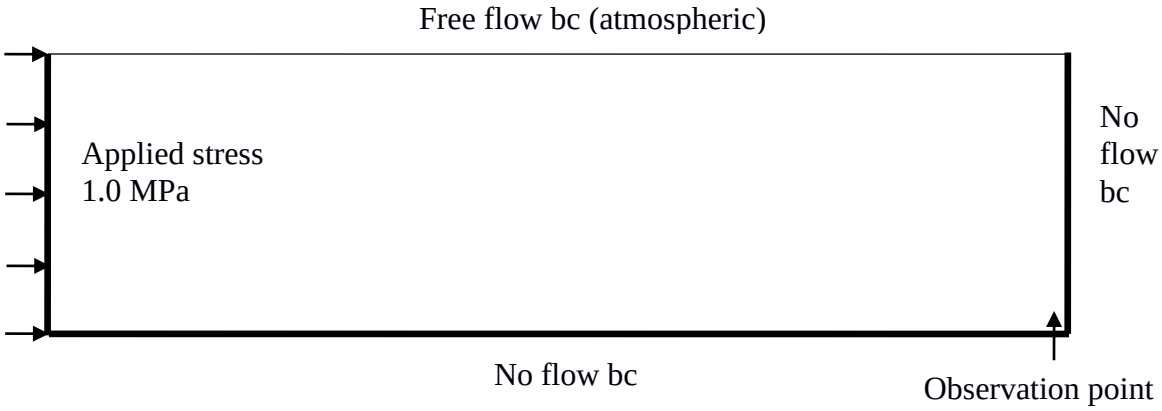

Figure 4.6 Idealization of Mandel's problem for simulation with TOUGH-PyLith

This happens due to the softening or bending of the specimen at the drained boundary (top edge) and near the load boundary surface during the pressure dissipation. Water at that location leaks out immediately upon load application thereby bending it and causing differential displacements along the load boundary. But this is a clear violation of the Mandel's boundary condition of load application at constant rate displacement. In order to prevent that, we select an observation point as shown in Figure 4.6. We apply 1 MPa stress on the left face (-x) of the specimen horizontally along the x direction. The free flow boundary is applied along the top surface. All other surfaces

permit no flow through them. The displacements on the positive and negative y faces, positive x face, and negative z face are restricted to be zero at all times.

Because of all the boundary constraints, the specimen is allowed to expand only along the top surface with changes in flux in that direction. In order to properly define the constant pressure free flow Dirichlet boundary conditions in TOUGH2, additional elements are added on the +x and -x sides of the specimen. This is achieved by assigning very large volumes (say 10^{50}) and a prescribed pressure of the each additional element adjacent to the original volume elements. As a result, the thermodynamic conditions at those interfaces do not change from the interaction between the constant pressure high volume elements (additional elements) and variable pressure finite volume elements (original specimen). Thus, we are able to maintain a constant pressure boundary condition in the flow code TOUGH2.

Figure 4.7 shows the specimen along with its meshed volume (50m x 10m x 0.5m) created in Cubit. It has a total of 2000 elements (0.5m x 0.5m x 0.5m each).

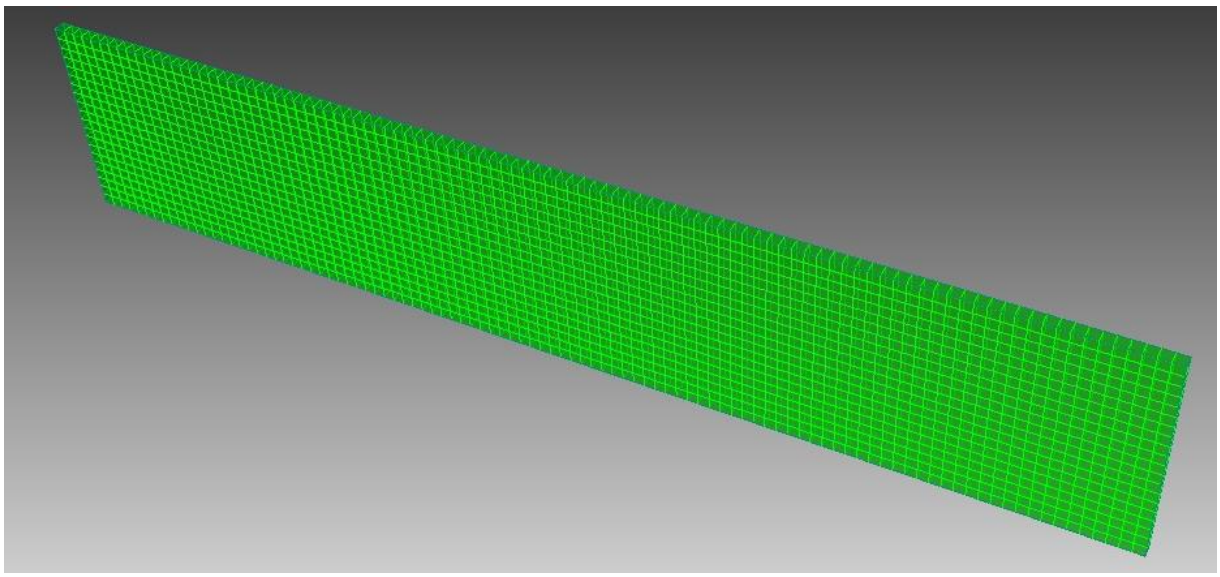

Figure 4.7 Specimen for simulating Mandel's problem in TOUGH-PyLith (2000 elements)

4.4 Validation Against Mandel's Solution

Figure 4.8 shows the plots of pressure evolution of the observation point. The solid red line shows the analytical solution and the blue line shows the results simulated by TOUGH-PyLith. Both analytical and simulation results start out at 1 MPa applied stress. With time, due to Mandel's effect described before, they start rising. The peak pressure response predicted by the TOUGH-PyLith simulation is very close to the analytical solution. However, simulation results seem to drain a bit faster than the one predicted by Mandel.

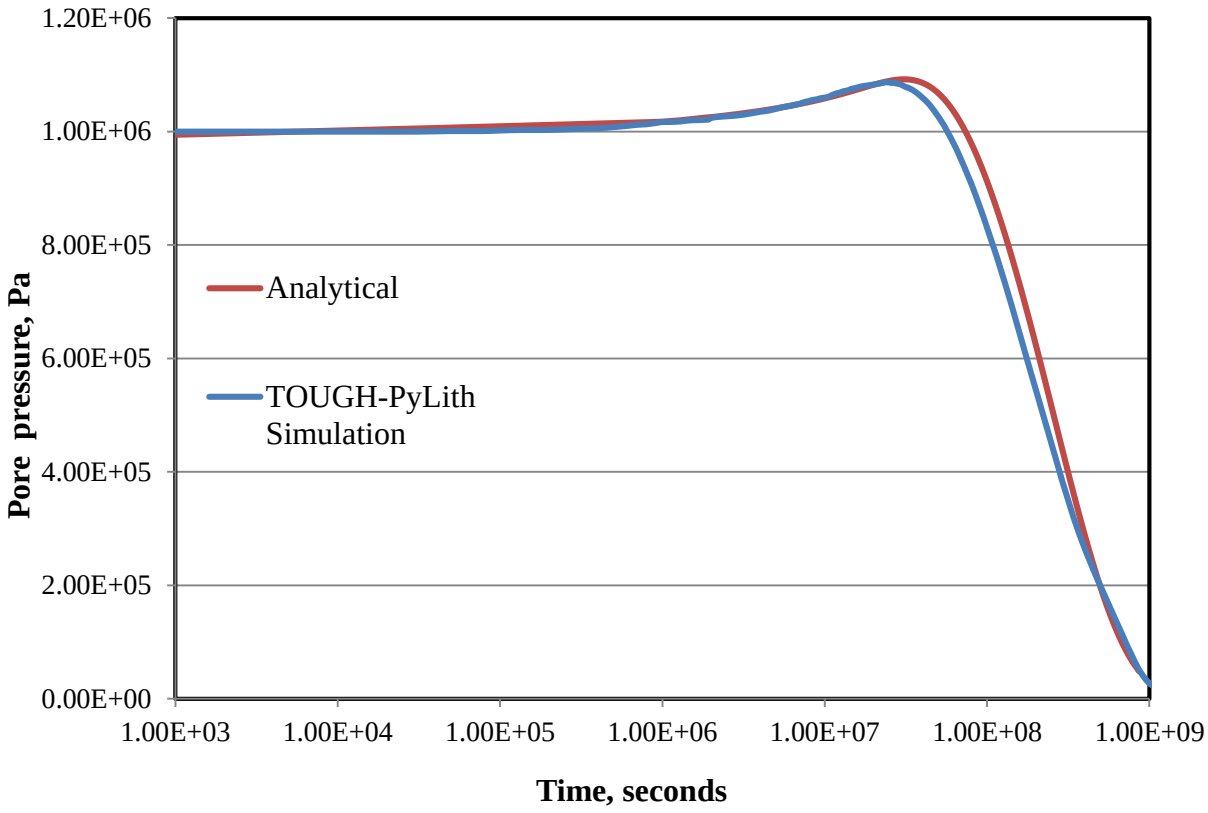

Figure 4.8 Comparison of simulation results with Mandel's analytical solution

CHAPTER V

HYDRO-GEOMECHANICAL SIMULATION OF EARTHQUAKES INDUCED BY FLUID INJECTION

5.1 Introduction

This chapter describes an application of the developed coupled hydro-geomechanical methodology to simulate earthquake nucleation and slip distribution along the fault, induced by subsurface fluid injection in conjunction with far-field tectonic loading. Hydro-mechanical modeling to simulate induced earthquakes from geological CO_2 storage has previously been carried out by iteratively coupling TOUGH2 with the geomechanics code FLAC3D [Cappa and Rutqvist, 2012]. The main limitation in using FLAC3D as the mechanical code is that, unlike PyLith, it was not developed specifically for large-scale quasi-static and dynamic earthquake computation. Furthermore, it does not contain the rate- and state-dependent frictional model that can describe earthquake-like stick-slip behavior more completely.

Jha et al. [Jha and Juanes, 2014] have recently developed a computational code by coupling a fluid flow code, General Purpose Reservoir Simulator (GPRS) [Cao, 2002; Pan and Cao, 2010] and geomechanics code PyLith for simulating coupled fluid flow and reservoir geomechanics. They have demonstrated their code applicability to induced seismicity simulation from subsurface CO_2 injection by using a rate- and state-dependent friction law in the fault constitutive model. The fluid flow code (TOUGH2) used in this research, however, is more

robust and widely used among the scientific community. At present, we are not accounting for thermo-poroelasticity effects [e.g., Kohl et al., 1995, 1998; Ghassemi et al., 2003], but fluid pressure effects on the stress field, and stress-dependent porosity and permeability changes as the coupling parameters from mechanics to flow. However, since in the long run we are interested in simulating earthquake dynamic rupture and wave propagation, our coupled approach requires relatively expensive, large-scale computations, with sequential solution of the flow and mechanics problems [Kim, 2011].

5.2 Application to Induced Seismicity

This section describes a successful demonstration of the TOUGH-PyLith coupled simulator to compute induced seismicity from water injection at an enhanced geothermal reservoir. In an existing geologic setting, a fault is usually stressed tectonically for years. In order to replicate that stress condition we apply an initial displacement and a displacement rate boundary conditions on the two sides of a domain and run it for a period of 100 years. The stress field and fault tractions from this simulation are then used as initial conditions for the subsequent runs.

5.2.1 Model geometry

We use a simple 5400 m x 4500 m x 2700 m 3D domain (Figure 5.1) in order to demonstrate the induced seismicity modeling capability of our coupled simulator. It has a 100 meter thick reservoir at a depth of 1300 m from the ground surface. A vertical fault is located in the half way from the negative x-boundary and it is along the YZ plane. The reservoir is 100m thick shown as thick black line in the halfway along the depth (Z axis). The rock properties,

initial conditions, and other geometric and hydrogeological parameters are listed in Table 1. An injection well is located at distance of 1 km from the fault and at reservoir depth level of 1350 m from the ground surface. Figure 5.2 shows the meshed geometry produced in Cubit. The coarsest mesh is of size 900 m x 900 m x 900 m and the finest mesh is of 100 m x 100 m x 100 m .

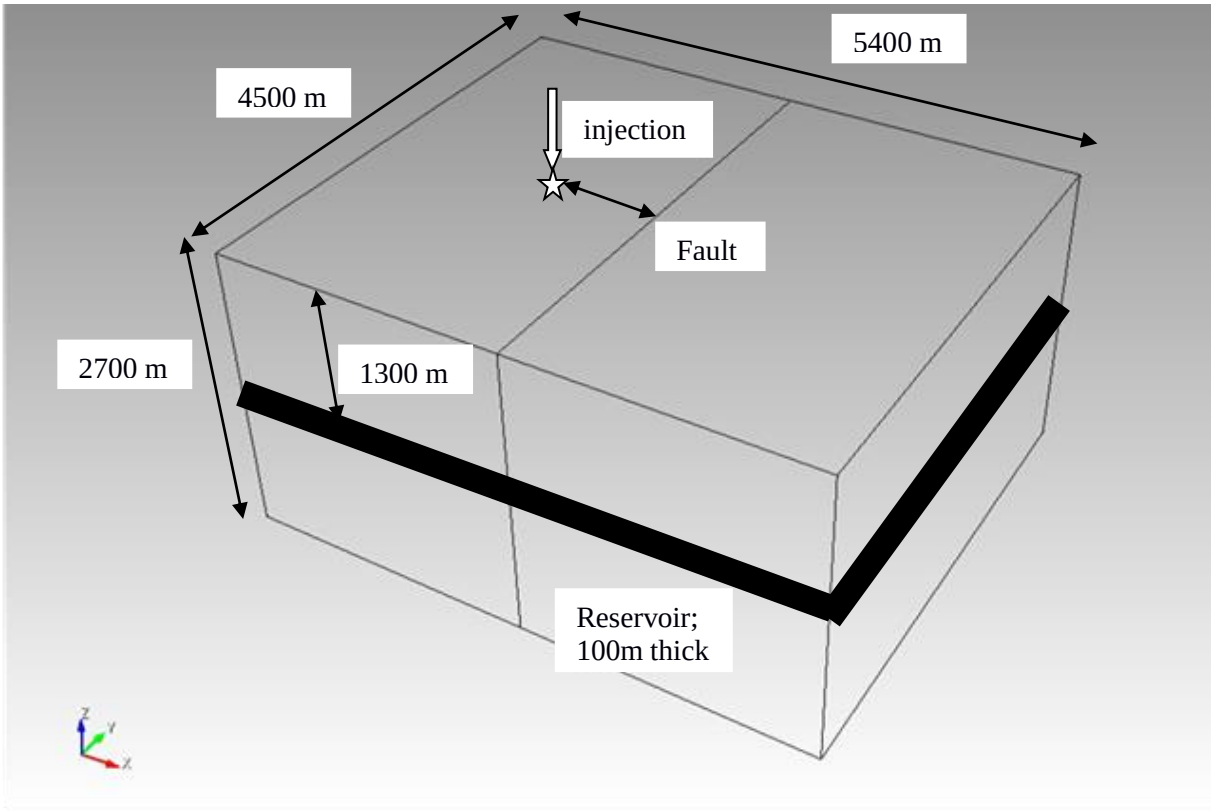

Figure 5.1 Dimensions of the geometry for the application problem

Mesh is refined near the fault and injection well in order to get noticeable amount of pressure change from the water injection. The domain geometry is created and meshed separately for each of the codes due to their compatibility issue. TOUGH2 does not work on Graphical User Interface (GUI) based geometry modeling and simulation running. It uses a command prompt in

Windows platform and terminals for Mac and Linux machines. The two grids, one that produced by TOUGH2 (flow grid) and the other produced by PyLith (mechanics grid), are then mapped by using a mapping algorithm.

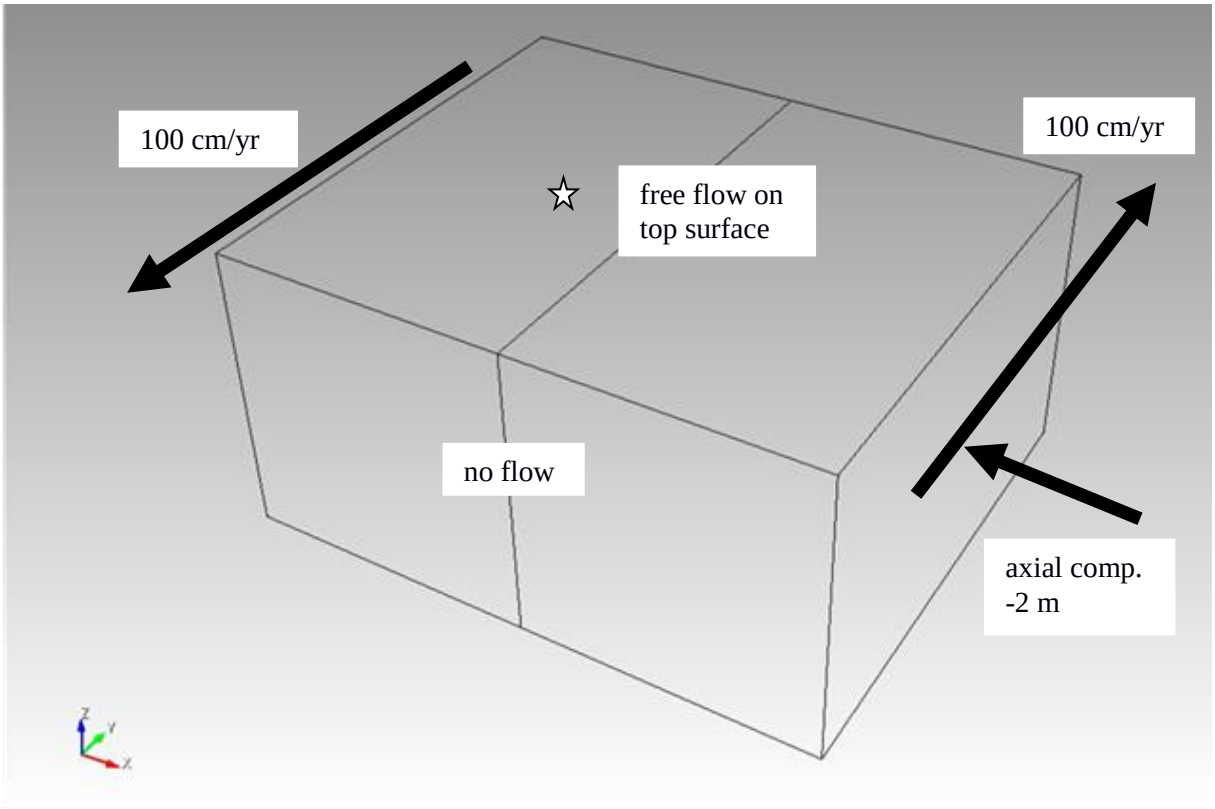

Figure 5.2 Assigning boundary conditions: (i) free flow b.c. on top and no-flow b.c.s on all other surfaces for fluid flow problem (ii) left-lateral tectonic loading and an axial compression for geomechanics problem

The domain consists of a total of 630 trilinear hexahedral elements which are created separately in TOUGH2 and PyLith. The different colors of the gridded domain indicate different subdomains that can be assigned different rock material properties. For simplicity we use only elastic rock material properties in this preliminary model. By defining various subdomains, we are also able to request our outputs in the desired rock type at the desired locations.

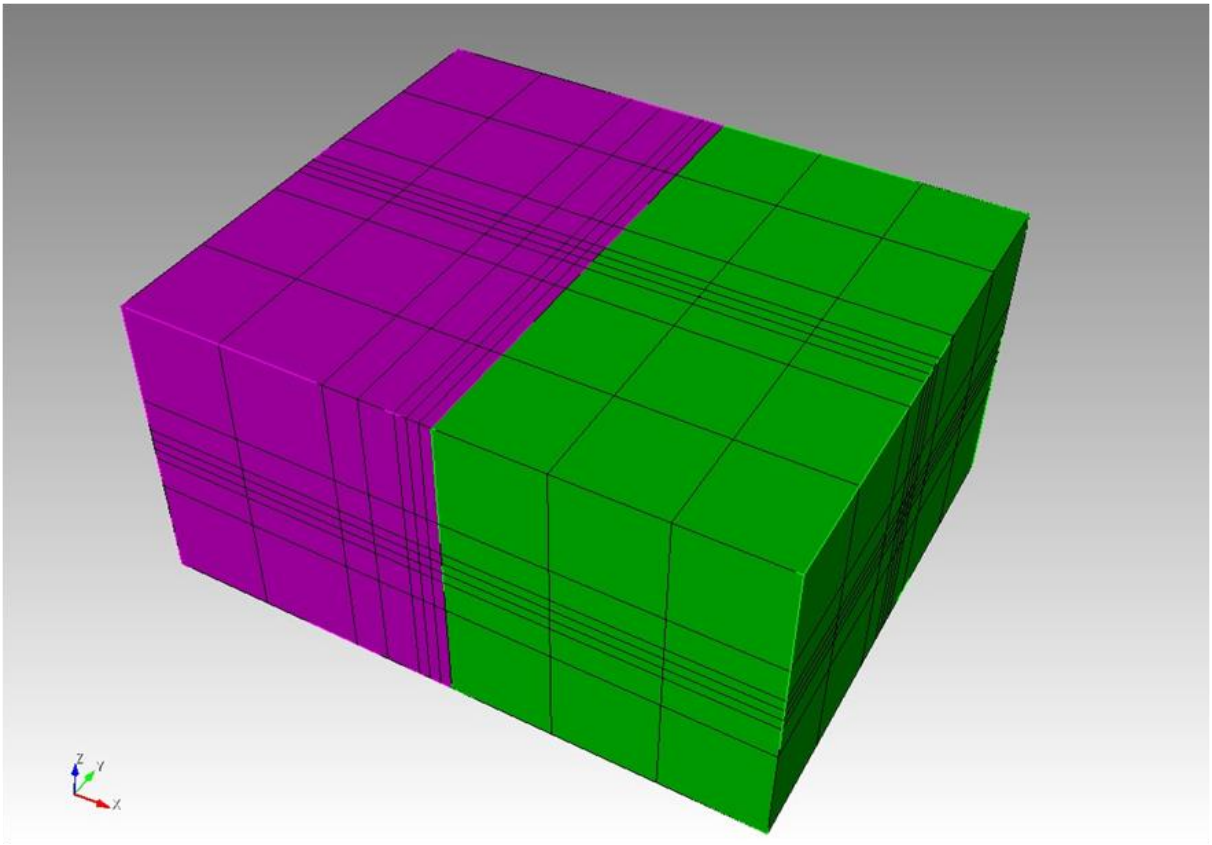

Figure 5.3 Meshed geometry, refined in the vicinity of injection well and fault

5.2.2 Initial and boundary conditions

Since the two different codes (i.e. TOUGH2 and PyLith) for two different physical problems (i.e. fluid flow and geomechanics) are involved in simulation of a coupled hydro-geomechanical and poroelastic problem, they have to be initialized independently before running together in order to simulate the most realistic conditions. Table 5.1 lists some of the properties, and initial and boundary conditions for both codes.

Flow code TOUGH2 is initialized with a fully-saturated condition and by turning on the gravity to simulate the hydrostatic pressure condition in addition to the lithostatic stress condition specified by the overburden rock. Permeability value along the x axis is used as

$6.51x10^{-15}$ m^2 whereas it is relatively impermeable along the y and z axes. This is done in order

Table 5.1 Input parameters including initial conditions and rock properties

Formation	
Rock density	2200 kg/m^3
Water density	1000 Kg/m^3
Porosity	42.5 %
Permeability along x dir.	$6.51x10^{-15}$ m^2
Permeability along y and z dir.	$6.0x10^{-28}$ m^2
Initial and Boundary Conditions	
Temperature	25 ºC
Liquid saturation	1.0
Pressure on top surface	Atmospheric
Pressure on all other surfaces	Hydrostatic
Traction on +x and -x sides	100 cm/year
Axial compression +x side	-2.0 m
Injection	
Pattern area	5400 m x 4500 m
Depth	2700 m
Reservoir thickness	100 m
Injection depth	1300 m
Injection rate	0.01 kg/s

to see the effect of fluid pressure on the fault by channeling more flow towards the fault from the injection point. Water density is 1000 kg/m^3 with a constant temperature (assumed) of 25 ºC.

Since we are only considering the effect of pressure field on fault, the temperature effect is not considered in the current research scope. TOUGH2 is run for sufficiently long time in order to achieve the hydrostatic pressure equilibrium throughout the domain.

Mechanics code is initialized by putting on an overburden by means of rock density and turning on the gravity. But turning on gravity produces unrealistic amount of deformation which results in convergence problem of the nonlinear equation solver in the code. Although the rock domain is under in lithostatic stress condition, the deformation is assumed zero in that gravity equilibrium. Therefore in the simulation, an initial stress is used in a spatial database to make the initial displacement essentially zero. In applying rate- and state-friction model, a reference coefficient of friction of 0.4, reference slip rate of 1.0e-3 m/s, characteristic slip distance of 0.02 m, coefficients a and b of 0.008 and 0.012, and zero cohesion are used. The initial values of the state variable are set so that the fault is in equilibrium for the initial tractions. As boundary conditions, we constrain the slip to be in the y-direction faces and apply a steady-state secular slip velocity of 100.0 cm/year in the y-direction. Dirichlet boundary condition on the positive x face is -2.0 m. The bottom face of the domain is fixed at zero displacement. The simulation is run for a year with an injection rate of 0.01 kg/s.

5.2.3 Simulation run cases

After properly assigning the initial and boundary conditions and using the initial stress conditions from the first 100 years run, we run the following two cases:

a. Run a simulation for a period of 150.0 years with tectonic loading alone

b. Run a second simulation for the same time period in conjunction with fluid injection and tectonic stress

The results obtained from the above two cases are compared against each other in order to see the differences in evolution of stress changes, traction on the fault, slips on the fault, and other slip and friction parameters. Thus, it will be evident how the injected fluid is perturbing the reservoir and fault system and if it is causing a premature slip on the fault.

5.2.4 Comparison of the results

We run a total of 300 years of simulation in both cases as stated earlier. We then investigate the stress, traction, and slips on the fault in order to compare the effect of water injection into the domain. Figure 5.4 shows vertical stress in the domain without injection at the end of simulation. Maximum stress is calculated as -89.4 MPa in compression and the minimum stress is found as +56 MPa in tension. This can be explained by thinking of the displacement and displacement rate boundary conditions applied on the positive and negative x boundaries. Since we apply a y- displacement rate (i.e. velocity along y direction) of 100 cm/year in left-lateral sense, i.e. +100 cm/year on the positive x side and -100 cm/year on the negative x side, it is obvious that two of the corners of the domain are moving towards each other causing more compression in those areas (blue corners) while the other two corners are moving away from each other causing tension in those areas (red corners). More precisely, the corners under compression are located at y = - 2250 m on the positive x side and y = 2250 m on the negative x side. Corners under tension are located at y = 2250 m on the positive x side and y = -2250 m on the negative x side.

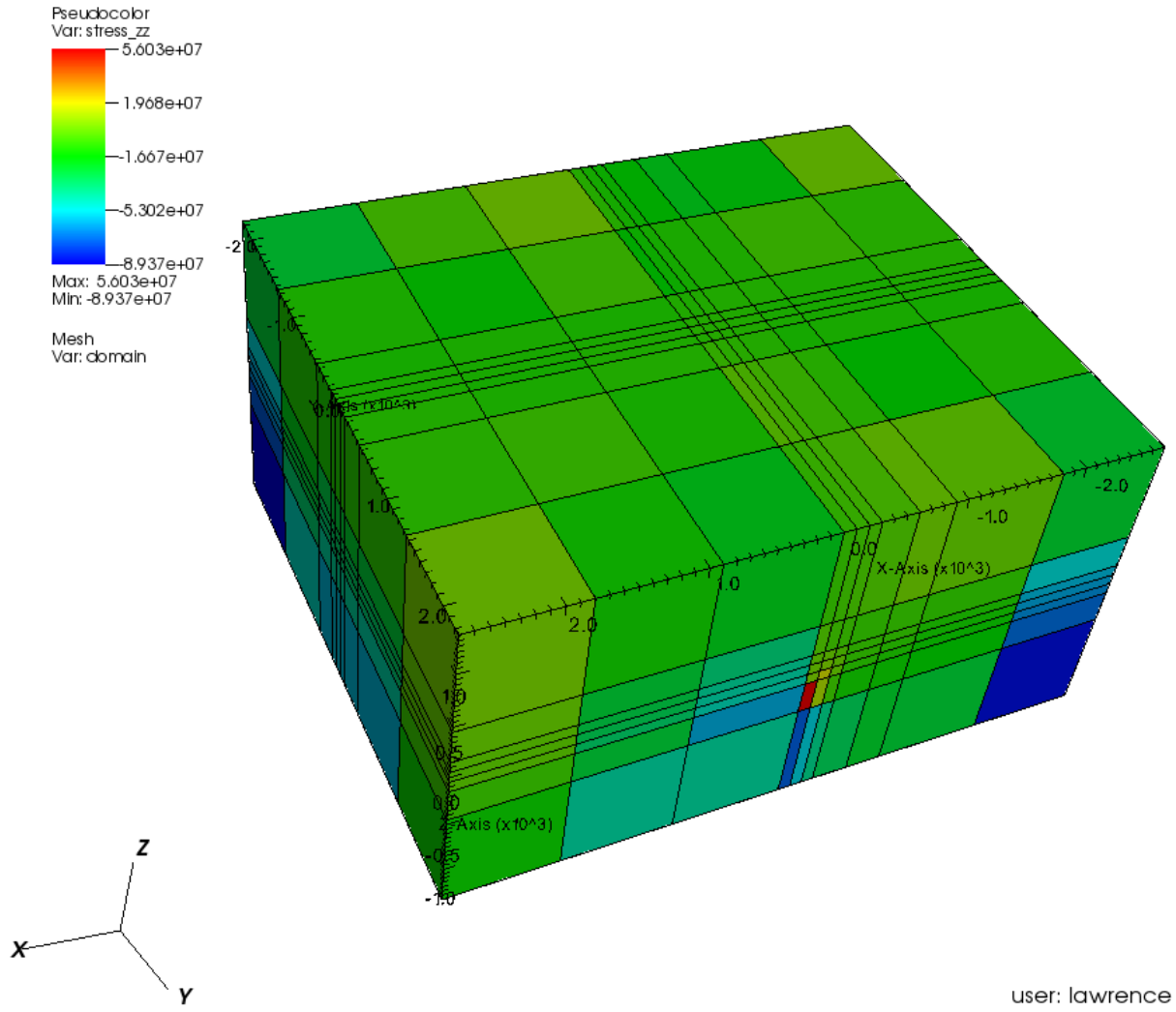

Figure 5.4 Vertical stress distribution in the domain from gravity and far-field tectonic loading after 300.0 years and without injection

Maximum lithostatic stress due to the rock overburden is calculated as -59.4 MPa at a depth of 2700 m from the ground surface. Also, if there was only gravity, then there would have been a uniform increase of vertical stress from the ground surface to the bottom in accordance with the depth (lithostatic condition).

Figure 5.5 shows the vertical stress distribution in the domain at the end of 300 years and including an injection rate of 0.01 kg/s of water for that time period.

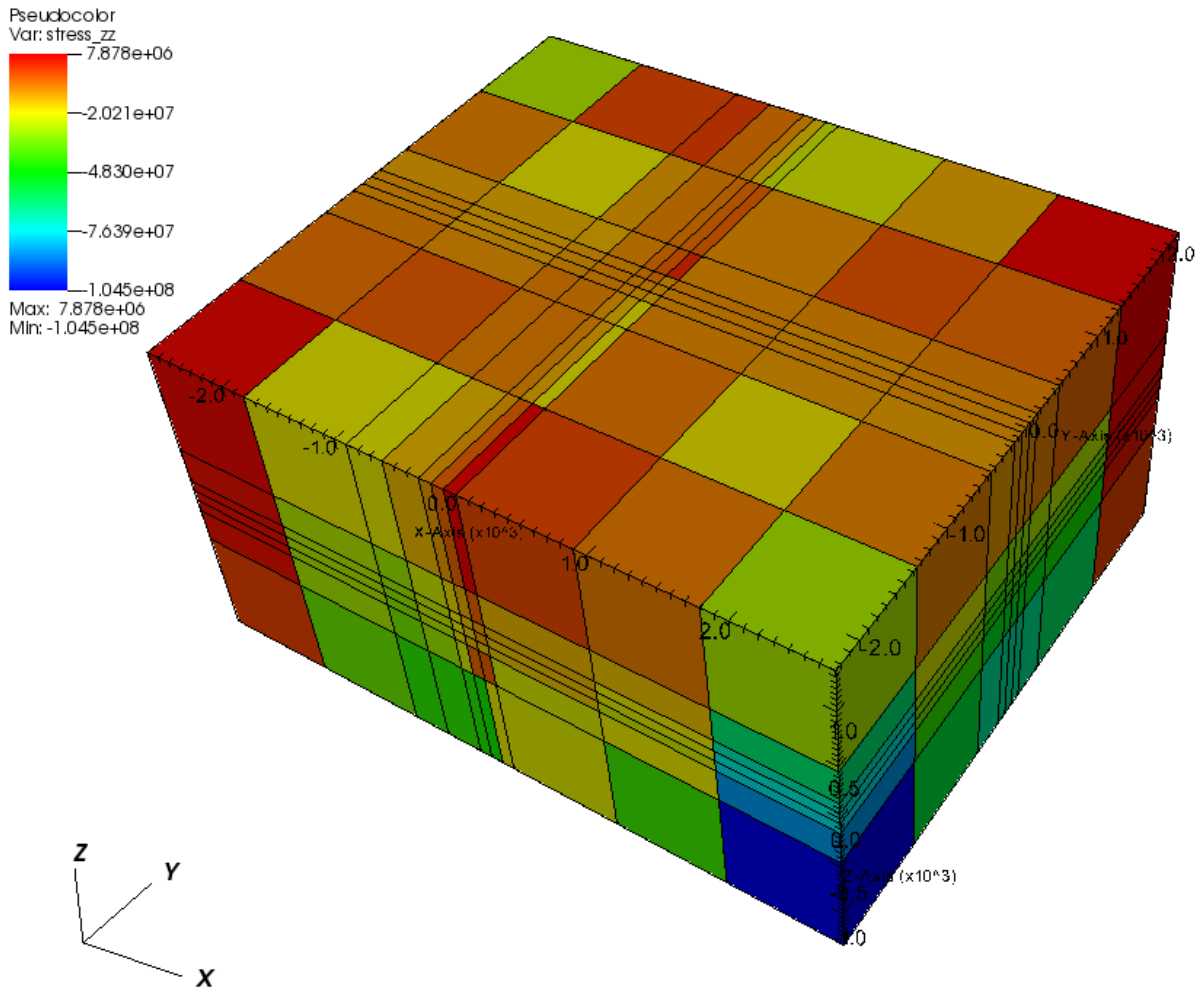

Figure 5.5 Vertical stress distribution in the domain from gravity and far-field tectonic loading after 300.0 years and with injection

The maximum stress is computed as -104.5 MPa in compression at the same corners as in the dry case but the magnitude is larger. There is about -15 MPa more now in the fluid injection case. This is due to the increase in total stress. Before it was just lithostatic stress coming from the rock overburden whereas now there is an additional stress coming from the weight of water injected in the volume over the period of 300 years.

Also, note that the minimum stress is computed as +7.87 MPa in tension which is less than the minimum stress in dry case (+56 MPa). This could be explained by accounting the sense

of fluid pressure generation with compression or tension. As we know, fluid pressure acts in a counter direction in order to oppose the applied stress. In other words, if a fluid-saturated volume undergoes a compression (inward) the pressure increases and acts outward whereas if a volume undergoes a tension or as the volume expands there would be a negative pressure or suction in the domain. Although, we have a free-flow atmospheric boundary condition on the top surface, there is no free flow through any lateral or bottom surface. Under an IFD framework in TOUGH2, if there is no element with connection it is considered a no-flow boundary condition. Consequently, water cannot flow out of these lateral and bottom surfaces which, in turn, causes a high pressure rise inside the domain. Since this is a closed volume except the top surface, increase in water pressure causes increase in total compressive stresses which is more evident in the stress along the x axis as shown in Figure 5.7.

Figure 5.6 shows the horizontal stress distribution in the domain at the end of 300 years and without injection. The maximum stress is computed to be -151 MPa in compression while the minimum stress is calculated as +89 MPa in tension. Both of these values are higher than the maximum and minimum vertical stresses (+56 MPa and -89.5 MPa respectively). Under normal case, the maximum horizontal stress is less than or equal to the maximum vertical stress. But we have an axial compression of -2.0 as a boundary condition which causes an extra compression in the domain. Like it was delineated before in explaining vertical stresses, tension arises due to the far-field displacement rate boundary conditions in y- direction on the positive and negative x sides.

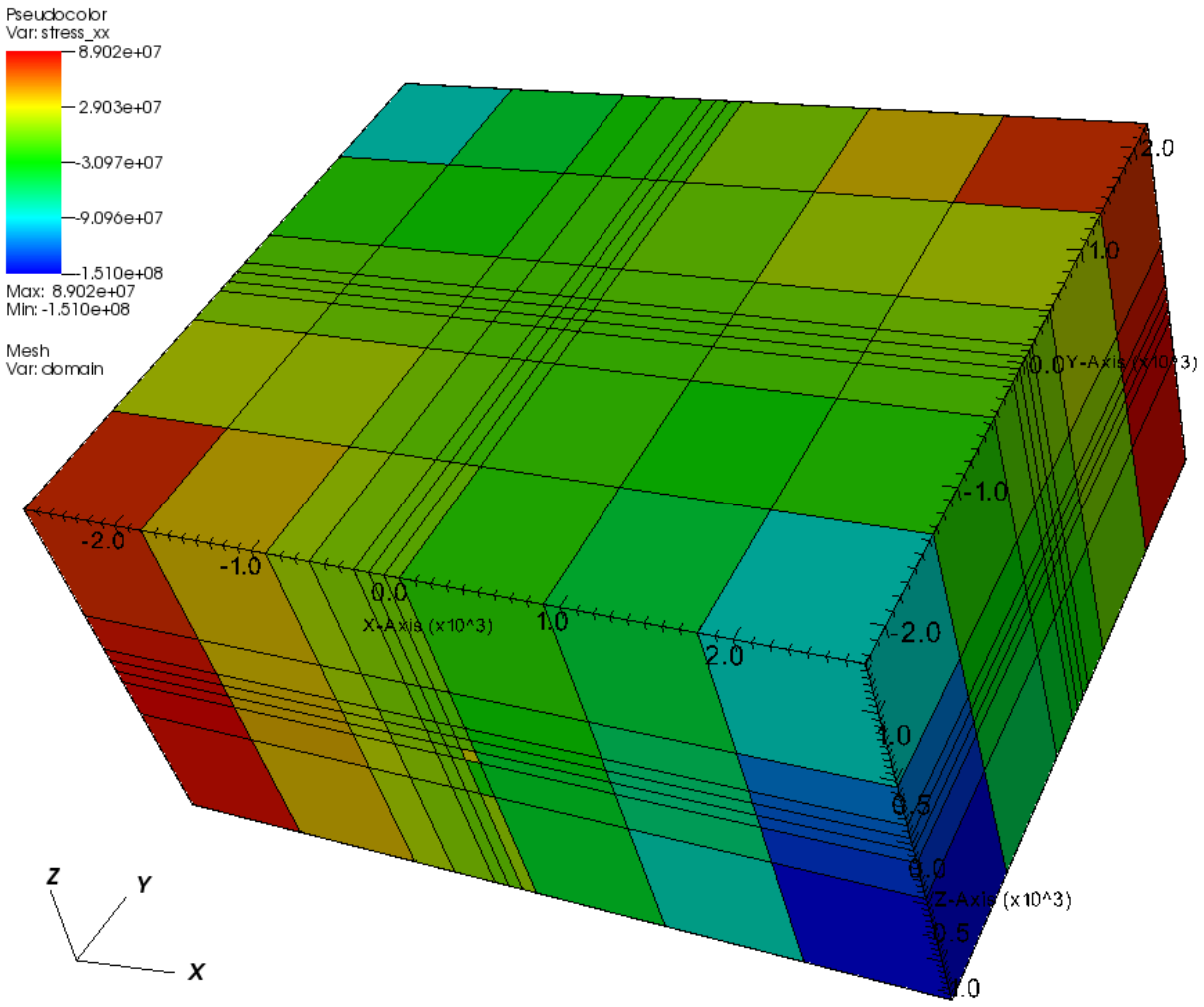

Figure 5.6 Horizontal stress distribution (σ_{xx}) in the domain from gravity and far-field tectonic loading after 300.0 years and without injection

Figure 5.7 shows the horizontal stress distribution in the domain at the end of 300 years and including the water injection. The maximum stress in this case is -197 MPa in compression and the minimum stress is 81 MPa. The locations of these stresses are same as in the dry case but the values are more pronounced in the injection case. Similar reasoning of pore water pressure generation as opposed to applied stresses also apply here.

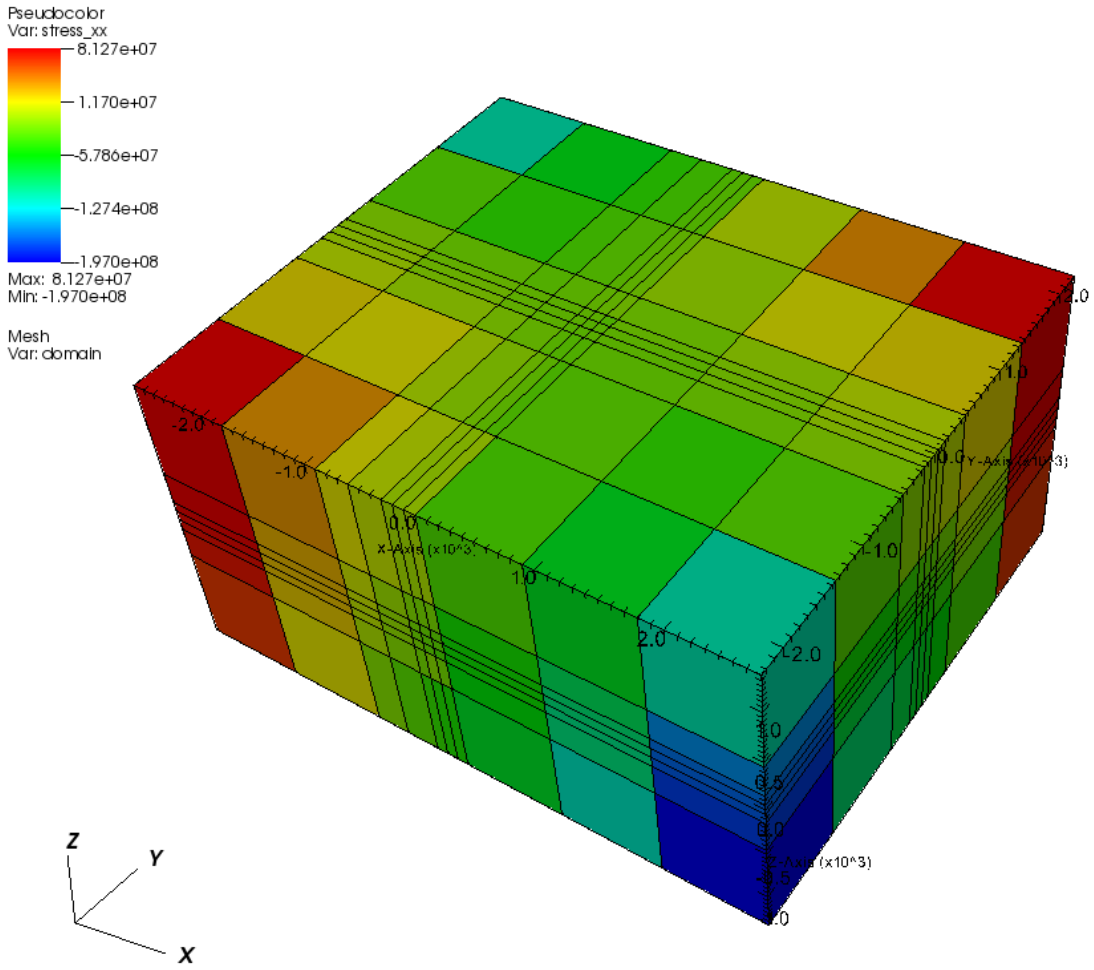

Figure 5.7 Horizontal stress distribution (σ_{xx}) in the domain from gravity and far-field tectonic loading after 300.0 years and with injection

Figure 5.8 shows the displacement in the domain at the end of 300 years and without water injection. Maximum displacement is computed as 318 m which occurs at both positive and negative sides and minimum displacement is computed as 6 m near the central region of the domain. Since we applied a y- displacement rate boundary condition of +1.0 m/year on positive x side and -1.0 m/year on negative x side, these two sides have the highest magnitude of the displacement.

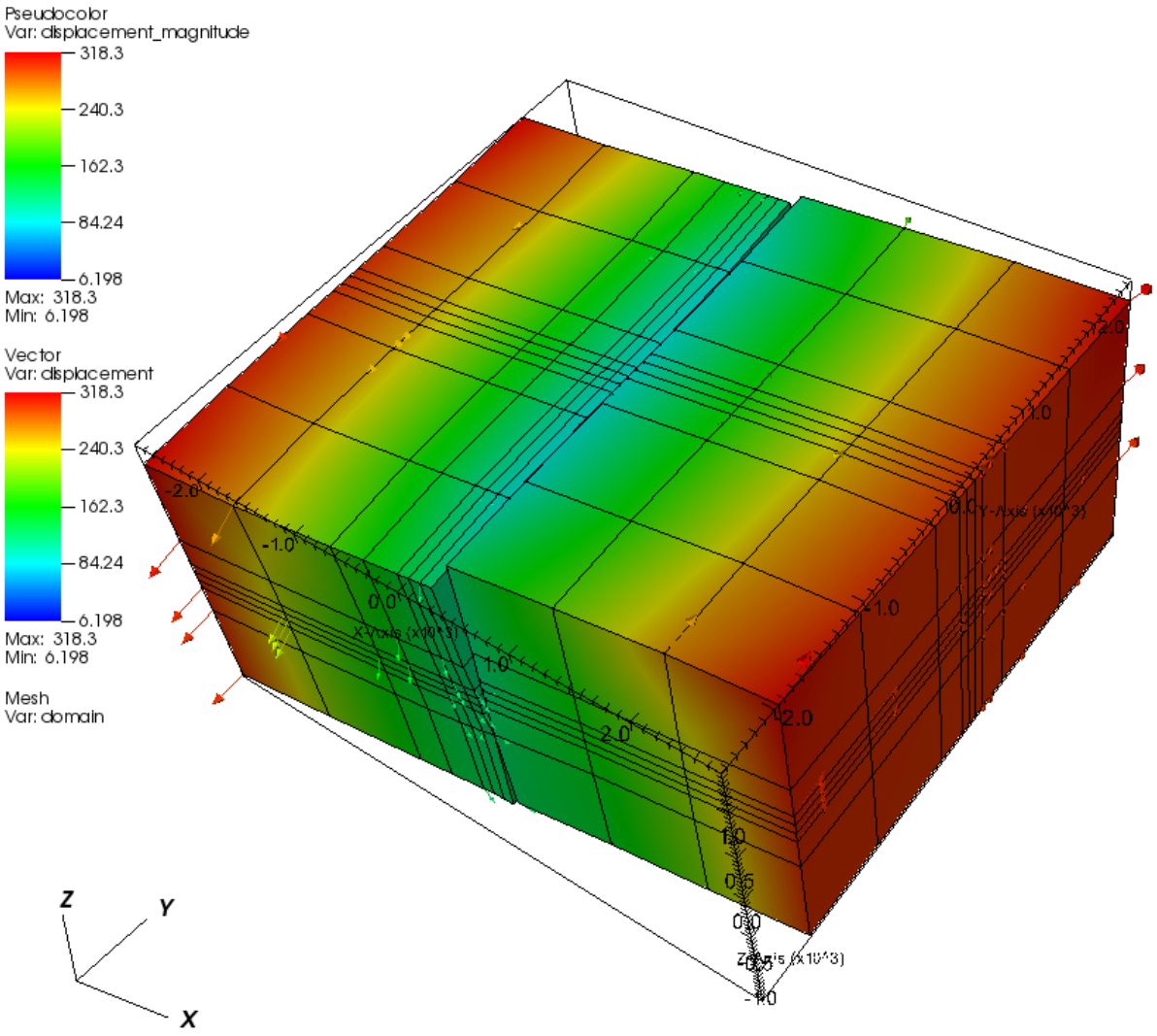

Figure 5.8 Displacement in the domain from gravity and far-field tectonic loading after 300.0 years and without injection

Since we run the simulation for 300 years with 1 m/year velocity on two sides, we would expect a total of 300 m displacement on either of the sides.

Figure 5.9 shows the displacement in the domain at the end of 300 years and with the injection of water. Maximum displacement is computed as 327 m while minimum displacement is calculated as 6.8 m. Maximum displacement in this case exceeds the maximum displacement in the dry case whereas the minimum displacements are comparable.

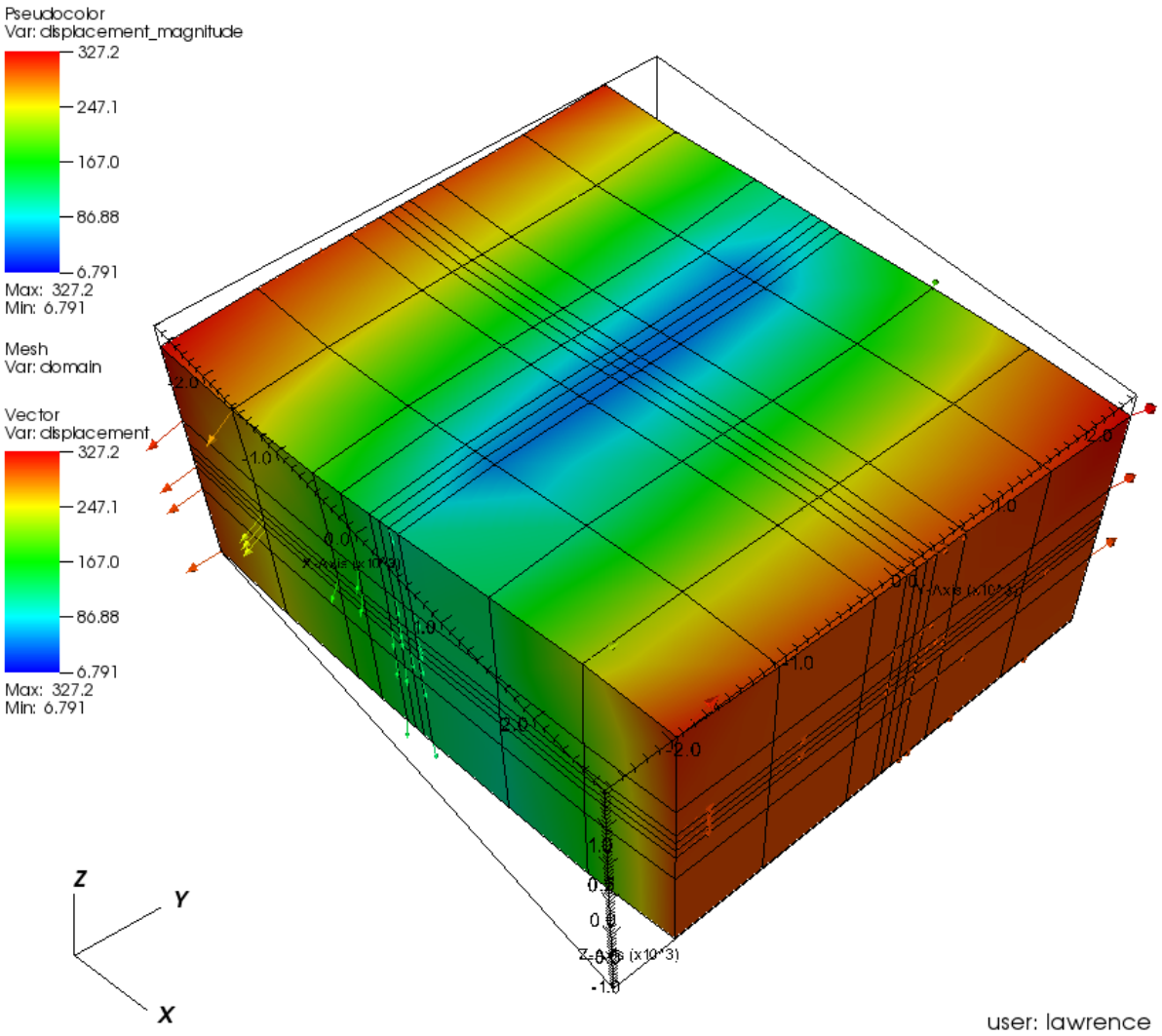

Figure 5.9 Displacement in the domain from gravity and far-field tectonic loading after 300.0 years and with injection

Figure 5.10 shows slips on the fault surface at the end of 300 years and without water injection. The fault is subject to far-field tectonic loading as well as gravitational stresses as stated earlier. Maximum slip magnitude is 182 m on the ground surface, although the slip initiated at about 900 m depth from the ground surface. Then the slip gradually propagates to the ground surface.

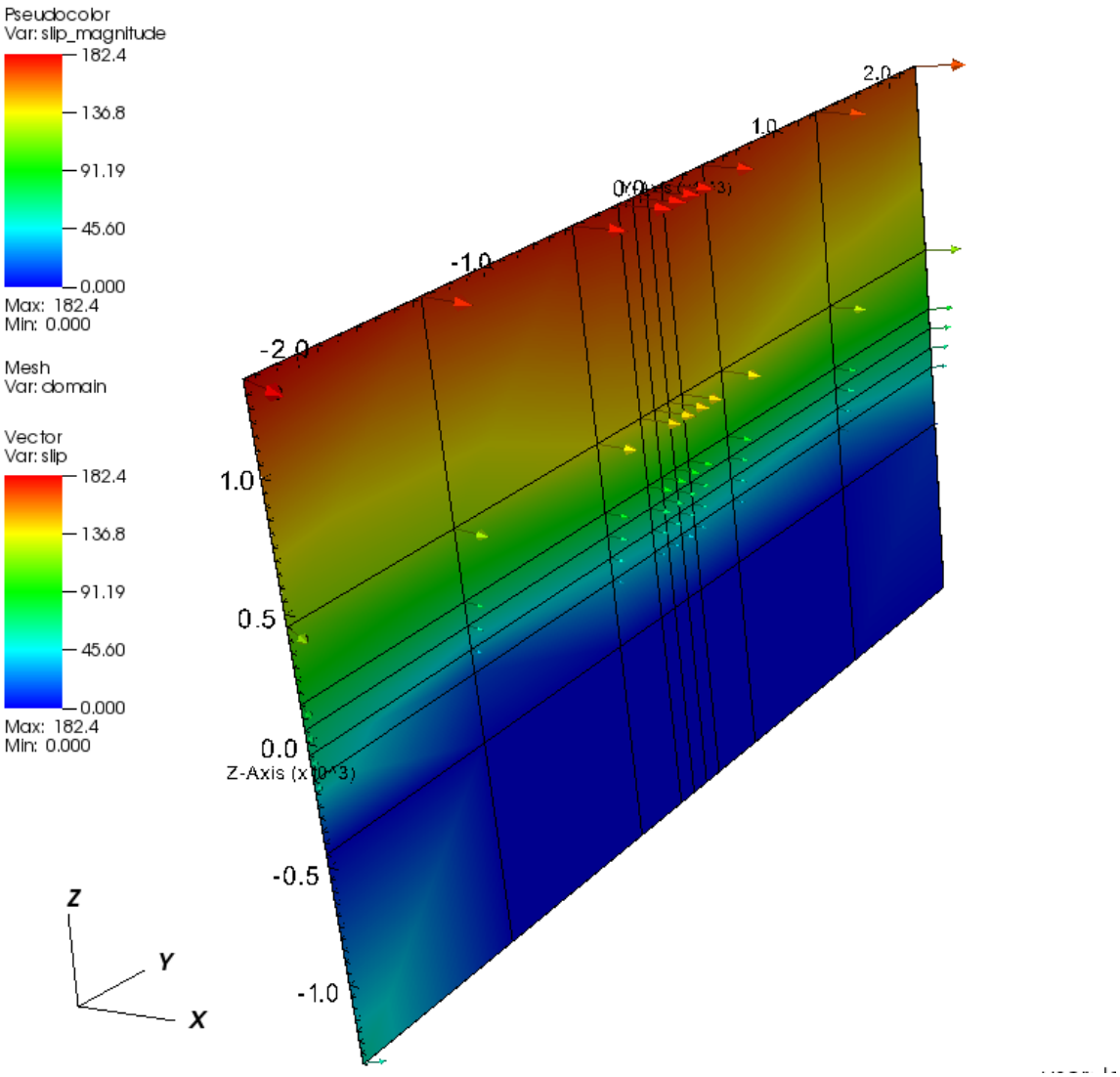

Figure 5.10 Slips on the fault after 300 years and without injection

Figure 5.11 shows slip on the fault surface with water injection and after the same time period. It shows a maximum slip of 27.5 m at a depth of 900 m from the ground surface.

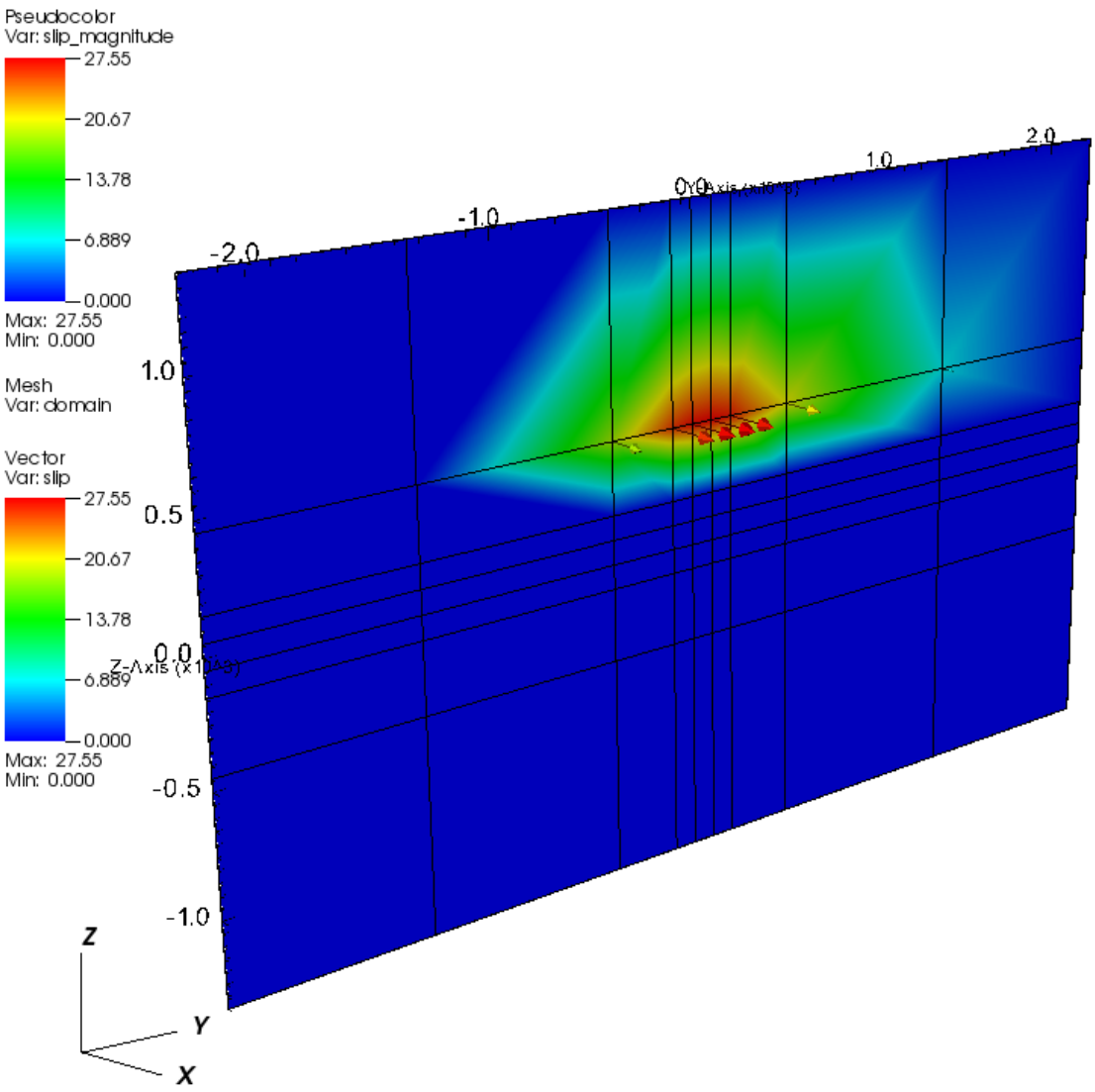

Figure 5.11 Slips on the fault after 300 years and with injection

The simulation results show that maximum slip in dry case (182 m) is higher than the maximum slip with injection. This is explained as follows: injection of fluid in the domain increases the total stresses as reflected in the stress outputs (See Figure 5.5 and Figure 5.7). The increase in total axial compressive stress increases fault normal compressive stresses on the fault. Consequently, there is a relatively higher locking of the fault surface in the injection case in

comparison with the dry case. But we use the same failure criteria using Mohr-Coulomb shear strength in both dry and injection case. Recalling equation 2.68 from Chapter II,

$$\tau = c + \mu\sigma_n^{'}$$

we see that shear strength τ is a function of effective normal stress $\sigma_n^{'}$ acting on the fault. Since the fault normal stress has increased (see Figure 5.13 for more details) in the injection case, shear strength of the fault has also increased according to this equation. This is why the fault shows a delayed response in simulating the slip nucleation in the injection case.

Figure 5.12 shows the tractions on the fault surface without injection after a period of 300 years. Maximum traction is about 125 MPa at the bottom of the domain and midway along the fault length. Minimum traction is about 12 MPa in the upper region of the fault surface. Fault traction shown in Figure 5.12 and Figure 5.13 are the resultants of three traction components acting on the fault surface. These are traction-shear-leftlateral, traction-shear-updip, and traction-normal. The first two are the shear traction acting along the fault surface and that determines the slip potential. The last component, traction-normal determines the shear strength of the fault by Mohr-Coulomb failure criteria. These three components respectively determine the leftlateral-slip, reverse-slip, and fault opening [see Figure 2.8 and 2.9 in Chapter 2]. After investigating the traction database, the maximum traction-normal is found to be as +69.1 MPa in this case.

Figure 5.13 shows traction on the fault surface with injection after a period of 300 years. Like before, maximum stress occurs near the bottom of the fault and in the midway of fault length. Maximum traction value in this case is calculated about 130.6 MPa and minimum is about 26.8 MPa. Comparing the dry case, it shows a traction increase of about 6 MPa. But the maximum traction-normal is computed of about 111.6 MPa compared to the dry case (+69.1

MPa). So, there is about a 40 MPa increase in fault normal traction due to injection of fluid. This increase results in locking the fault longer than the dry case, which shows earlier slip.

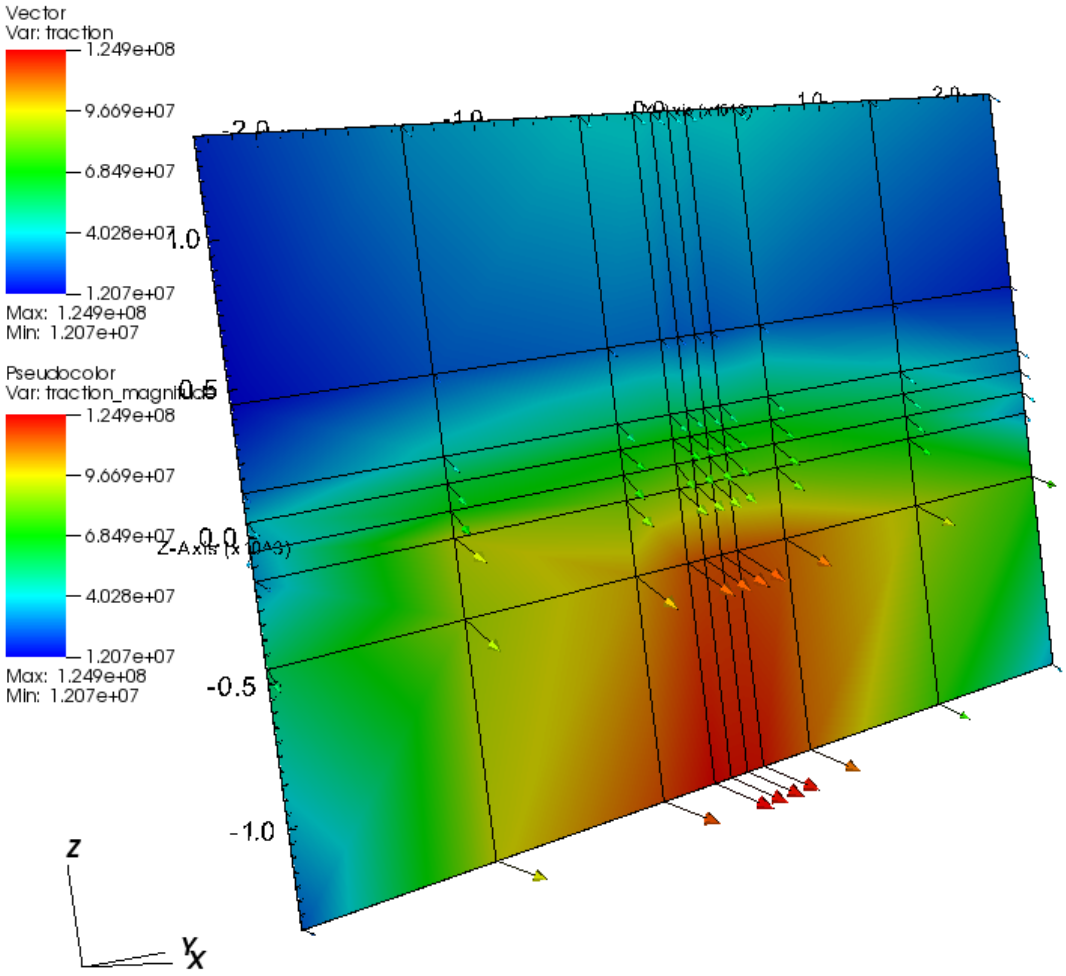

Figure 5.12 Traction on the fault surface after 300 years and without injection

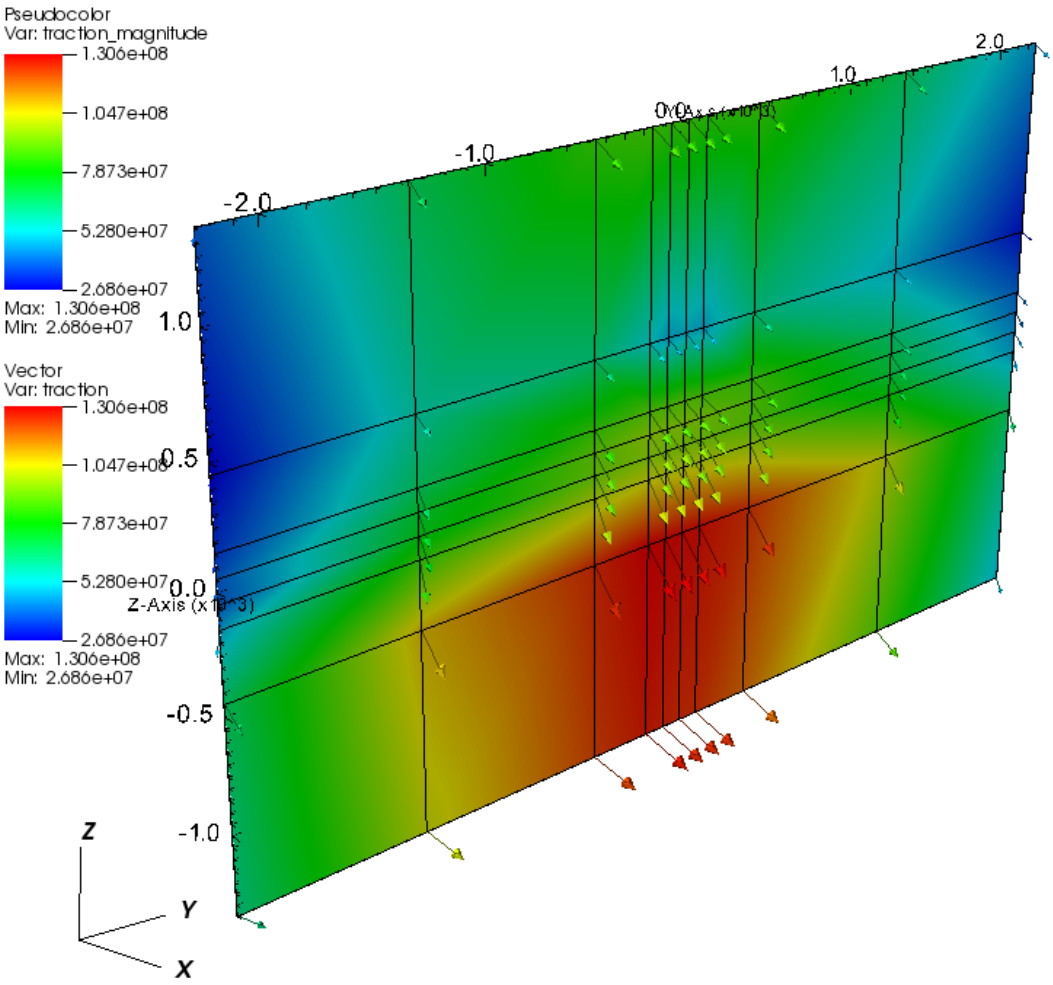

Figure 5.13 Traction on the fault surface after 300 years and with injection

CHAPTER VI

EARTHQUAKE DYNAMIC RUPTURE SIMULATION FROM FLUID INJECTION

6.1 Introduction

In the previous chapter, we demonstrated quasi-static induced earthquakes simulation resulting from hundreds of years of tectonic plate movements. From seismological point of view, those models could not explain the causes of variation of rupture behavior of individual earthquakes that may have been swamped by the large time steps coming from the fluid flow code. Under a dynamic rupture modeling scheme, following a specified failure criterion and initial and boundary conditions on the fault, the causes of rupture variation can be explained accurately [Okubo, 1989]. A dynamic model involves specification of a fault material constitutive relation that governs the material response to the applied loads and propagation of the resulting cracks over the failure surface. In this chapter, we simulate a single event dynamic rupture of a fault due to the presence of fluid pressure on the fault surface. This could essentially tell the experts the effect of fluid pressure on an earthquake event nucleation, and its dynamic rupture process due to the injection near a tectonic fault.

6.2 Issues in Simulating Dynamic Rupture from Fluid Injection

An earthquake dynamic rupture involves wave propagation through finite element cells. Running a dynamic problem with coupled TOUGH2-PyLith simulator poses a limitation due to two different time scale constraints of the two different multiphysics problems. The process of

fluid flow through porous and fractured media is very slow due to the low permeability of the subsurface rocks. It may take years for the fluid to propagate from the injection wells to the fault surface. On the other hand, for the dynamic rupture simulation it takes fraction of a second to nucleate a single event and propagate the resulting seismic waves through the rock domain. Since in the TOUGH-PyLith coupled simulator, time steps from the fluid flow code are passed to the geomechanics simulator, the very large time step required to capture the flow properties, exceeds far beyond the stable time step computed for the wave propagation. This causes an instability in the geomechanics code PyLith due to its time restriction in simulating dynamic rupture.

In order to solve this limitation of the coupled simulator, an alternative approach is used for the dynamic rupture of an earthquake. Since the entire dynamic rupture and wave propagation occurs within seconds, a geomechanics simulation for this problem is performed at first. Next, a standalone fluid flow simulation from injections is performed for 1 year. This gives rise to the fluid pressure on the fault surface by the end of that time period. These pressure outputs are then used to account for the tractions on the fault surface before running the geomechanics problem. Next, PyLith is run for the same time period like before except this time the tractions on the fault are different due to the pressure effect. Finally, the results from the first and second cases of the PyLith runs are compared to see the fluid pressure effect on the dynamic rupture of a fault.

Unlike the quasi-static earthquake simulation (Chapter V) where we used slip rate on the positive and negative x boundaries, in a dynamic rupture case we specify normal and shear tractions on the fault and let an earthquake nucleate and rupture governed by the rate- and state-dependent friction law. Also, in quasi-static case, we ran the simulations in the order of hundreds

of years whereas under a dynamic case we only run the simulation for few seconds. Because a single event dynamic rupture occurs within a fraction of a second which is not possible to observe while running a simulation for hundreds of years. By running a single event simulation we can then analyze how the slip nucleates, where it nucleates, and when it goes dynamic by investigating the wave propagation characteristics. Also, during quasi-static simulation we used Dirichlet boundary conditions on the sides of the domain. But in a dynamic rupture case we use absorbing boundary conditions on the sides of the domain. These kind of boundary conditions prevent the seismic waves from reflecting off of a boundary by placing dashpots on it. Both p-wave and s-wave normally incident to the boundaries are absorbed perfectly. But waves that are not normally incident are partially absorbed.

6.3 Description of the Problem

We use a domain size of 2 x 1.5 x 1 km as shown in Figure 6.1 to demonstrate the dynamic rupture simulation from a single event. We run a total of three different cases to show the effect of fluid pressure and injection well sensitivity to rupture simulation. The first run consists of pure dynamic rupture simulation without any presence of fluid. The second run consists of dynamic rupture simulation with an injection well located at 50 m away from the fault. The third case involves the sensitivity analysis of the fluid injection well to the traction perturbation and slip nucleation on the fault surface. In this case, we change the location of the well at a distance of 950 m away from the fault. We use water as the fluid. The fault is located at the midway along the X axis and parallel to the YZ plane. The fault cuts all the way from top to bottom and from one side to another (white portion in Figure) making it equal to the size of 1.5 x 1 km. We grid the entire domain with an element size of 100 x 100 x 100 m. Therefore, the

domain has a total of 3000 elements. We use rock density of 2670 kg/m^3, shear wave velocity 3464 m/s and p-wave velocity of 6000 m/s. For boundary conditions we use absorbing dampers on all the sides except the top surface (ground surface).

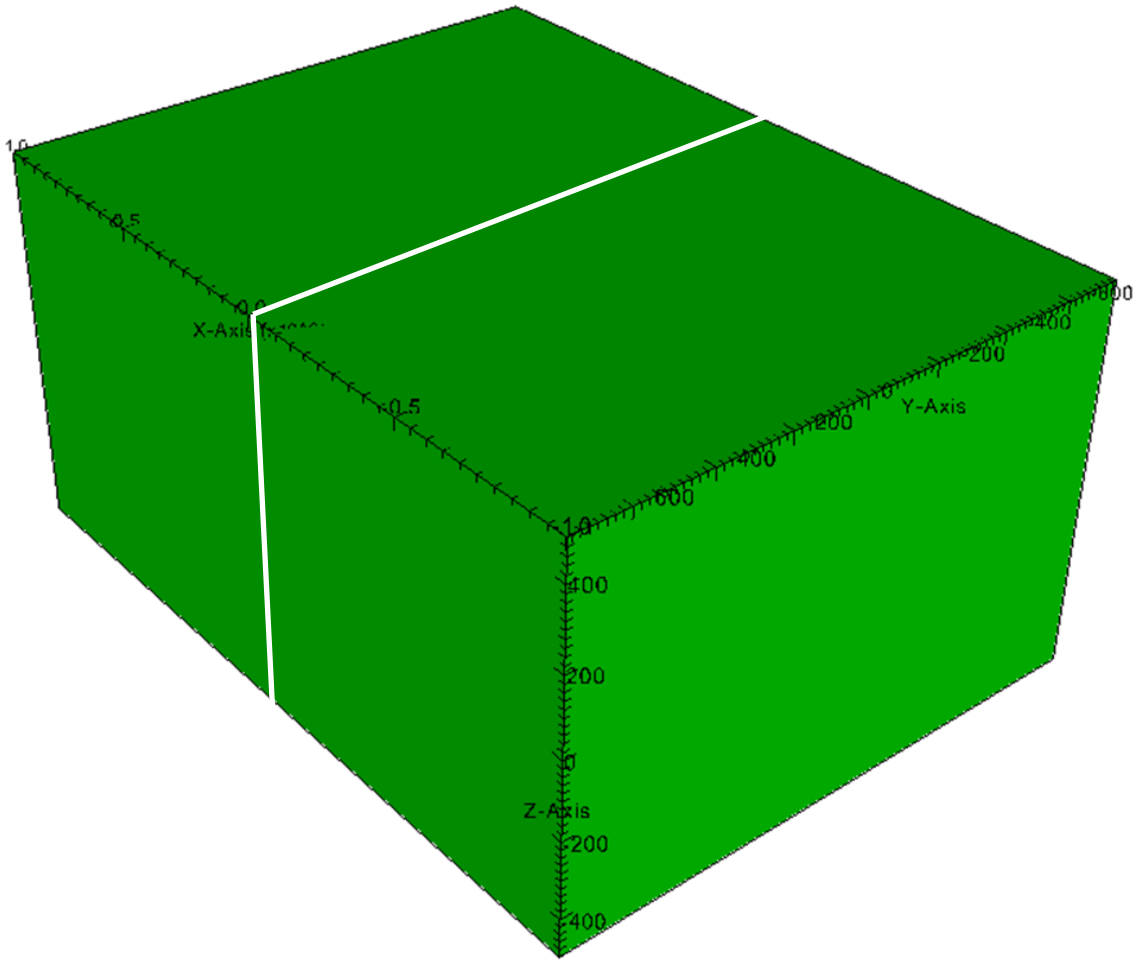

Figure 6.1 Domain geometry (2000 x 1500 x 1000 m) for a single event dynamic rupture simulation

Figure 6.2 shows that the fault is 1500 m long and 100 m wide. It also shows the location of the hypocenter for dynamic slip nucleation which is specified through parameter specification in the geomechanics code PyLith. The fault is also gridded with element size of 100 x 100 m

providing it a total of 150 elements. Tractions, slips, and pressures are calculated at the centers of these gridded cells.

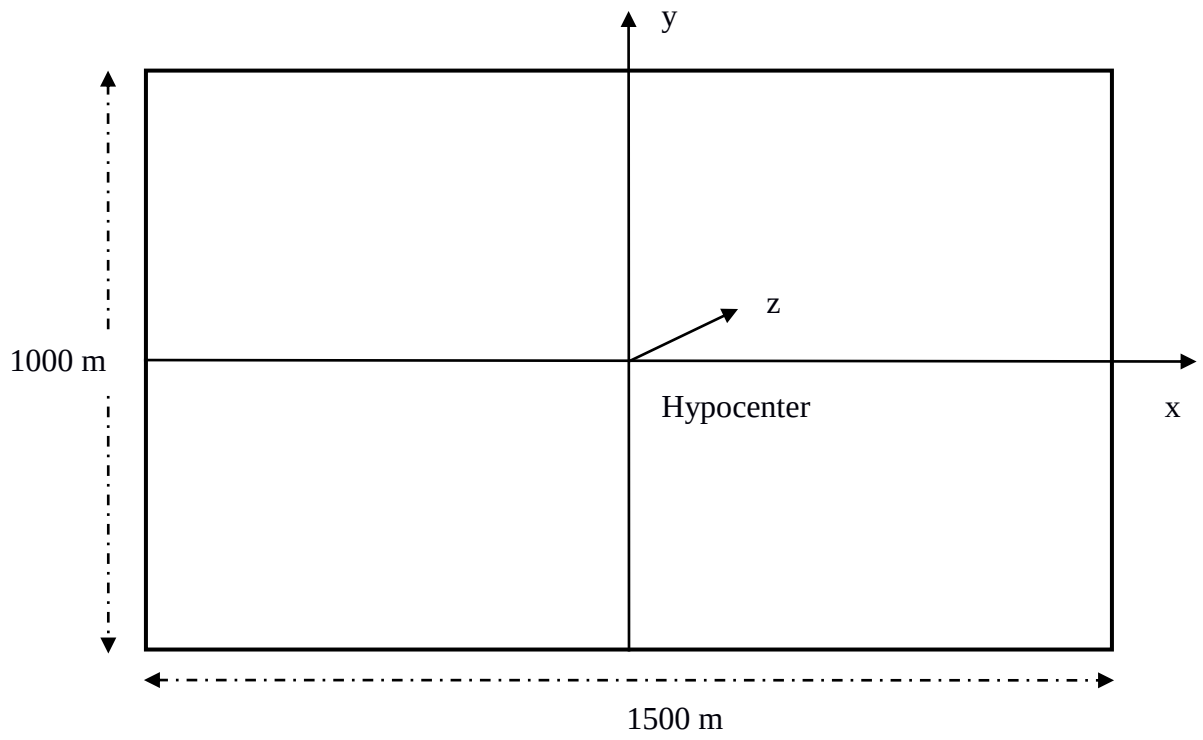

Figure 6.2 Dimension of the fault surface and prescribed location of the hypocenter

6.3.1 Dynamic parameter specification

We follow the earthquake dynamic rupture methodology as described by Aagaard et al (2013). We use rate- and state-dependent ageing friction law for the frictional strength development of the fault material. We impose initial left-lateral shear traction of 40 MPa and normal traction of 60 MPa on the fault surface. We also specify a spatial and temporal variation of a horizontal shear traction value in order to nucleate the rupture front. The particular form of rupture results from the smooth variation of tractions from zero to its maximum value $\Delta\tau_0 =$ 25 MPa over a finite time interval $T =$ 1s, and confined to a finite region $R = 500\ m$. We

specify the hypocenter to be located at a depth of 500 m from the ground surface. The traction perturbation is given by the following mathematical formula:

$$\Delta\tau = \Delta\tau_0 F(r) G(t)$$

Where $F(r)$ is used for spatial variation of the traction values and given by:

$$F(r) = \begin{cases} exp^{\left(\frac{r^2}{r^2 - R^2}\right)} & r < R \\ 0, \quad r \geq R \end{cases}$$

where R is used as 500 m in the current simulation and r represents the distances from the hypocenter to all the fault elements. $G(t)$ is used for the temporal variation of the traction and is given:

$$G(t) = \begin{cases} exp^{\left(\frac{(t-t_n)^2}{t(t-2t_n)}\right)}, & 0 < t \leq t_n \\ 1, & t > t_n \end{cases}$$

where $t_n = 1.0\ s$

These spatial and temporal variation of the traction values are specified via the spatial and time history databases in PyLith.

We run the dynamic rupture simulation for a total of 2 seconds and use a time step size of 0.005 second based on the wave period of 0.3 second. The output is requested at every 0.05 second. We use the following rate- and state parameters (Table 6.1):

Table 6.1 Specification of fault constitutive model using Dieterich-Ruina RSF parameters

Rate- and state parameters	**Values**
Reference friction coefficient	0.6
Reference slip rate	1.0E-06 m/s
Characteristic slip distance	0.02 m
Constitutive parameter a	0.016
Constitutive parameter b	0.012
Cohesion	0.0 MPa

6.3.2 Simulation results

With the boundary conditions and parameters specified above, we run the simulation for a total of 2 seconds and request output at every 0.05 second. Figure 6.3 shows the magnitude of the tractions on the fault surface. Since we specify initial normal and left-lateral tractions and there is no pressure perturbation near the fault surface, tractions perturbation only results from the specified functions discussed in section 6.3.1. Traction changes with time and space on the fault surface. At time 0.05 s, the traction magnitude is computed as 72 MPa on every point of the fault surface. We specify the traction change spatial database and time history database in such a way that perturbation occurs only in the bottom half of the fault. At time 1.0 s, traction perturbation results in the maximum magnitude of 88 MPa near the hypocenter of the fault surface. Traction magnitude diminishes from the hypocenter radially outward. The concentration of the higher magnitude of traction values at the center makes it susceptible to nucleate an earthquake event at that point. It is noticeable from the two plots that the color contours of the traction values do not change but the magnitude itself. These contour plots are in contrast to the ones perturbed by the fluid pressure which is shown and discussed afterward in the injection cases.

Figure 6.4 shows the slip nucleation on the fault surface with time. We see that there is no slip nucleation on the fault surface up until 0.6 s. That means until this time period, the shear traction on the fault surface does not exceed the frictional strength specified by the RSF friction parameters. At time 0.65 s, slip starts to nucleate at the hypocenter and at 1.0 s the maximum value of slip is computed as 1.55e-05 m, which is very small indicating that the rupture does not go dynamic. At the end of the simulation (at time = 2 s), the maximum computed slip is found to be 7e-05 m only. By investigating the slip characteristics, it is understood that this earthquake is

still in the nucleation phase and does not go dynamic within 2 seconds.

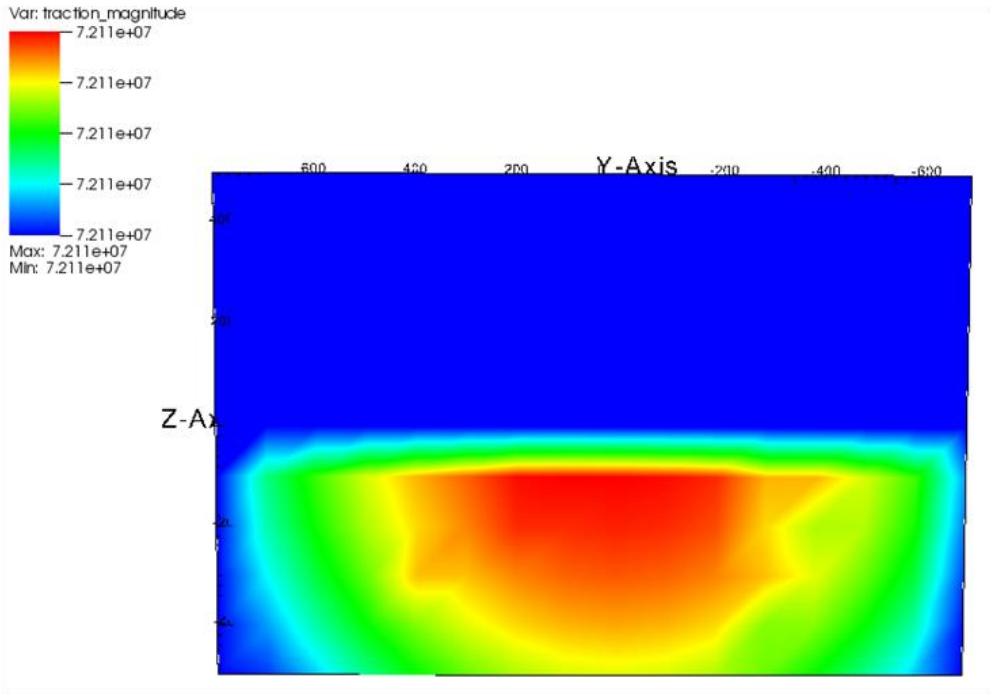

(a) Traction on the fault at time 0.05 s

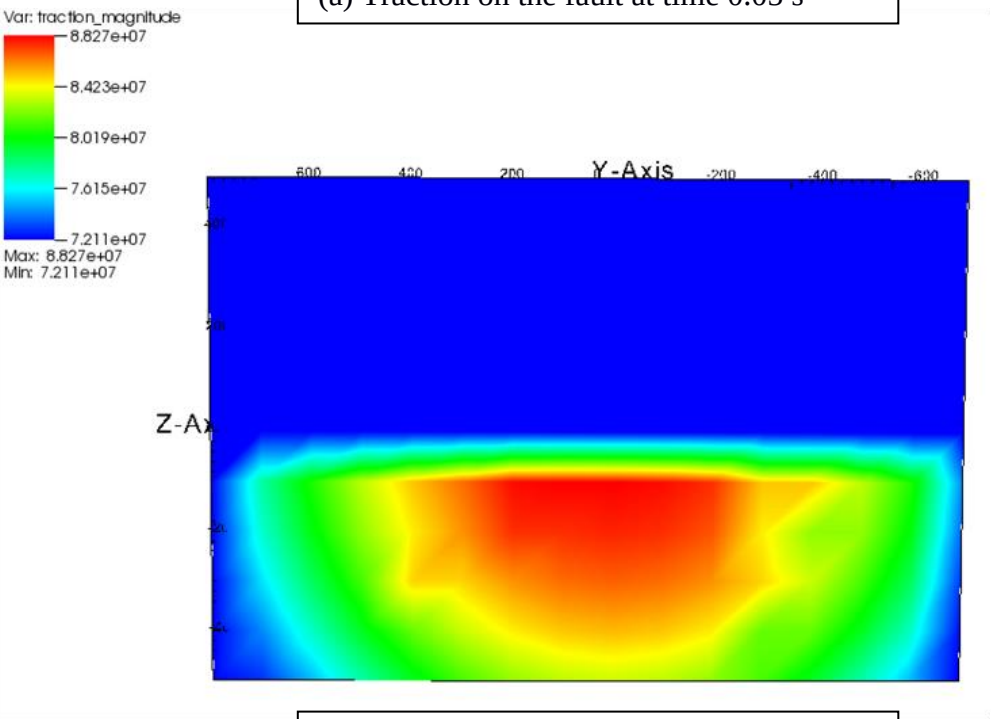

(a) Traction on the fault at time 1.0 s

Figure 6.3 Traction magnitudes on the fault surface without the presence of water

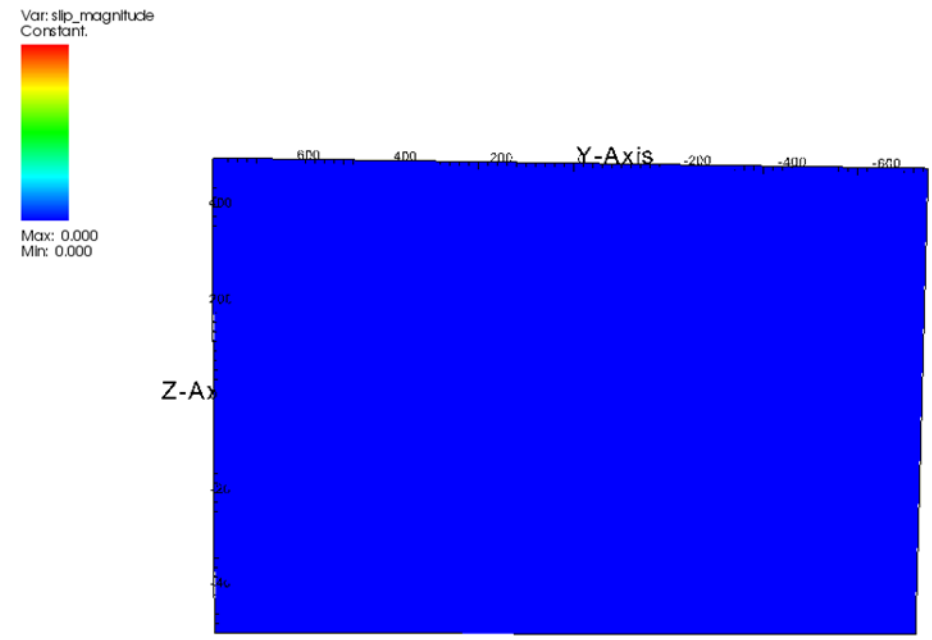

(a) No slip nucleation up until 0.60 s

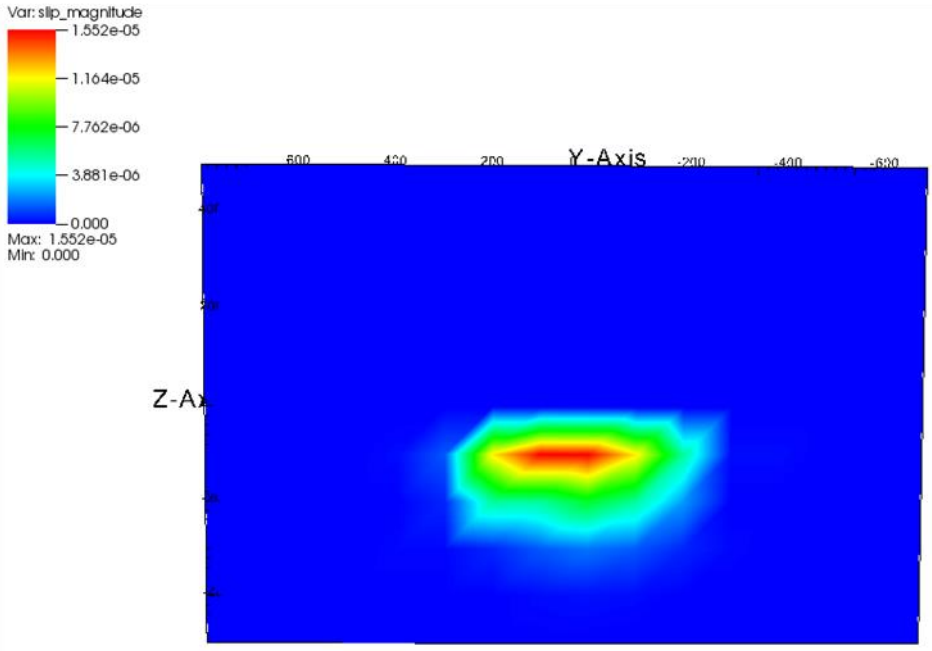

(b) Slip nucleation at time 1.0 s

Figure 6.4 Slip nucleation on the fault surface under no injection case

6.4 Earthquake Dynamic Rupture Simulation with Fluid Injection

In this section, we run the same simulation by including a typical water injection case in geothermal reservoirs. We consider a case where water is injected at the rate of 1 kg/s for 10 years at a depth of 450 m from the ground surface. The injection well is located 50 m away from the fault. Table 6.2 shows the relevant fluid flow parameters.

Table 6.2 Specification fluid flow parameters for dynamic rupture simulation

Flow parameters	**Values**
Fluid (water) density	1000 kg/m^3
Rock porosity	42.5 %
Rock permeability in all dir.	6.51E-17 m^2
Fault permeability in x dir.	6.51E-28 m^2
Fault permeability in y and z dir.	6.51E-15 m^2
Boundary conditions	No flow on all sides, free flow across the ground surface

The injection of the water causes the development of pore water pressure which propagates throughout the domain including the fault surface. We use a uniform rock permeability of 6.51E-17 m^2 throughout the domain. We use a very low permeability (6.51E-28 m^2) across the fault core that may represent a mature fault thereby not allowing water to pass from one side to another through the fault. But we use a very high permeability (6.51E-15 m^2) along the width and depth of the fault which may represent a very highly fractured fault zone. Figure 5 shows the pore water pressure distribution on the fault surface due to injection for 10 years. It shows a symmetric pressure distribution relative to the element where water is injected. The distribution shows a maximum of 22 MPa of pressure development due to that high injection and for a period of 10 years. The symmetry makes sense due to the uniform rock permeability. However, the plot does not include the hydrostatic pressure from saturated ground condition; it shows pressure

from injection only.

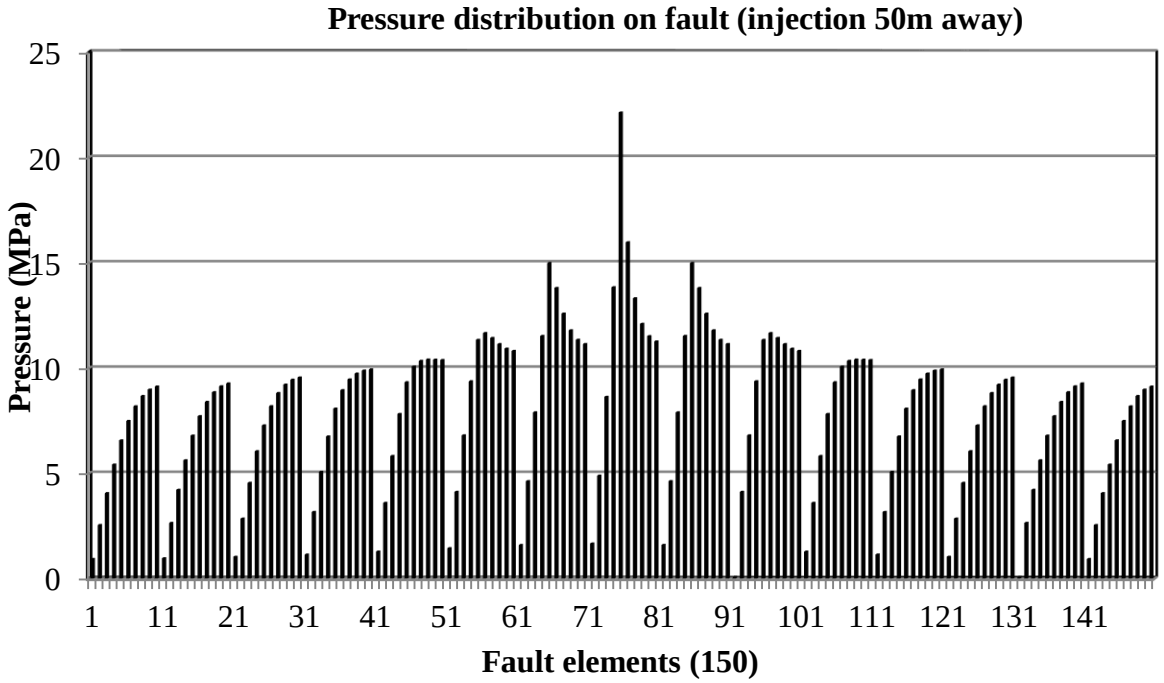

Figure 6.5 Pore water pressure distribution on the fault surface after 10 years of injection

These pressures are used to directly account for the fault normal tractions before running the injection cases. Because fluid pressure does not affect the shear tractions on a body. There is a total of 150 elements in the fault, starting from 1 (near ground surface) through 10 (fault bottom) in the first column. The second column consists of elements 11 through 20 and so forth until the last element is 150.

6.4.1 Simulation results

Figure 6.6 shows traction perturbation on the fault surface due to the presence of pore water pressure. Near the mid-central region, the blue area shows reduced traction values resulting from the high pore water pressure development near the injection well. Regions which are away from the injection well and located near the bottom show higher magnitudes of traction.

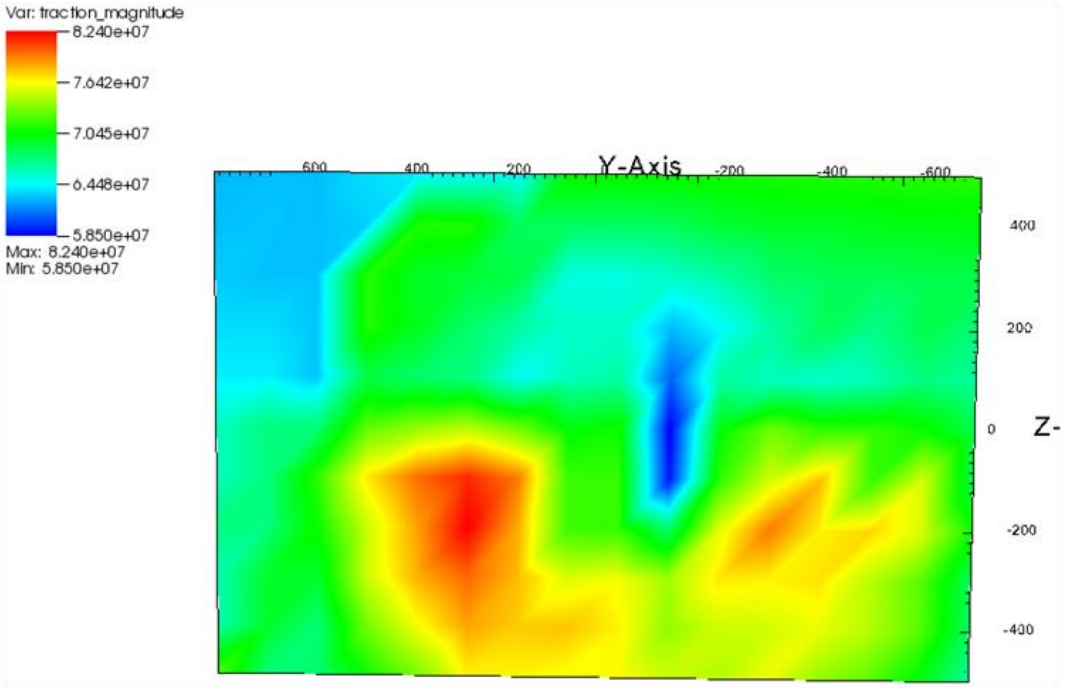

(a) Traction on the fault at time 0.05 s

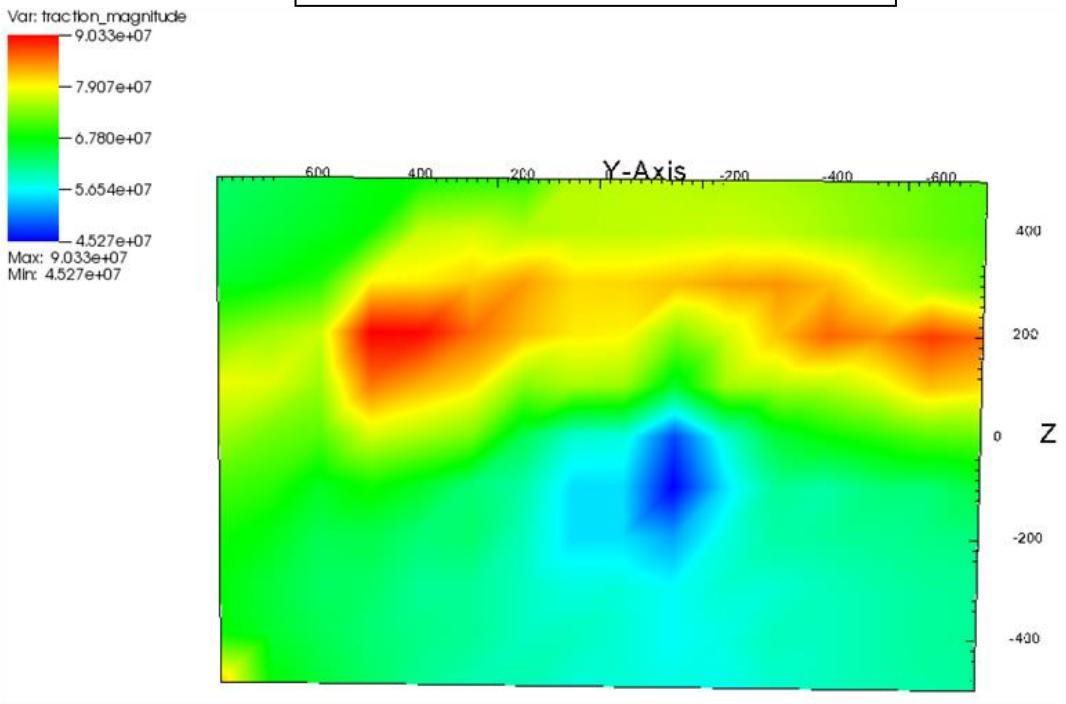

(a) Traction on the fault at time 1.0 s

Figure 6.6 Traction perturbation on the fault surface from an injection 50 m away

Figure 6.7 shows the slip distribution on the fault surface in the presence of pore water pressure.

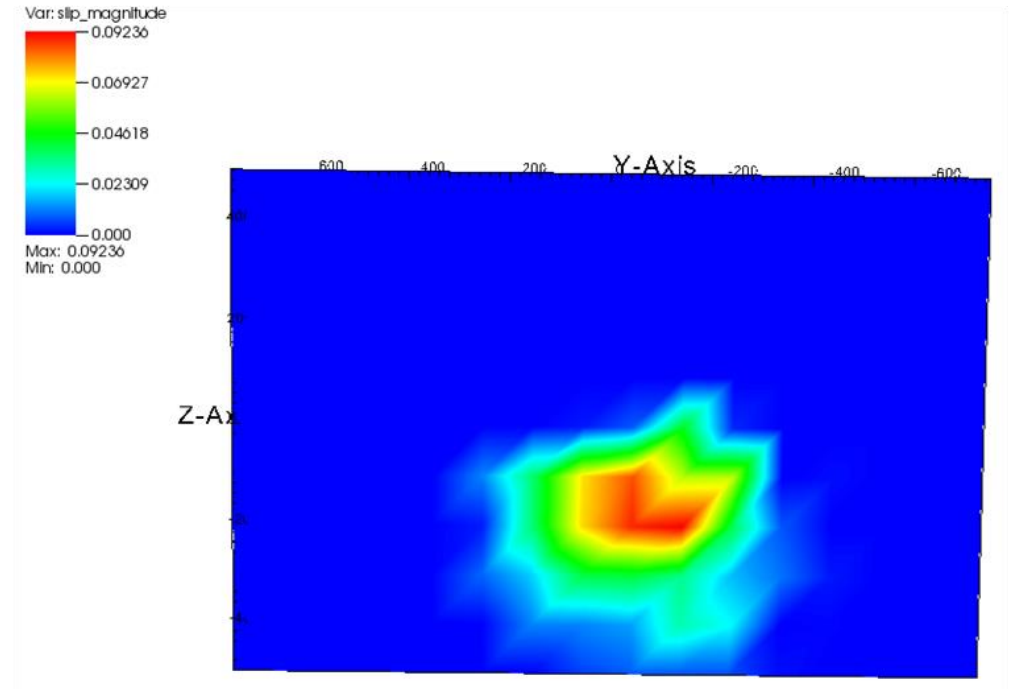

(a) Slip distribution at time 0.05 s

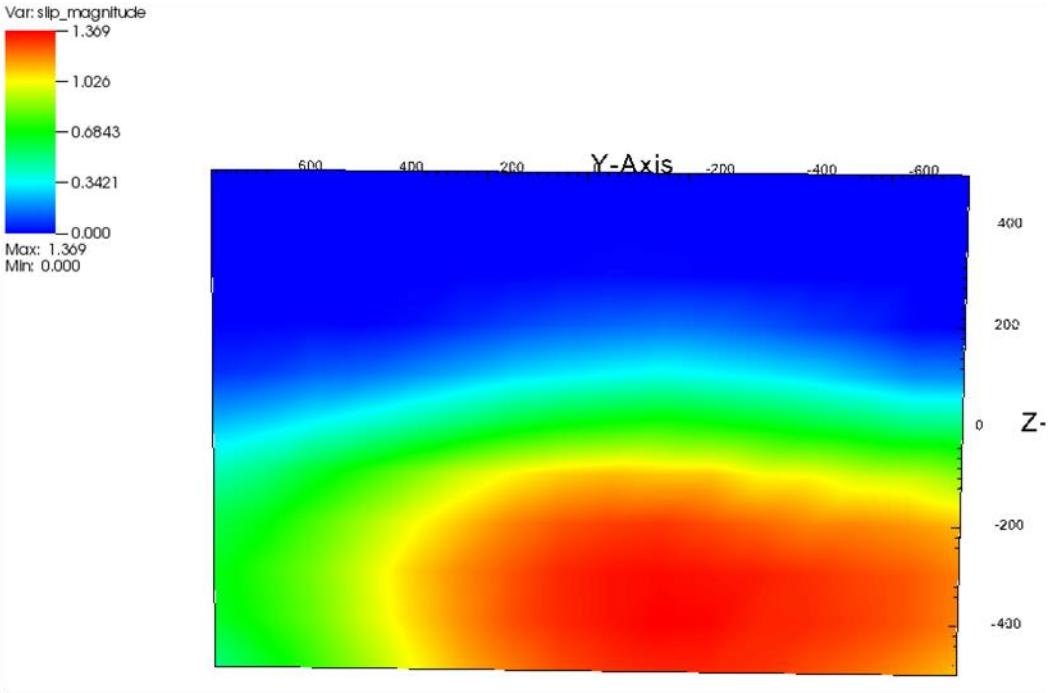

(a) Slip distribution at time 0.65 s

Figure 6.7 Slip nucleation and dynamic rupture propagation from an injection 50 m away

Comparing to the no injection case, we see a significant amount slip results in after 0.05 second of the simulation under the water injection case. This increase in slip can be attributed to reduction of traction values near the central region of the fault which implicates the unlocking of the fault. At time 0.65 second, maximum slip is seen as 0.75m which is still slipping. We have created a movie file of the whole dynamic rupture process and slip continuation for the entire period of simulation.

6.5 Sensitivity of Fluid Injection to Slip Nucleation

We perform a sensitivity analysis in order to show the effect of the injection well location to the slip nucleation time while keeping all other parameters identical. We now inject at the same rate and at the same depth but at a distance of 950 m (instead of 50 m) away from the fault. Figure 6.8 shows the pore water pressure distribution in this case.

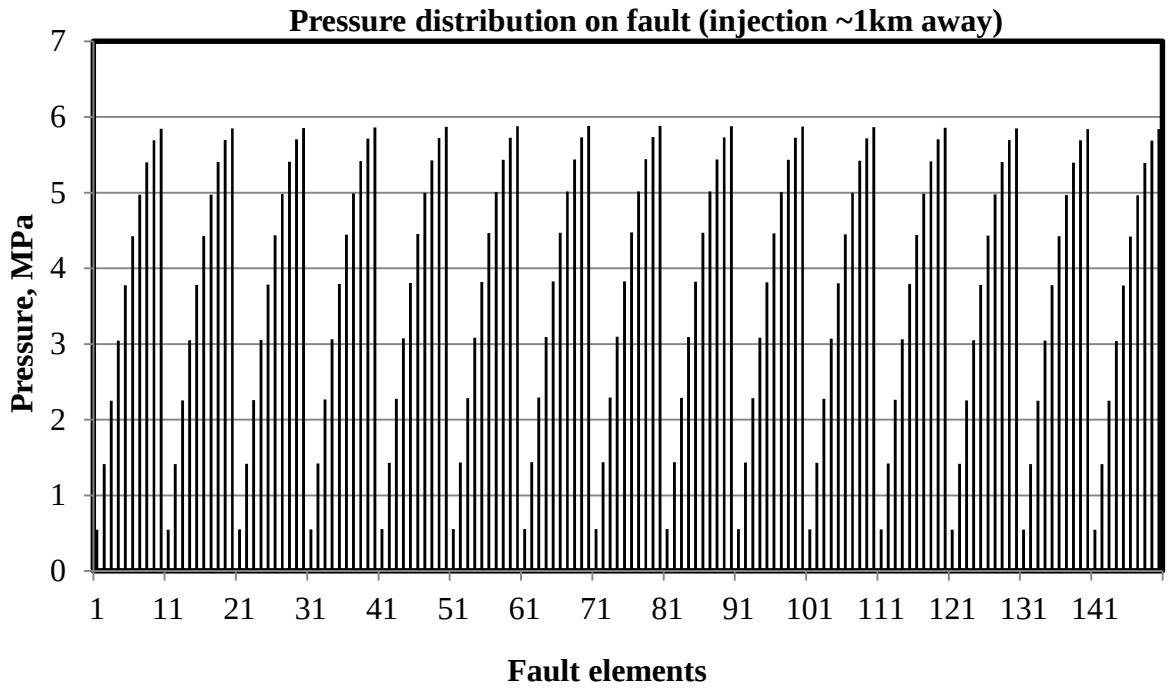

Figure 6.8 Pore water pressure distribution on the fault surface after 10 years of injection

It is interesting to see the difference of pore water pressure distribution in two cases. The distribution shows a uniform hydrostatic pressure throughout the domain. This can be explained as follows. Since the injection well is located far away from the fault, in this case, and rock permeability is sufficiently low, it takes a long time for water to permeate through the rock pores and reach to the fault surface. By the time it reaches to the fault surface, water already propagates to all other boundary surfaces which do not allow the water to pass through. This results in the monotonic increase of the water pressure due to the accumulation of the water volume. The excess water flows out through the ground surface. This is in contrast to the first case where water is injected near the fault. Pressure under that circumstance immediately rises to 22 MPa which is very high compared to the neighboring elements. This is because water at that time is still propagating to the surrounding elements and not reached to the boundary surfaces.

6.5.1 Simulation results

Figure 6.9 shows the distribution of traction perturbation on the fault surface due to the injection well located about a kilometer away. Like before, we observe the traction values at times 0.05 s and 1.0 s in order to compare the results and explain the sensitivity. The maximum traction values, in this case, exceed the maximum values we computed in the first case. This is because of the lower pore water pressure development on the fault surface resulting in relatively higher fault normal traction values.

Figure 6.10 shows the slip nucleation and distribution due to water injection occurring at a distance of 950 m away from the fault. Comparing the slip magnitudes with the case 1, we see that slip is lower in this case. The maximum value of slip was 1.37 m when the injection well is very close to the fault surface whereas in this case we obtain only 0.74 m. Both simulations show

a dynamic slip distribution since slip increases at a rapid rate after the critical slip distance.

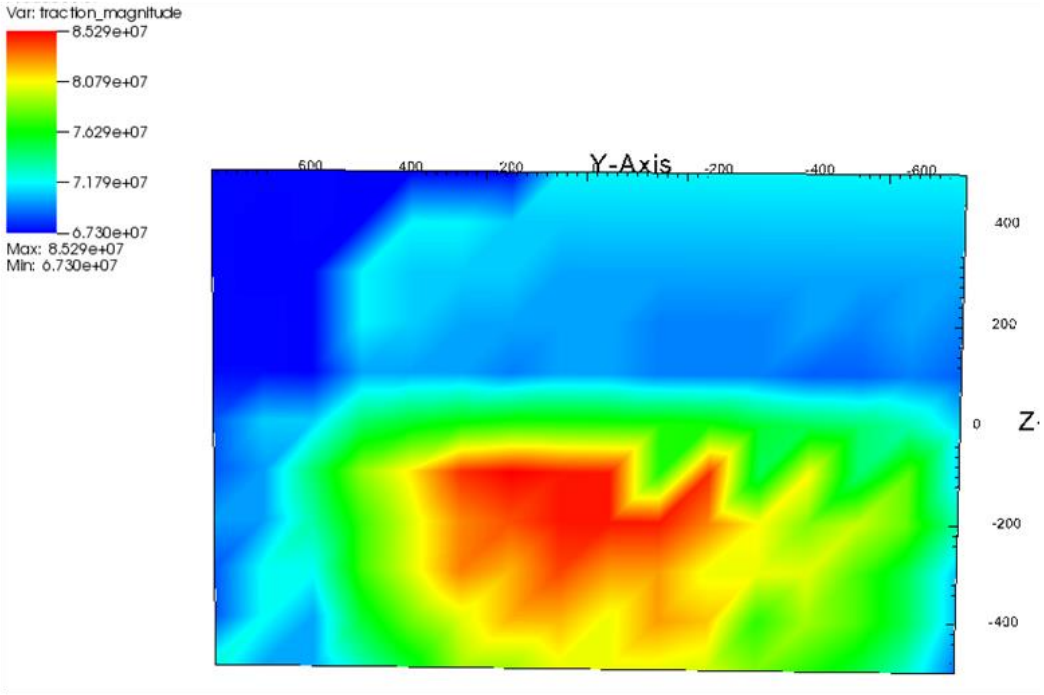

(a) Traction on the fault at time 0.05 s

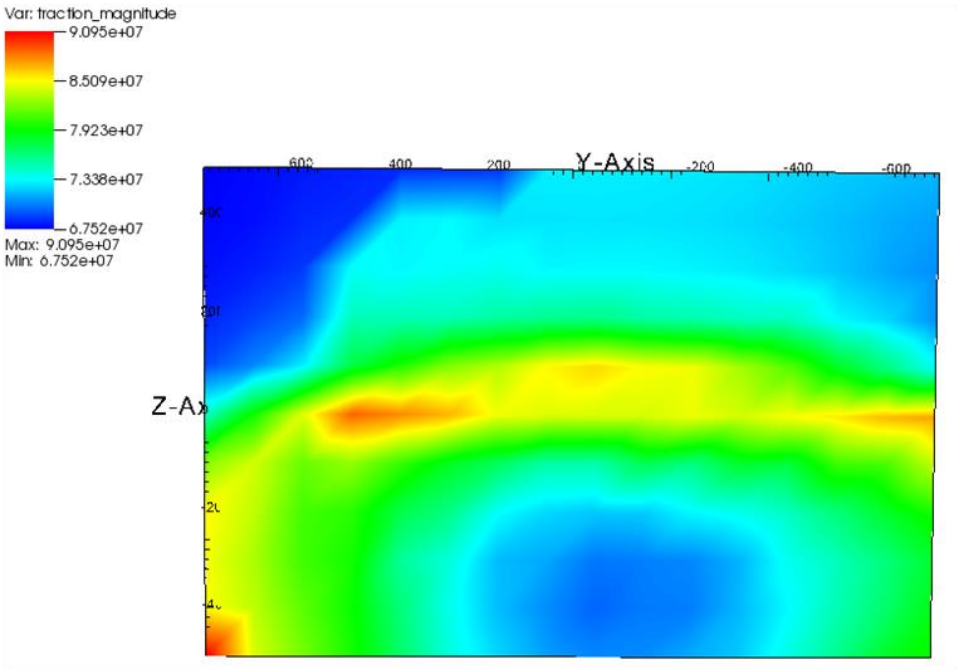

(a) Traction on the fault at time 1.0 s

Figure 6.9 Traction perturbation on the fault surface from an injection 950 m away

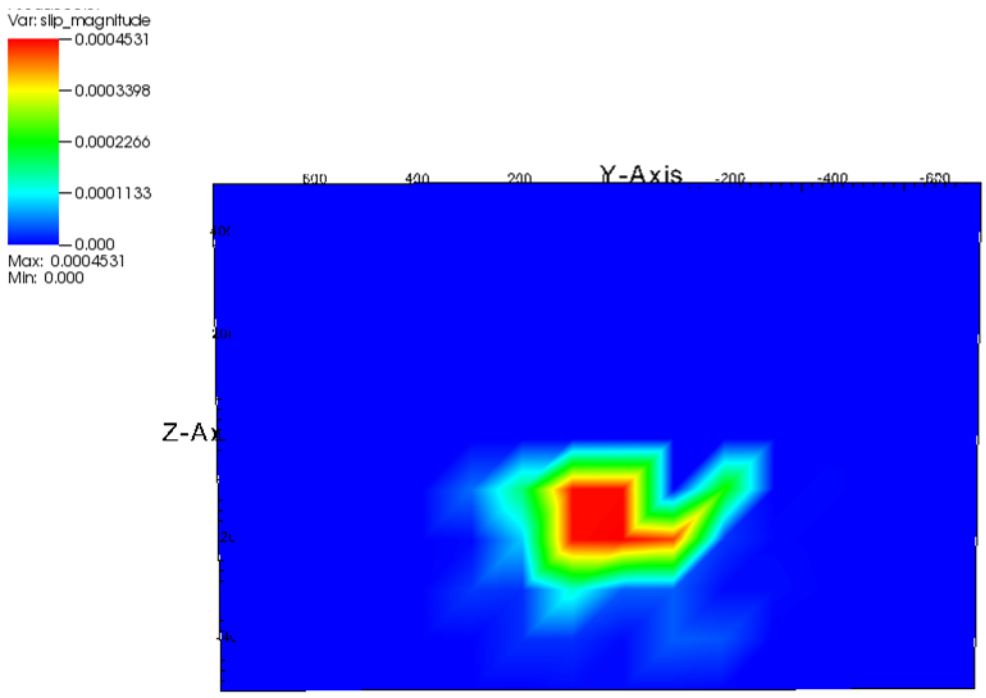

(a) Slip distribution at time 0.05 s

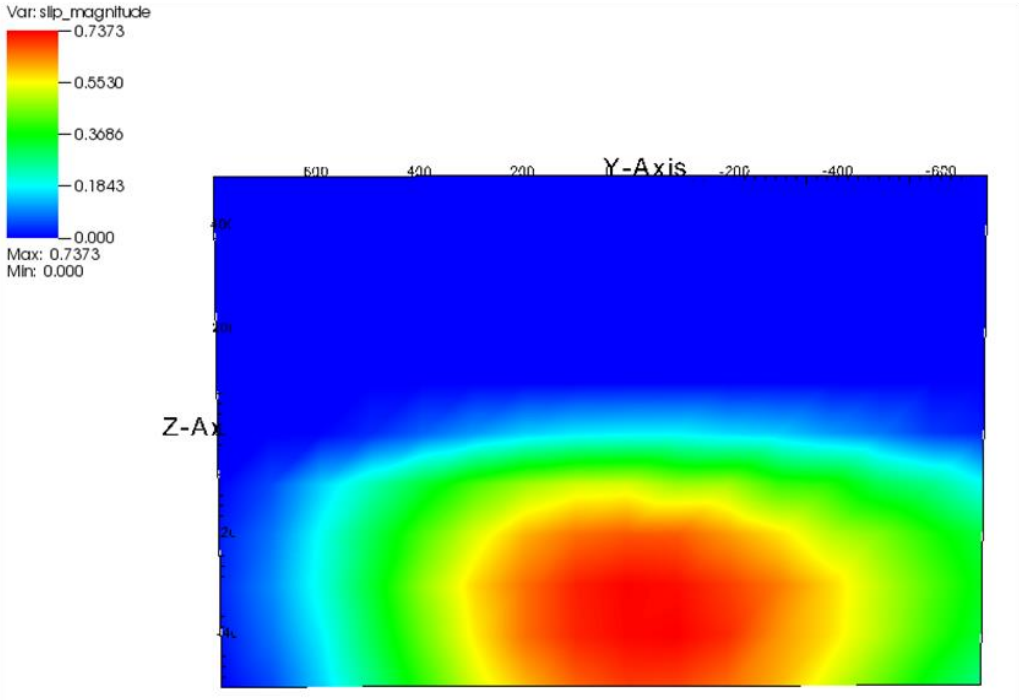

(a) Slip distribution at time 1.0 s

Figure 6.10 Slip nucleation and dynamic rupture propagation from an injection 950 m away

In this chapter, we have performed three simulations for a single event earthquake dynamic rupture with and without water injection to demonstrate the effect of pore water pressure on the fault tractions and slips. We have considered the in situ condition as saturated with water before starting the simulations. Therefore, the pore water pressures accounted in the fault normal tractions result from the water injections alone; no hydrostatic pressure is considered. The pressure plots show the pressures that develop from the fluid injections only. Indeed, this could be the case in real situations where the fault is already saturated with water. The results clearly demonstrate the positive effect of water pressures on the slip nucleation time and subsequent rupture propagation of an earthquake event. The sensitivity analysis demonstrates that the injection location plays a critical role on the earthquake nucleation time and rupture propagation as well. With distance increased from 50 m to 950 m, while keeping the same injection rate for a period of 10 years, we see the slip value decreasing from 1.37 m to 0.74 m.

CHAPTER VII

SUMMARY, CONCLUSIONS, AND FUTURE WORK

In this dissertation, a sequential coupled simulator is developed that can simulate the coupled interaction between multiphase fluid flow and geomechanics. For one-way coupling and testing the accuracy, it is validated with Terzaghi's 1D consolidation problem. The code is benchmarked with the analytical solution of Mandel's problem for coupled poroelasticity.

The TOUGH-PyLith coupled simulator is used to simulate quasi-static earthquake slips for a 3D rock model with a reservoir and a 2D planar vertical fault interface. Two cases are run in order to compare the influence of water pressure on tractions and slips on the fault. The injection case shows a delayed response in nucleating slips which may partly result from the increase of total stress inside the reservoir. Also, in running the quasi-static simulations we do not account for pore water pressure along the fault plane. All these issues are addressed in the earthquake dynamic rupture simulations in the previous chapter.

The previous chapter deals with the simulations of a single event earthquake dynamic rupture problem. We demonstrate the sequential execution of TOUGH-PyLith coupled simulator in benchmarking with Mandel's problem and modeling quasi-static simulations. However, for dynamic rupture simulation, we encounter a problem in time stepping of two different multiphysics problems in two different codes. An earthquake dynamic rupture occurs within a fraction of a second whereas fluid pressure diffuses very slowly due to the low permeability and porosity of subsurface rock strata. Since we pass each converged time step from the flow code to

the geomechanics code, a very large time (~years) coming from TOUGH causes instability in PyLith dynamic rupture simulation. We resolve that issue by running TOUGH and PyLith separately and using the pressure output to account for fluid pressure along the fault. We compute the pressures on the fault and effective fault normal tractions due to injection. Next, we run an injection that clearly showed an early nucleation of slip and rupture propagation compared to no injection case. We also perform a sensitivity analysis by placing the injection well about a km farther away from the fault. The results from the sensitivity analysis shows that increasing injection distance from the fault results in delayed nucleation of the slips on fault and subsequent dynamic rupture propagation.

The code currently uses an isotropic elastic material constitutive model to demonstrate the application problem. However, fault rupture and seismic slips are usually associated with plastic deformation of the rock material. This necessitates using more appropriate elastoplastic material models for an earthquake simulation. PyLith has some other material constitutive models such as Drucker-Prager elastoplastic and Maxwell viscoelastic constitutive models. Although not used in the current application, Drucker-Prager constitutive model in PyLith is modified and incorporated in TOUGH-PyLith to account for pore pressure and its effect on material deformation.

The current simulator does not include the effect of multiphase fluid flow and thermo-poroelasticity that may arise from changes in temperature, saturations, and the pore volume of the porous and fractured rock in an actual reservoir. However, TOUGH2 has already the capability of modeling multiphase, multicomponent, and nonisothermal fluid flow. But the geomechanics code PyLith is developed for crustal deformation from tectonic loading without considering fluid pressure and temperature. A constitutive model that accounts for the

temperature can be added to PyLith Pyre framework as needed. The temperature effect will take care of the thermal expansion or shrink of the rock volumes as well multiphase fluid components that may be more appropriate in geothermal reservoirs.

In developing the TOUGH-PyLith computational code, two different grids are created separately and mapped by matching their coordinates with a Fortran script. However, the code currently contains the mapping capability for hexahedral elements only. Additional modification is necessary to further include the more generic mapping scheme between the two codes. Time stepping in the TOUGH-PyLith coupled simulator is governed by TOUGH2 since this is run first for a particular time step after which it commands PyLith to run for the same time period. PyLith then breaks up that time period to reach convergence. However, a time step that converges TOUGH2 may not guarantee the convergence of the PyLith within the current implementation of the code. This is because of the two different characteristic time scales for two different multiphysics problem. Furthermore, each code uses their own linear and nonlinear solvers which are used sequentially but independently. These solvers have their own preconditioners for solving large matrices that involve computation of Jacobian.

We intend to use TOUGH-PyLith coupled simulator as a fully dynamic benchmarking code against an approximate but fast-running code RSQSim, [Richards-Dinger and Dieterich, 2012] which is more efficient for induced seismicity catalog simulations.

BIBLIOGRAPHY

Aagaard, B., S. Kientz, M. Knepley, L. Strand, and C. Williams [2013], PyLith User Manual, Version 2.0.0. Davis, CA: Computational Infrastructure of Geodynamics.

Abousleiman, Y., A. H.-D. Cheng, L. Cui, E. Detournay, and J.-C. Roegiers. [1996]. Mandel's problem revisited, Geotechnique, 46, 187–195.

Armero, F. and Simo, J.C. [1992]. A new unconditionally stable fractional step method for non-linear coupled thermo mechanical problems. Int J Numer Methods Eng 35: 737–766.

Asanuma, H., Soma, N., Kaieda, H., Kumano, Y., Izumi, T., Tezuka, K., Niitsuma, H.,Wyborn, D., 2005a. Microseismic monitoring of hydraulic stimulation at the Australian HDR project in Cooper Basin. In: Proceedings of the World Geothermal Congress 2005, Antalya,Turkey,Paper1615,5pp

Aziz, K., and A. Settari [1979], Petroleum Reservoir Simulation, Elsevier, London.

Bachmann, C. [2011]. Statistical analysis of the induced Basel 2006 earthquake sequence: introducing a probability-based monitoring approach for Enhanced Geothermal Systems. Geophysical Journal International, Vol. 186, Issue 2, Oxford University Press.

Baisch, S., Vörös, R., Rothert, E., Stang, H., Jung, R., Schellschmidt, R. [2010]. A numerical model for fluid injection induced seismicity at Soultz-sous-Forêts. International Journal of Rock Mechanics and Mining Sciences Volume 47, Issue 3, April 2010, Pages 405–413

Balay, S., W. D. Gropp, L. C. McInnes, and B. F. Smith [1997]. Efficient management of parallelism in object-oriented numerical software libraries, in Modern Software Tools in Scientific Computing, pp. 163–202, Birkhauser Press.

Barenblatt, G.I. Zheltov, I.P. Kochina, I.N. [1960]. Basic concepts in the theory of seepage of homogeneous liquids in fissured rocks [strata], Prikl. Mat. Mekh. 24 852–864, J. Appl. Math. Mech. 24 [1960] 1286–1303

Baria, R., Michelet, S., Baumgaartner, J., Dyer, B., Gerard, A., Nicholls, J., Hettkamp, T., Teza, D., Soma, N., Asanuma, H., 2004. Microseismic monitoring of the world's largest potential HDR reservoir. In: Proceedings of 29thWorkshop on Geothermal Reservoir Engineering, Stanford University, Stanford, CA, USA, pp. 194–201.

Batra, R., Albright, J.N., Bradley, C. [1984]. Downhole seismic monitoring of an acid treatment in the Beowawe geothermal field. Geotherm. Resour. Counc. Trans. 8, 479–483.

Bear, J., Corapcioglu, M.Y., A mathematical model for consolidation in a thermoelastic aquifer due to hot water injection of pumping. Water Resour Res, 17 [1981], pp. 723–736

Béatrice Ledéserta, Ronan Heberta, Albert Genterb, Danièle Bartierc, Norbert Clauerd, Céline Gralla. [2010]. Fractures, hydrothermal alterations and permeability in the Soultz Enhanced Geothermal System

Beer, G. [1985], An isoparametric joint/interface element for finite element analysis, Int. J. Numer. Meth. Eng., 21, 585–600.

Biot, M. A. [1941]. General theory of three-dimensional consolidation, J. Appl. Phys., 12, 155–164.

Boley,B. A. and Weiner, J. H. [1960]. Theory of Thermal Stresses. John Wiley, New York.

Byerlee, J.D. [1978]. Friction of Rocks, Pure Appl. Geophys, 116 615-626.

Bowker, K.A. [2007]. "Barnett Shale Gas Production, Fort Worth Basin, Issues and Discussion," AAPG bulletin, 91, p522-533.Byerlee, J.D. [1978]. Friction of rocks. Pure Appl. Geophys.116, 615–626

Caine, J.S., Evans, J.P., Foster, C.G. [1996]. Fault zone architecture and permeability structures. Geology24[11], 1025–1028

Cao, H. [2002]. Development of techniques for general purpose simulators, Ph.D. thesis, Stanford University.

Cappa, F., Guglielmi, Y., Virieux, J. [2007]. Stress and fluid transfer in a fault zone due to overpressures in the seismogenic crust. Geophys. Res. Lett. 34, L05301, doi:10.1029/2006GL028980.

Cappa, F. [2009]. Modelling fluid transfer and slip in a fault zone when integrating heterogeneous hydromechanical characteristics in its internal structure. Geophys. J. Int. 178, 1357–1362, doi:10.1111/j.1365-246X.2009.04291.x.

Cappa, F., and J. Rutqvist. [2011]. Modeling of coupled deformation and permeability evolution during fault reactivation induced by deep underground injection of CO2, Int. J. Greenhouse Gas Control, 5, 336–346, doi:10.1016/j.ijggc.2010.08.005.

Cappa, F., and J. Rutqvist. [2011]. Impact of CO2 geological sequestration on the nucleation of earthquakes, Geophys. Res. Lett., 38, L17313, doi:10.1029/2011GL048487

Cappa, F., and J. Rutqvist. [2012]. Seismic rupture and ground accelerations induced by CO_2 injection in the shallow crust, Geophys. J. Intl., 190, 1784-1789.

Carol, I., A. Gens, and E. E. Alonso. [1985]. A three dimensional elastoplastic joint element,

pp. 441–451, Centek Publishers, Lulea, Sweden.

Cheng, A. H.-D. & Detournay, E. [1988]. A direct boundary element method for plane strain poroelasticity. Int. J. Numer. Anal. Methods Geomech. 12, 551±572.

Cheng, A.H-D., Abousleiman, Y., Roegiers, J.-C. [1993]. Review of some poroelastic effects in rock mechanics. Int. J. Rock Mech. Min. Sci. & Geomech. Abstr. Vol.30, No.7, pp.1119-1126

Chester, F. M., J. P. Evans, and R. Biegel. [1993]. Internal structure and weakening mechanisms of the San Andreas Fault, J. Geophys. Res., 98, 771–786.

Childs et al., 2012. VisIt: An End-User Tool For Visualizing and Analyzing Very Large Data; p357-372; Book title: High Performance Visualization-Enabling Extreme-Scale Scientific Insight; https://wci.llnl.gov/simulation/computer-codes/visit/

Chin, L.Y., Raghavan, R., Thomas, L.K. [2000]. Fully coupled geomechanics and fluid flow analysis of wells with stress-dependent permeability. SPE J. 5 [1], 32–45, Paper 58968.

Christian, J. T. & Boehmer, J. W. [1970]. Plane strain consolidation by ®nite elements. J. Soil Mech. Fdn Div. Am. Soc. Civ. Engrs 96, 1435-1457.

Cipolla, C., Warpinski, N.R., Mayerhofer, M.J., Lolon, E.P., Vincent, M.C.:"The Relationship Between Fracture Complexity, Reservoir Treatment and Fracture Treatment Design," Paper SPE 115769, presented at the 2008 SPE Annual Technical Conference and Exhibition, Denver, Colorado, 21-24 September.

Computational Infrastructure for Geodynamics [CIG, 2014]. http://geodynamics.org

Coussy, O. [1995], Mechanics of Porous Continua, John Wiley and Sons, Chichester, England.

Cryer, C. W. [1963]. A comparison of the three dimensional consolidation theories of Biot and Terzaghi. Q. J. Mech. Appl. Math. 16, 401-412.

CUBIT [2013], CUBIT 13.2 User Documentation, Sandia National Laboratories.

Cuenot, N., Dorbath, C., Dorbath, L. [2008]. Analysis of the Microseismicity Induced by Fluid Injections at the EGS Site of Soultz-sous-Foreˆts [Alsace, France]: Implications for the Characterization of the Geothermal Reservoir Properties. Pure appl. geophys. 165 797–828 0033–4553/08/050797–32 DOI 10.1007/s00024-008-0335-7

Cui, L., Abousleiman, Y., Cheng, A. H.-D., Kaliakin, V. & Roegiers, J.-C. [1995]. Finite

element solutions to two problems in anisotropic poroelasticity. Int. J. Numer. Analy. Methods Geomech., [in press].

Dieterich, J. H. [1979]. Modeling of rock friction, 1, Experimental results and constitutive equations, J. Geophys. Res. 84, 2,161–2,168.

Economides, M.J. and Martin, T. Modern Fracturing: Enhamcing Natural Gas Production, Energy Tribune Publishing, 2007.

Edwards, A. L., Trump: A Computer Program for Transient and Steady State Temperature Distributions in Multidimensional Systems, National Technical Information Service National Bureau of Standards, Springfield, Va, 1972.

Ernest L. Majer, Roy Baria, Mitch Stark, Stephen Oates, Julian Bommer, Bill Smith, Hiroshi Asanuma. [2007]. Induced seismicity associated with Enhanced Geothermal Systems. Geothermics. Volume 36, Issue 3, June 2007, Pages 185–222

Faulkner, D.R., Lewis, A.C., Rutter, E.H., 2003.Onthe internal structure and mechanics of large strike-slip faults: Field observations from the Carboneras fault, southeastern Spain. Tectonophysics 367, 235–251.
336, 85–92.

Faulkner, D.R, Mitchell, T.M., Healy, D., Heap, M., 2006. Slip on 'weak' faults by the rotation of regional stress in the fracture damage zone. Nature 444 [7121], 922–925.

Fischer T., Hainzl S., Eisner L., Shapiro S.A. and Le Calvez J. 2008. Microseismic signatures of hydraulic fracture growth in sediment formations: Observations and modeling. Journal of Geophysical Research 113, B02307. doi:10.1029/2007JB005070

Fisher, M. K., J. R. Heinze, C. D. Harris et alet al. 2004. Optimizing horizontal completion techniques in the Barnett Shale using microseismic fracture mapping. Paper SPE 90051 presented at the SPE Annual Technical Conference and Exhibition, Houston, Texas, DOI: 10.2118/90051-MS.

Foxall, W., Savy, J., Johnson, S., Hutchings, L., Trainor-Guitton, W., Chen, M. [2013].Second Generation Toolset for Calculation of Induced Seismicity Risk Profiles. Lawrence Livermore National Laboratory. LLNL-TR-634717

Fredrich, J., Arguello, J., Thorne, B., Wawersik, W., Deitrick, G., de Rouffignac, E., Myer, L., Bruno, M.,[1996]. Three-dimensional geomechanical simulation of reservoir compaction

and implications for well failures in the Belridge Diatomite. Proceedings of the SPE Annual Technical Conference and Exhibition, No. 36698. SPE, Richardson, TX, pp. 195–210.

Galloway, D. L. & Burbey, T. J. Regional land subsidence accompanying groundwater extraction. Hydrogeol. J. 19,1459–1486 [2011].

Gambolati, G., P. Teatini, D. Bau, and M. Ferronato [2000], Importance of poroelastic coupling in dynamically active aquifers of the Po River basin, Italy, Water Resour. Res., 36[9], 2443 – 2459.

Geertsma J [1973] Land subsidence above compacting oil and gas reservoirs. J Petrol Technol 25:734–744

Gens, A., I. Carol, and E. E. Alonso [1988], An interface element formulation for the analysis of soil-reinforcement interaction, Computers and Geotechnics, 7, 133–151.

Ghassemi, A., Tarasovs, S., Cheng, A.H.-D., [2007]. A three-dimensional study of the effects of thermo-mechanical loads on fracture slip in enhanced geothermal reservoir. International Journal for Rock Mechanics & Mining Science 44, 1132–1148.

Ghassemi, A., Zhou, X., [2011]. A three-dimensional thermo-poroelastic model for fracture response to injection/extraction in enhanced geothermal systems. Geothermics 40 39-49

Giardini, D. Geothermal quake risks must be faced. Nature [2009] volume: 462 issue: 7275 page: 848-849

Gibson, R. E., Gobert, A. & Schiffman, R. L. [1990]. On Cryer's problem with large displacements and variable permeability. GeÂotechnique 40, 627±631.

Goodman RE. [1974]. The mechanical properties of joints. In: Proc 3rd Int Congr International Society of Rock Mechanics, 1–7 September 1974, Denver, Colorado. National Academy of Sciences, Washington, DC, vol I, pp 127–140

Gudmundsson, A. [1999]. Fluid overpressure and stress drop in fault zones. Geophys. Res. Lett. 26 [1], 115–118.

Gudmundsson, A. [2004]. Effects of Young's modulus on fault displacement. C.R. Geosci.

Guglielmi, Y., Cappa, F., Amitrano, D. [2008]. High-definition analysis of fluid-induced seismicity related to the mesoscale hydromechanical properties of a fault zone. Geophys. Res. Lett. 35, L06306, doi:10.1029/2007GL033087.

Gutierrez M., Lewis R.W., and Masters I. [2001]. Petroleum reservoir simulation coupling fluid flow and geomechanics. SPE Res. Eval. Eng. 164–172.

Gwo, J.P., P.M. Jardine, G.V. Wilson, and G.T. Yeh. [1996]. Using a multiregion model to study the effects of advective and diffusive mass transfer on local physical nonequilibrium and solute mobility in a structured soil. Water Resour. Res. 32:561–570.

Hawkes, C. D., P. J. McLellan, U. Zimmer, and S. Bachu [2004]. Geomechanical factors affecting geological storage of CO2 in depleted oil and gas reservoirs: risks and mechanisms, in Gulf Rocks 2004: Rock Mechanics Across Borders and Disciplines: Proceedings of the 6th North America Rock Mechanics Symposium, ARMA, Houston, Tex.

Hickman, S., Sibson, R.H., Bruhn, R. [1995]. Introduction to special section: mechanical involvement of fluids in faulting. J. Geophys. Res. 100, 12831–12840.

Hsiung, S.M., Chowdhury, A.H., Nataraja, M.S. [2005]. Numerical simulation of thermal-mechanical processes observed at the Drift-Scale Heater Test at Yucca Mountain, Nevada, USA. Int. J. Rock Mech. Min. Sci. 42, 652–666.

Hubbert, M. King, and Rubey, William W. [1959]. Role of fluid pressure in mechanics of overthrust faulting, I. Mechanics of fluid-filled porous solids and its application to overthrust faulting: Geol. Soc. America Bull., v. 70, p. 115-166

Hughes, T.J.R. and L. P. [1987.] Franca. A new finite element formulation for fluid dynamics: VII. The Stokes problem with various well-posed boundary conditions: Symmetric formulations that converge for all velocity/pressure spaces. Computer Methods in Applied Mechanics and Engineering, 65:85–96.

Jaeger, J. C., and N. G. W. Cook [1979]. Fundamentals of Rock Mechanics, Chapman and Hall, London.

Jha B. [2005]. A mixed finite element framework for modeling coupled fluid flow and reservoir geomechanics. Master's Thesis. Department of Petroleum Engineering, Stanford University, Stanford, CA.

Jha B. and Juanes R. [2007]. A locally conservative finite element framework for the simulation of coupled flow and reservoir geomechanics. Acta Geotechnica 2: 139–153.

Jha, B. and Juanes, R. [2014]. Coupled multiphase flow and poromechanics: a computational model of pore-pressure effects on fault slip and earthquake triggering. Water Resour.

Res., 50, 3776–3808, doi:10.1002/2013WR015175.

Juanes, R., J. Samper, and J. Molinero [2002]. A general and efficient formulation of fractures and boundary conditions in the finite element method, Int. J. Numer. Meth. Eng., 54 [12], 1751–1774.

Khalili, N., F. Geiser, and G. E. Blight. [2004]. Effective stress in unsaturated soils, a review with new evidence, Int. J. Geomech., 4, 115–126.

Kim, J., Schwartz, F.W., Xu, T., Choi, H., Kim, I.S. [2004]. Coupled processes of fluid flow, solute transport, and geochemical reactions in reactive barriers. Vadose Zone Journal, v. 3, p. 867-874.

Kim J. [2009]. Sequential formulation of coupled geomechanics and multiphase flow. Ph.D. Dissertation, Stanford University.

Kim, J., H. A. Tchelepi, and R. Juanes. [2011b]. Stability and convergence of sequential methods for coupled flow and geomechanics: Fixed-stress and fixed-strain splits, Comput. Meth. Appl. Mech. Eng., 200, 1591–1606.

Kohl, T., Evans, K.F., Hopkirk, R.J., Ryback, L., [1995]. Coupled hydraulic, thermal, and mechanical considerations for the simulation of hot dry rock reservoirs. Geothermics 24, 345–359.

Kohl, T., Hopkirk, R.J., [1995]. "FRACimage"—a simulation code for forced fluid flow and transport in fractured, porous rock. Geothermics 24 [3], 333–343.

LaGriT [2013]. Los Alamos Grid Toolbox Manual, Los Alamos National Laboratories.

Lei, X. Y., G. Swoboda, and G. Zenz [1995], Application of contact-friction interface element to tunnel excavation in faulted rock, Comput. Geotech., 17, 349–370.

Lewis, R. W., and Y. Sukirman. [1993]. Finite element modelling of three-phase flow in deforming saturated oil reservoirs, Int. J. Numer. Anal. Methods Geomech., 17, 577–598.

Lewis, R. W., and B. A. Schrefler. [1998]. The Finite Element Method in the Static and Dynamic deformation and Consolidation of Porous Media, second ed., Wiley, Chichester, England.

Lund, J., Freeston, D. [2000]. World-wide direct uses of geothermal energy 2000. Geothermics 30 [2001] 29-68

Maillot, B., Nielsen, S., & Main, I. [1999]. Numerical simulation of seismicity due to fluid injection in a brittle poroelastic medium. Geophys. J. Int. 139, 263-272

Majer, E.L., Peterson, J.E. [2005]. Application of microearthquake monitoring for evaluating and

managing the effects of fluid injection at naturally fractured EGS sites. Geotherm. Resour. Counc. Trans. 29, 103–107.

Majer E.L., R. Baria, M. Stark, S. Oates, J. Bommer, B. Smith and H. Asanuma. [2007]. Induced Seismicity Associated with Enhanced Geothermal Systems, Geotherm., 36, 185-222.

Mainguy M. and Longuemare P. [2002]. Coupling fluid flow and rock mechanics: formulations of the partial coupling between reservoir and geomechanics simulators. *Oil Gas Sci Tech* **57**: 355–367.

Mandel, J. [1953]. Consolidation des sols Geotechnique 3, 287-299.

Marone, C. J. [1998]. Laboratory-derived friction constitutive laws and their application to seismic faulting, Annu. Rev. Earth Planet. Sci. 26, 643–696.

Matsu'ura, M., H. Kataoka, and B. Shibazaki [1992]. Slip-dependent friction law and nucleation processes in earthquake rupture, Tectonophysics 211, 135–148.

Mazzoldi, A., Rinaldi, A., Borgia, A., Rutqvist, J. [2012]. Induced seismicity within geological carbon sequestration projects: Maximum earthquake magnitude and leakage potential from undetected faults. International Journal of Greenhouse Gas Control Volume 10, September 2012, Pages 434–442

McGarr, A., Simpson, D., Seeber, L., [2002]. Case Histories of Induced and Triggered Seismicity. International Handbook of Earthquake and Engineering Seismology, Vol. 81A

McClure, M. [2009] Fracture stimulation in enhanced geothermal systems. Master's thesis report, Stanford University, Stanford, California.

McClure, Mark W., Roland N. Horne. 2013. Discrete Fracture Network Modeling of Hydraulic Stimulation: Coupling Flow and Geomechanics: SpringerBriefs in EarthSciences, Springer.

Miga M.I., Paulsen K.D., and Kennedy F.E. [1998]. Von Neumann stability analysis of Biot's general two dimensional theory of consolidation. Int J Numer Methods Eng 43: 955–974

Miller, S.A., Collettini, C., Chiaraluce, L., Cocco, M., Barchi, M., Kaus, B.J.P., 2004. Aftershocks driven by a high-pressure CO2 source at depth. Nature 427, 724–727.

Minkoff S.E., Stone C.M., Bryant S., Peszynska M., and Wheeler M.F.[2003]. Coupled fluid flow and geomechanical deformation modeling. J Petrol Sci Eng **38**: 37–56.

Mitchell, T.M., Faulkner, D.R., 2009. The nature and origin of off-fault damage surrounding

strike-slip fault zones with a wide range of displacements: a field study from the Atacama fault system, northern Chile. J. Struct. Geol. 31, 802–816, doi:10.1016/j.jsg.2009.05.002.

Morris J. [2009]. Injection and Reservoir Hazard Management: The Role of Injection-Induced Mechanical Deformation and Geochemical Alteration at In Salah CO2 Storage Project. Lawrence Livermore National Laboratory.

Mossop, A., and P. Segall. Subsidence at The Geysers geothermal field, N. California from a comparison of GPS and leveling surveys, Geophysical Research Letters, 24, 1839-1842,1997.

Narasimhan TN, Witherspoon PA. An integrated finite difference method for analysis of fluid flow in porous media. Water Resour Res 1976;12:57–64.

National Risk Assessment Partnership [NRAP]. National Energy Technology Laboratory [NETL]. US Department of Energy. http://www.netl.doe.gov/research/coal/crosscutting/national-risk-assessment-partnership

NEWS, 2014. http://news.discovery.com/earth/weather-extreme-events/oklahoma-has-20-earthquakes-in-one-day-140822.htm

Nicol, A., Carne, R., Gerstenberger, M., Christophersen, A. [2011]. Induced seismicity and its implications for CO2 storage risk. Energy Procedia. Volume 4, 2011, Pages 3699–3706

Nikooee, E., G. Habibagahi, S. M. Hassanizadeh, and A. Ghahramani [2013], Effective stress in unsaturated soils: A thermodynamic approach based on the interfacial energy and hydromechanical coupling, Transp. Porous Med., 96, 369–396.

Nuth, M., and L. Laloui [2008], Effective stress concept in unsaturated soils: Clarification and validation of a unified framework, Int. J. Numer. Anal. Methods Geomech., 32, 771–801.

Okubo, P.G., 1989. Dynamic rupture modeling with laboratory-derived constitutive relations. J. Geophys. Res. 94, 12,321–12,335.

Pan, H., and H. Cao [2010]. User Manual for General Purpose Research Simulator, Stanford University Petroleum Engineering Institute, Stanford, CA. Parotidis, M., Rothert E. and

Shapiro S.A. [2003]. Pore-pressure diffusion: A possible triggering mechanism for the earthquake swarms 2000 in Vogtland/nw-Bohemia, Central Europe. Journal of Geophysical Research 30, 1–12. doi:10.1029/2003GL018110

Pine, R.J. , Batchelor, A.S. [1984]. Downward migration of shearing in jointed rock during

hydraulic injections. International Journal of Rock Mechanics and Mining Sciences & Geomechanics Abstracts. Volume 21, Issue 5, October 1984, Pages 249-263

Pruess, K., Oldenburg, C., Moridis, G., [1999], TOUGH2 user's guide, version 2.0, Lawrence Berkeley National Laboratory Report, LBNL-43134, Berkeley, p.198.

Pruess, K., [2006] Enhanced geothermal systems [EGS] using CO2 as working fluid—A novel approach for generating renewable energy with simultaneous sequestration of carbon. Geothermics 35 [2006] 351–367

Rice, J. R. [1993]. Spatio-temporal complexity of slip on a fault, J. Geophys. Res. 98, 9,885–9,907.

Richards-Dinger, K. B., and Dieterich, J. H. [2012]. RSQSim earthquake simulator, Seismol. Res. Lett. 83, 983–990.

Rinaldi, A.P., Rutqvist, J., Cappa, F., 2014. Geomechanical effects on CO2 leakage through fault zones during large-scale underground injection. Int. J. Greenhouse Gas Control 20 [2014] 117–131 http://dx.doi.org/10.1016/j.ijggc.2013.11.001

Rivas, J.A., Castell´on, J.A., Maravilla, J.N., 2005. Seven years of reservoir seismic monitoring at Berlin Geothermal Field, Usulutan, El Salvador. In: Proceedings of the World Geothermal Congress 2005, Antalya, Turkey, April 24–29, 2005, Paper 0215, 8 pp.

Ruina, A. L. [1983]. Slip instability and state variable friction laws, J. Geophys. Res. 88, 10,359–10,370.

Rutqvist J [1995a] Coupled stress-flow properties of rock joints from hydraulic field testing. PhD Thesis, Royal Institute of Technology, Sweden

Rutqvist, J., Y.-S. Wu, C.-F. Tsang, and G. Bodvarsson. [2002]. A modeling approach for analysis of coupled multiphase fluid flow, heat transfer, and deformation in fractured porous rock, Int. J. Rock Mech. Min. Sci., 39, 429–442, doi:10.1016/S13651609[02]00022-9.

Rutqvist, J., Stephansson, O. [2003]. The role of hydromechanical coupling in fractured rock engineering. Hydrogeol. J. 11, 7–40, doi:10.1007/s10040-002- 0241-5.

Rutqvist, J., C.-F. Tsang,.[2003] Analysis of thermal–hydrologic–mechanical behavior near an emplacement drift at Yucca Mountain. Journal of Contaminant Hydrology 62–63 [2003] 637– 652

Rutqvist, J., D. Barr, R. Datta, A. Gens, A. Millard, S. Olivella, C.-F. Tsang, Y. Tsang. [2005]. Coupled thermal-hydrological-mechanical analysis of the Yucca Mountain Drift Scale Test-comparison of field results to predictions of four different models. International Journal of Rock Mechanics and Mining Sciences, 42 [2005], pp. 680–697

Rutqvist, J., J. T. Birkholzer, and C. F. Tsang. [2008]. Coupled reservoir–geomechanical analysis of the potential for tensile and shear failure associated with CO2 injection in multilayered reservoir–caprock systems, Int. J. Rock Mech. Min. Sci., 45, 132–143.

Rutqvist, J., Tsang, C.-F. [2012]. Multiphysics processes in partially saturated fractured rock: experiments and models from yucca mountain. Rev. Geophys. 50[3], http://dx.doi.org/10.1029/2012RG000391.

Schellschmidt, R., Clauser, C., Sanner, B., [2000]. Geothermal energy use in Germany at the turn of the millennium, World Geothermal Congress 2000, Japan

Schiffman, R. L., Chen, A. T.-F. & Jordan, J. C. [1969]. An analysis of consolidation theories. J. Soil Mech.Fdn Div. Am. Soc. Civ. Engrs 95, 295±312.

Settari, A., and F. Mourits [1998]. A coupled reservoir and geomechanical simulation system, Soc. Pet. Eng. J., 3, 219–226.

Settari, A. and Mourits, F.M.[1994]: "Coupling of geomechanics and reservoir simulation models," Computational Methods and Advances in Geomechanics, Siriwardane and Zeman [eds.], Balkema, Rotterdam, The Netherlands [1994] 2151.

Shapiro S.A., Rentsch S. and Rothert E. [2005b]. Fluid-induced seismicity: Theory, modeling and applications. Journal of Engineering Mechanics 131, 947–952

Shapiro, S. A., and C. Dinske. [2009]. Scaling of seismicity induced by nonlinear fluid- rock interaction, J. Geophys. Res., 114, B09307, doi:10.1029/2008JB006145

Sibson, R. H. [1977]. Fault rocks and fault mechanisms, J. Geol. Soc. Lond., 133, 191–213.

Sibson, R. H. [1990]. Rupture nucleation on unfavorably oriented faults, Bull. Seismol. Soc. Am., 80, 1580–1604.

Sibson, R.H., Rowland, J.V. [2003]. Stress, fluid pressure and structural permeability in seismogenic crust, North Island, New Zealand. Geophys. J. Int. 154, 584–594

T. Li, M.F. Cai, M. Cai. [2007]. A review of mining-induced seismicity in China. International Journal of Rock Mechanics & Mining Sciences 44 [2007] 1149–1171

Talwani, P., 1997. On the Nature of Reservoir-induced Seismicity. Pure appl. geophys. 150

[1997] 473–492

Tarasovs, S. and Ghassemi, A. [2012]. On the Role of Thermal Stress in Reservoir Stimulation. Oral presentation given at the Thirty-Seventh Workshop on Geothermal Reservoir Engineering, Stanford University, Stanford, California, 30 January–February 1

Teklemariam, M., Beyene, K., Amdeberhan, Y., Gebregziabher, Z. [2000]. Geothermal development in Ethiopia. World Geothermal Congress 2000, Japan.

Terzaghi, K., R. B. Peck, and G. Mesri. [1996]. Soil Mechanics in Engineering Practice, John Wiley & Sons, New York, NY.

Thomas L.K., Chin L.Y., Pierson R.G., and Sylte J.E. [2003]. Coupled geomechanics and reservoir simulation. SPE J 8[4]: 350–358.

Tran D., Settari A., and Nghiem L. [2004[. New iterative coupling between a reservoir simulator and a geomechanics module. SPE J 9[3]:362–369.

Tullis, T. E. [1988]. Rock friction constitutive behavior from laboratory experiments and its implications for an earthquake prediction field monitoring program, Pure Appl. Geophys. 126, 555–588.

Uehara, S.I., Shimamoto, T. [2004]. Gas permeability evolution of cataclasite and fault gouge in triaxial compression and implications for changes in fault-zone permeability structure through the earthquake cycle. Tectonophysics 378, 183–195.

Vermilye, J.M., Scholz, C.H. [1998]. The process zone: a microstructural view of fault growth. J. Geophys. Res. 103 [B6], 12 223–12 237.

Verruijt, A. 2013. Theory and problems of poroelasticity. Delft University of Technology

Vlahinic, I., H. M. Jennings, J. E. Andrade, and J. J. Thomas [2011], A novel and general form of effective stress in a partially saturated porous material: The influence of microstructure, Mech. Mater., 43, 25–35.

Voyiadjis, GZ., Song, CR. [2006]. The coupled theory of mixtures in geomechanics with applications.

Wainwright, H., Stefan Finsterle, S., Zhou, Q., Birkholzer, J. [2012]. Modeling the Performance of Large Scale CO2 Storage Systems: A Comparison of Different Sensitivity Analysis Methods. U.S. Department of Energy.

Walsh J.B. [1981]. Effects of pore pressure and confining pressure on fracture permeability. Int J Rock Mech Mining Sci Geomech Abstr 18:429–435

Wang, H. Theory of Linear Poroelasticity with Applications to Geomechanics and Hydrogeology [Princeton Univ. Press, Princeton, New Jersey, 2000]

Wibberley, C.A.J., Shimamoto, T. [2005]. Earthquake slip weakening and asperities explained by thermal pressurization. Nature 436, 689–692, doi:10.1038/nature03901.

Wilson, J.E., Chester, J.S., Chester, F.M. [2003]. Microfracture analysis of fault growth and wear processes, Punchbowl Fault, San Andreas System, California. J. Struct. Geol. 25 [11], 1855–1873.

Witherspoon, P.A., Wang, J.S.Y., Iwai, K., Gale, J.E. [1980]. Validity of cubic law for fluid flow in a deformable rock fracture. Water Resour. Res. 16, 1016–1024.

Xu, T., Sonnenthal, E., Spycher, N., Pruess, K. [2004]. TOURGHREACT: A Simulation Program for Non-isothermal Multiphase Reactive Geochemical Transport in Variably Saturated Geologic Media. Earth Sciences Division, Lawrence Berkeley National Laboratory, University of California, Berkeley, CA 94720, USA

Zhang, Z., Wang J., Ren, X., Liu, S., Zhu, H., 2000b. The state-of-the-art and future development of geothermal energy in China. Country update report for the period 1996-2000. World Geothermal Congress 2000, Japan.

Zienkiewicz OC, Paul DK, Chan AHC [1988] Unconditionally stable staggered solution procedure for soil–pore fluid interaction problems. Int J Numer Methods Eng 26[5]:1039–1055

Zienkiewicz OC, Taylor RL. [2005]. The finite element method for solid and structural mechanics. 6th ed. Butterworth-Heinemann.

Zoback, M., Byerlee, J. Permeability and Effective Stress: GEOLOGIC NOTES. Volume: 59 [1975]

Zoback M.D., H. -P Harjes [1997]. J. Geophys. Res. 102, 18477-18491.

Zoback M.D. and Harjes H.-P. 1997. Injection-induced earthquakes and crustal stress at 9 km depth at the KTB deep drilling site, Germany. Journal of Geophysical Research 102, 18 477–18 491

Zoback M.D. [2007]. Reservoir Geomechanics. Cambridge, UK: Cambridge University Press.

Zoback, M.D., Gorelick, S.M. [2012]. Earthquake triggering and large-scale geologic storage of carbon dioxide. Proc. Natl. Acad. Sci.,http://dx.doi.org/10.1073/pnas.1202473109.

Zuluaga E., Schmidt J.H., and Dean R.H. [2007]. The use of a fully coupled geomechanics-

reservoir simulator to evaluate the feasibility of a cavity completion. SPE Ann Tech Conf Exhib [SPE109588], Anaheim CA, 11-14 Nov.

APPENDIX

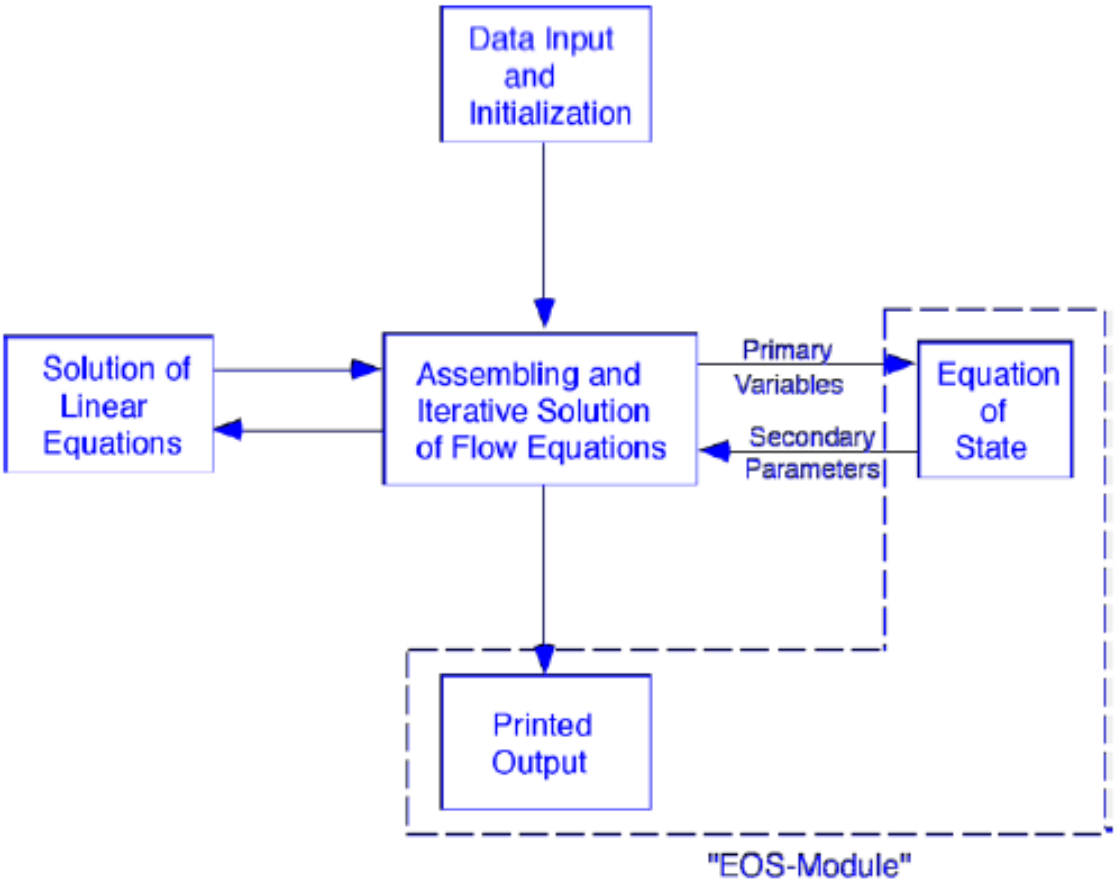

Figure A1. Modular architecture of TOUGH2

Table A1. TOUGH2 input data blocks

Keyword	Function
TITLE (first record)	one data record (single line) with a title for the simulation problem
MESHM	optional; parameters for internal grid generation through MESHMaker
ROCKS	hydrogeologic parameters for various reservoir domains
MULTI	optional; specifies number of fluid components and balance equations per grid block; applicable only for certain fluid property (EOS) modules
SELEC	used with certain EOS-modules to supply thermophysical property data
START	optional; one data record for more flexible initialization
PARAM	computational parameters; time stepping and convergence parameters; program options
DIFFU	diffusivities of mass components
FOFT	optional; specifies grid blocks for which time series data are desired
COFT	optional; specifies connections for which time series data are desired
GOFT	optional; specifies sinks/sources for which time series data are desired
RPCAP	optional; parameters for relative permeability and capillary pressure functions
TIMES	optional; specification of times for generating printout
*ELEME	list of grid blocks (volume elements)
*CONNE	list of flow connections between grid blocks
*GENER	optional; list of mass or heat sinks and sources
INDOM	optional; list of initial conditions for specific reservoir domains
*INCON	optional; list of initial conditions for specific grid blocks
NOVER (optional)	optional; if present, suppresses printout of version numbers and dates of the program units executed in a TOUGH2 run
ENDCY (last record)	one record to close the TOUGH2 input file and initiate the simulation
ENDFI	alternative to "ENDCY" for closing a TOUGH2 input file; will cause flow simulation to be skipped; useful if only mesh generation is desired

§ Blocks labeled with a star * can be provided as separate disk files, in which case they would be omitted from the INPUT file.

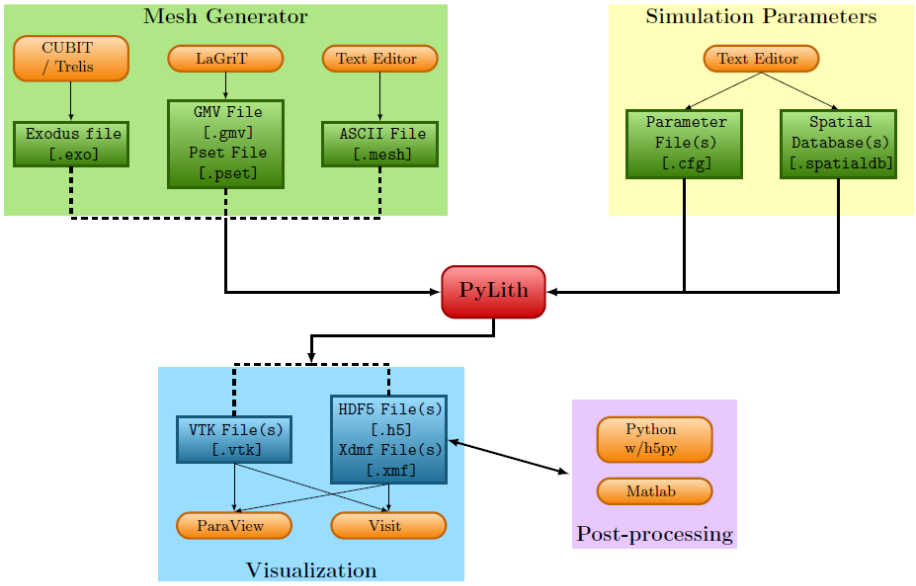

Figure A2. PyLith module and file formats

VITA

Mamun Miah was born and raised in Bangladesh. He completed his bachelor's degree in civil engineering from Bangladesh University of Engineering and Technology in 2009. He came to USA in the same year for higher study. He then obtained a master's degree in engineering science with an emphasis in civil engineering from the University of Mississippi in 2010. He pursued a doctoral study at the same department and same institution starting in 2011. A summer 2013 internship experience at the Lawrence Berkeley National Laboratory enabled him to obtain funding for furthering his Ph.D. research and eventually completing the degree in August 2016. He is joining the Berkeley Lab as a post-doctoral researcher from July 2016.